A Novel Framework Using Brain Computer Interfacing & EEG Microstates To Characterize Cognitive Functionality

A NOVEL FRAMEWORK USING BRAIN COMPUTER INTERFACING & EEG MICROSTATES TO CHARACTERIZE COGNITIVE FUNCTIONALITY

BY

SAURABH BHASKAR SHAW,

A THESIS

SUBMITTED TO THE MCMASTER SCHOOL OF BIOMEDICAL ENGINEERING

AND THE SCHOOL OF GRADUATE STUDIES

OF MCMASTER UNIVERSITY

IN PARTIAL FULFILMENT OF THE REQUIREMENTS

FOR THE DEGREE OF

MASTER OF APPLIED SCIENCE

Master of Applied Science (2016) McMaster University

(Biomedical Engineering) Hamilton, Ontario, Canada

TITLE:	A Novel Framework Using Brain Computer Interfacing & EEG Microstates To Characterize Cognitive Functionality
AUTHOR:	Saurabh Bhaskar Shaw B.Eng., (Electrical and Biomedical Engineering) McMaster University, Hamilton, Canada
SUPERVISOR:	Dr. Michael D. Noseworthy and Dr. John F. Connolly
NUMBER OF PAGES:	xviii, 133

What is wanted is not the will to believe, but the will to find out, which is the exact opposite. — Bertrand Russell

Abstract

The rapid advancements in the field of machine learning and artificial intelligence has led to the emergence of technologies like the Brain Computer Interface (BCI), which has revolutionized rehabilitation protocols. However, given the neural basis of BCIs and the dependence of its performance on cognitive factors, BCIs may be used to characterize the functional capacity of the user. A resting state segment can also be considered for characterization of the functional network integrity, creating a two part framework that probes the functional networks and their cognitive manifestations. This thesis explores such a two part framework using a simultaneous EEG-fMRI setup on a healthy population. The BCI accuracies for all subjects increased over the course of the scan and is thought to be due to learning processes on the subject's part. Since such learning processes require cognitive faculties such as attention and working memory, these factors might modulate the BCI performance profile, making it a potential metric for the integrity of such cognitive factors. The resting state analysis identified four EEG Microstates that have been previously found to be associated with verbal, visual, saliency and attention reorientation tasks. The proportion of each microstate that composed the corresponding fMRI resting state networks (RSN) were identified, opening up the potential for predicting fMRI-based RSN information, from EEG microstates alone. The developed protocol can be used to diagnose potential

conditions that negatively affect the functional capacity of the user by using the results from this study as healthy control data. This is the first known BCI based system for characterization of the user's functional integrity, opening up the possibility of using BCIs as a metric for diagnosing a neuropathology.

Acknowledgements

Firstly, I would like to acknowledge the immense contributions made by my co-supervisors Dr.Michael D Noseworthy and Dr.John F Connolly. They have guided me throughout the research process and have helped me with obstacles along this path.

I would also like to acknowledge the members of both labs - The Imaging Research Centre (Alejandro Santos, David Stillo, Olga Donalemus, Conrad Rockel, Evan McNabb, Amy Harrison, Mitch Doughty, Michael Behr, Maria Charles Herrera, Alireza Akbari and Nick Simard) and the Linguistics Lab (Richard Mah, Kyle Ruiter, Rober Boshra, and Angela Harrison), for the numerous intellectual discussions that has often given me new directions in my research, and for graciously volunteering for scans.

I would like to acknowledge Kiret Dhindsa and Dr. Sue Becker for the numerous discussions on BCIs and the collaborations which has been a huge contributing factor for my current knowledge base.

I would like to acknowledge the MRI technologists Carol, Cheryl and Julie, for patiently putting up with the numerous tests that I ran, and with the scanning of all the subjects.

I would like to acknowledge the undergraduate volunteers - Rami Saab and Hannah Milan that helped me with certain segments of my research.

I would like to acknowledge my closest friends Maria, Daniel, Kyle, Jaki, Neel and Dwip for sticking by me during the ups and downs of the research process (which they never heard the end of).

And finally, I would like to acknowledge my mother Suchitra Shaw, father Sanjay Shaw and sister Srinidhi Shaw, who have been by my side for the past 23 years, believing in me and helping me achieve each milestone in my life thus far. They have always put a lot of faith in me and have sacrificed a lot for me to reach this milestone.

Notation and Abbreviations

The following mathematical notations are followed throughout the thesis:

- The transpose of a matrix A is represented as A^T
- The inverse of a function or transform $\mathcal{F}$ is represented as $\mathcal{F}^{-1}$
- The convolution is denoted by the $\star$ operator. Hence the convolution of two functions f and g is written as $f \star g$
- The raw input data is represented by the variable x, and its transformed variants X and $\boldsymbol{X}$.
- The trace of a matrix A is the sum along its diagonal elements and is represented by $Tr(A)$

The following abbreviations are commonly used throughout the thesis:

- ADHD - Attention Deficit Hyperactivity Disorder
- AF - Adaptive Filtering
- ALS - Amyotrophic Lateral Sclerosis
- BCG - Ballistocardiogram
- BCI - Brain Computer Interfacing
- BOLD signal - Blood Oxygen Level Dependent signal
- BSS - Blind Source Separation

- CCD - Charged Coupled Device
- CEN - Central Executive Network
- CMOS - Complementary Metal-Oxide Semiconductor
- CNR - Contrast to Noise Ratio
- CNV - Contingent Negative Variation
- CSF - Cerebrospinal Fluid
- CSP - Common Spatial Patterns
- CT - Computed Tomography
- DMN - Default Mode Network
- dynFC - Dynamic Functional Connectivity
- ECG - Electrocardiography
- ECoG - Electrocorticography
- EEG - Electroencephalography
- EMG - Electromyography
- EOG - Electro-oculography
- ERD - Event Related Desynchronization
- ERP - Event Related Potentials
- ERS - Event Related Synchronization
- fMRI - Functional Magnetic Resonance Imaging
- fNIRS - Functional Near-Infrared Spectroscopy
- FC - Functional Connectivity
- FOV - Field Of View
- FT - Fourier Transform
- GA - Gradient Artifact
- GCS - Glasgow Coma Scale
- GFP - Global Field Potential
- GLM - Generalized Linear Model
- HR - Hemodynamic Response
- HRF - Hemodynamic Response Function
- k-NN - K Nearest Neighbors
- LDA - Linear Discriminant Analysis
- LFP - Local Field Potential
- IBM - International Business Machines corporation (the company)
- ICA - Independent Component Analysis
- MEG - Magnetoencephalography
- ML - Machine Learning
- MRI - Magnetic Resonance Imaging

- mTBI - Mild Traumatic Brain Injury
- MUA - Multi-Unit Activity
- NN - Neural Network
- OA - Ocular Artifacts
- OBS - Optimal Basis Set
- PCA - Principle Component Analysis
- PCSS - Post-Concussion Symptom Scale
- PPV - Positive Predictive Value
- PSD - Power Spectral Density
- PTSD - Post Traumatic Stress Disorder
- RBF - Radial Basis Function
- RF - Radio Frequency
- RLS - Recursive Least Squares
- ROI - Region Of Interest
- rsEEG - Resting State EEG
- rsfMRI - Resting State fMRI
- RSN - Resting State Network
- SCP - Slow Cortical Potential
- ScWT - Scattering Wavelet Transform
- SUA - Single Unit Activity
- SMR - Sensori-Motor Rhythm
- SN - Salience Network
- SNR - Signal to Noise Ratio
- SSVEP - Steady-State Visual Evoked Potential
- STFT - Short Time Fourier Transform
- SVD - Singular Value Decomposition
- SVM - Support Vector Machine
- SQUID - Superconducting QUantum Interference Device
- TR - Repetition Time
- TRN - Task Related Network
- TVEP - Transient Visual Evoked Potentials
- VEP - Visual Evoked Potentials
- VSDI - Voltage Sensitive Dye Imaging
- WT - Wavelet Transform

Contents

List of Figures

Chapter 1

Introduction

The idea of a Learning Computer has intrigued scientists ever since the advent of computers. Friedberg (1958) discussed the utility of such a device that would learn aspects of a task and consequently get better at performing them. Friedberg proposed to do this by trial and error, accumulating the trials that resulted in a positive result. The IBM 704 was used for his simulations due to the large amounts of computational power and storage required to accomplish this task. However, the size and cost associated with such computers (approximately 1 million USD at the time) limited the widespread use of such learning algorithms (Rothenberg, 1982).

The advancement in affordable computing power over recent decades has greatly accelerated the development of more advanced learning algorithms, such as support vector machines, neural networks and deep belief networks. Such algorithms are more commonly known as machine learning (ML) and have been extensively used in fields such as artificial intelligence and data mining. ML techniques are particularly useful in identifying features in data that may otherwise be hard for humans to distinguish. This utility has led to ML being used for numerous data discovery purposes such

as detecting fraud from large scale financial data, studying astronomical data, and identification of optimal investment schemes (Fayyad *et al.*, 1996).

Due to its prowess in identifying unique features, ML is also useful in classifying data by recognizing distinguishing features. Among other fields, examples of its use can be found in computer vision where objects in the field of view are identified and classified into various categories (Medathati *et al.*, 2016).

Among numerous other fields, the boom in machine learning has led to its application in the identification of brain patterns and states. This forms the basis of Brain Computer Interfacing (BCI). These are systems that use machine learning methods to process neurologically derived data for identification and classification of a current brain state. The identified brain state is then used by a computer to perform a particular task.

BCI research was slow to start earlier in the century due to the high computational demand of BCI systems. The advent of faster and more powerful computers coupled with their diminishing costs led to a boom in the number of BCI related publications in the late 1990s and early 2000s. The cumulative number of BCI related publications rose exponentially from 69 in 2000 to 1081 in 2008 (Hamadicharef, 2010). The improvement in neural signal acquisition techniques such as EEG, fMRI and fNIRS may have also contributed to the research boom in this burgeoning field.

Apart from using such acquisition methods for BCIs and studying the brain under cognitive load, they have been used to study of the resting state properties of the brain i.e. the brain under zero cognitive load. Starting in 1995 (Biswal *et al.*, 1995), resting state analysis found applicability in the study of learning, sleep, sedation and neurophysiological ailments (Hutchison *et al.*, 2013). It has also been used to

successfully characterize the networks involved in the upkeep of the brain and its functionality under zero cognitive load.

This thesis is organized into 9 Chapters - Chapters 2, 3 and 4 present a detailed review of the current literature on Brain Computer Interfaces, Resting State analysis of the human brain and simultaneous EEG-fMRI acquisition respectively. Chapter 5 discusses the objectives and the hypotheses of the current project, followed by the methods used detailed in Chapter 6. Chapters 7 and 8 explore the results and its significance in light of the current literature. Chapter 9 concludes the thesis by discussing the future possibility of applying the created framework for diagnostic purposes.

Chapter 2

Brain Computer Interfaces

The Brain Computer Interface (BCI) is a system which takes neurologically derived signals, indicative of certain brain functions and uses them as a control signal to control computers, or other physical devices. BCIs stemmed from the quest for computer based techniques to identify a person's intention for actuating a lingual command or a physical motion. BCIs detect such intentions and carry out the indicated task independently, bypassing the efferent neuronal pathways that would traditionally be used for completing the action. As such, these are excellent tools for paralyzed patients or patients with a physical disability that affect these efferent pathways.

First suggested by Vidal (1973), such a system was first implemented by Wolpaw *et al.* (1991) by using the sensorimotor rhythm in the brain to control a cursor on a computer screen. Since then, numerous other applications have been designed and built such as spellers for locked-in patients, controllers for lights or fans and restoring movement for patients with spinal injuries (Nicolas-Alonso and Gomez-Gil, 2012).

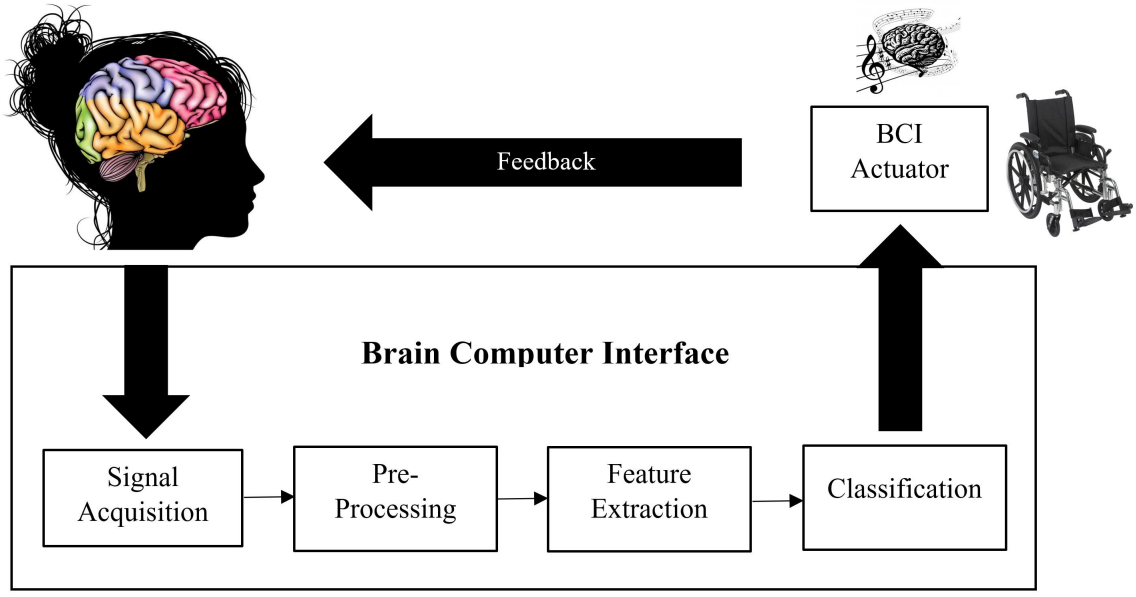

Figure 2.1: A BCI generally consists of 5 major components as shown. The signal recorder acquires the neural signal from the brain, after which the signal is pre-processed for feature extraction. The extracted features are used by a classifier to identify the current brain state, which triggers a control signal which actuates a machine such as a wheelchair motor or a note played by a computer.

2.1 General Structure of a BCI

The general structure of a BCI is shown in Figure 2.1. The neural signal is recorded using a non-invasive modality over a short segment of time and is pre-processed to minimize noise. The pre-processed data is then analyzed by the computer to compute features which are used by a classifier to identify the brain state or the intention of the user. That particular intention is carried out by the computer, thereby providing neurofeedback to the user in the form of the task carried out. Following a few trials, the user learns the thinking pattern required to indicate the correct intention to the computer, leading to an improvement in BCI accuracy over time.

A BCI system comprises of 5 major components - signal recorder, the pre-processor, the feature extractor, the signal classifier and the actuator

2.1.1 Signal recorder

The signal recorder acquires the neural signal to be used by the BCI for deciphering the user's intention. Acquiring such a signal can be a challenge as the brain is situated inside a bony cage, covered with skin and hair. These obstacles attenuate and distort the neural signal, making it more noisy (Buzsáki *et al.*, 2012). Consequently, numerous approaches have been developed over the years to acquire these signals with the least amount of noise and distortion. However, this comes at the cost of poorer temporal or spatial resolution, or increasing the invasiveness of the recording procedure. Some of these modalities include EEG, fMRI, fNIRS, MEG and VSDI which are reviewed in this section.

An ideal signal recorder must be reliable and robust in order to prevent contamination of the neural signal with machine drift which may deteriorate BCI performance over time. The recorder must also be non-invasive and easy to apply/remove to minimize user discomfort during the multiple sessions often required to train BCIs. Furthermore, the recorder must be able to update the brain derived signal with sufficient temporal resolution to capture dynamic neural features which could be potentially useful for the BCI task at hand.

Electroencephalography (EEG)

The possibility of detecting the electrical activity of neurons on the external surface of the scalp, over an intact skull was first shown by Hans Berger (1929), (See Gloor

(1969) for an english translation). This demonstrated the possibility of recording neural activity by using an electrode on the surface of the scalp to create an electroencephalograph. Consequently, this modality was termed Electroencephalography or EEG.

The neural origin of the voltages are graded postsynaptic potentials of the cell body (soma) and the apical dendrites of vertically orientated pyramidal cells in layers three, four and five of the cerebral cortex (Mayer and Bellgowan, 2014). Synchronized polarization and depolarization of these apical dentrites generate the voltages on the surface of the scalp. In addition to the cortical activity, vertical currents (flowing perpendicular to the scalp) in the extracellular space also influence the EEG voltage (Vidal, 1973). Since these currents could be from activity in deeper neurons or from adjacent neurons, the voltage at an electrode is influenced by a "ball" of neural tissue directly underneath it and surrounding it. The impedence of the overlying CSF, skull and tissues further attenuate and spatially blur the neural signal (Rice *et al.*, 2013). The EEG signal is therefore a spatially and temporally blurred version of the local field potential (LFP). This region of influence is usually limited to an area of 10 cm^2 due to limited conductance of the neural tissue, and the distance-dependent attenuation of the electrical fields generated by the cortical apical dentrites (Buzsáki *et al.*, 2012). Hence, in order to obtain a comprehensive dataset which describes activity over the entire brain, a spatially distributed array of electrodes is used.

Despite not directly measuring action potentials, EEG is still representative of neural activity (Whittingstall and Logothetis, 2009) due to the tight coupling of synaptic activity and action potentials (Larkum *et al.*, 2001) .

EEG signal contains a wide variety of frequency domain features, each of which are

modulated by different types and/or regions of neural activity. To better characterize these features, the EEG signal is divided into various frequency bands (Table 2.1).

EEG signal has excellent temporal resolution due to the instantaneous changes in electrical fields affecting the EEG voltages combined with a high sampling rate. EEG can therefore capture neurological processes that occur at fine temporal scale. However, due to the limited region of neural tissue capable of influencing EEG voltages, the EEG signal is primarily limited to the cerebral cortex. The volume conduction effects also spatially blur the voltage recorded at each electrode, leading to a decline in spatial resolution.

Functional Magnetic Resonance Imaging (fMRI)

Primarily used for anatomical imaging, MRIs can also be used to study the functional aspects of neural activity, using fMRI. The underlying assumption in fMRI is that an increase in neural activity leads to an increase in the local blood flow causing a rise in oxygenated blood flow to that particular region (shown in Figure 2.2). This results in a drop in the local deoxyhaemoglobin content. Since, T_2^* intensity is inversely proportional to the relative deoxyhaemoglobin content (due to its paramagnetic properties), this decrease in deoxyhaemoglobin content increases the local T_2^* relaxation time. Hence activated regions show up as a region of increased intensity on T_2^* weighted images. The intensity of each voxel represents the activity of the neurons in that voxel at a given time. This is referred to as the Blood Oxygen Level Dependent (BOLD) signal. Full brain T_2^* weighted images acquired at multiple time points can be used to create a timeseries of the BOLD signal at each voxel.

Band Name	**Frequency (Hz)**	**Region of Origin**	**Description**
Delta (δ)	0 - 4	Antero-frontal regions	Spontaneously generated during sleep and under neuropathologies. Predominant EEG band during human infancy (upto 2 years).
Theta (θ)	4 - 8	Anterior Cingulate	Associated with hypnagogic imagery, REM sleep, meditative state, conscious awareness, problem solving and attention. Has two subtypes which correspond to low alertness activities and attention related activites respectively.
Alpha (α)	8 - 13	Occipital region	Associated with visual processing and memory related functions. Present during the lack of cognitive activity and during awake relaxation.
Mu (μ)	8 - 12	Central region	Associated with motor activity and correlates with Beta activity.
Beta (β)	13 - 32	Frontal and Central regions	Linked to motor activity and imagery. Symmetric distribution under rest and becomes unsymmetric under motor load.
Gamma (γ)	32 - 60	Fronto-temporal regions	Related to cognitive processes involving integration of different stimuli to understand a complete scenario. Also involved in force modulation of strong motor contractions.

Table 2.1: The frequency bands of EEG signal and their corresponding significance (Mayer and Bellgowan, 2014), (Nicolas-Alonso and Gomez-Gil, 2012), (Lehmann *et al.*, 2001), (Michel *et al.*, 1992)

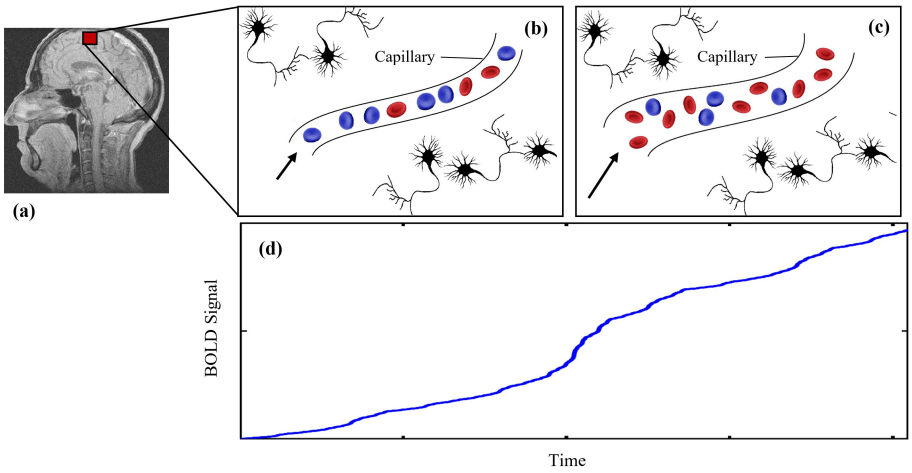

Figure 2.2: Physiological basis of BOLD signal (a) The capillaries in the red voxel of the brain is shown in (b) and (c). (b) is the state of the capillary under rest. When activated, the capillary expands, increasing the amount of oxyhaemoglobin relative to deoxyhamoglobin (c). This can be seen as a rise in the average BOLD signal (T2* intensity), as shown in panel (d). Figure adapted from (Huettel *et al.*, 2004)

The intensity of the BOLD signal is given by equation 2.1 (Uludag *et al.*, 2005), where A is a local scaling factor, V is the venous blood volume, E is the oxygen ejection fraction, and β is a field dependent parameter that is constant across the brain.

$$BOLD = \frac{\Delta S}{S_{rest}} = A \cdot \left[1 - \frac{V_{active}}{V_{rest}} \cdot \left(\frac{E_{active}}{E_{rest}}\right)^{\beta}\right] \tag{2.1}$$

Localized neural activation leads to a drop in the local oxygenation fraction, however the tight coupling of neural activity with blood flow, overcompensates for this drop by increasing the local oxygenated blood volume (V_{active}), decreasing the oxygen ejection fraction (E_{active}). This leads to an overall increase in the $BOLD$ signal. The coupling of neural activation with increased blood flow is characterized by the haemoynamic response (mathematically described as the haemodynamic response function -

HRF). The peak in blood flow is found to lag behind the onset of neural activation by about 3-6 seconds (Weiskopf *et al.*, 2004). Since the BOLD signal is sensitive to the blood flow dependent increase in oxygen, it is limited by the time delay introduced by the HR. This temporal blurring coupled with the long time taken by the MRI to acquire a single time point, results in BOLD signal having poor temporal resolution. However, the ability of MRI to acquire data concurrently from numerous voxels distributed across the entire brain, including deep brain structures, results in excellent spatial resolution of the BOLD signal.

One of the drawbacks of fMRI is the immobile and expensive MRI system required to acquire data. This limits the utility of fMRI to stationary BCIs and for identification of promising BCI features to be used with other signal recording modalities.

Functional Near-Infrared Spectroscopy (fNIRS)

fNIRS is another modality dependent on the haemodynamic response of neural activation. It exploits the difference in absorbence values of infrared light between oxyhaemoglobin and deoxyhaemoglobin to detect the increase in oxygenated blood flow in the region of neural activation. In addition to temporal blurring of the neural activation due to the haemodynamic response function (HRF), fNIRS signal is spatially limited due to the limited depth of penetration and scattering of photons.

Despite these shortcomings, fNIRS has been used to create BCIs using motor imagery as the control signal (Coyle *et al.*, 2007). It is gradually gaining popularity due to its low cost, high portability and ease of application.

Magnetoencephalography (MEG)

MEG is very similar to EEG as it directly records the neural activity rather than use an indirect measure of neural activation (such as in BOLD). However, unlike EEG which detects the electrical fields associated with neuronal activation, MEG senses the coupled magnetic field accompanying electrical fields. This was first demonstrated by David Cohen in 1972 by recording healthy alpha activity and abnormal epileptic activation from a subject using a superconducting quantum interference device (SQUID) (Cohen, 1972). Since then MEG has been used for numerous studies probing the functional activity of the human brain, owing to the superior spatial (2-3 mm) and temporal resolution (1 ms) of MEG as compared to that of EEG. This is due to the immunity of magnetic fields to the distortions caused by the skull and other intermediate tissue. The poorer spatial resolution in EEG is partly due to such distortions which affect the electrical fields (Buzsáki *et al.*, 2012).

The first application of MEG to an online BCI was in 2005 where MEG was successfully used to classify motor imagery of moving the little finger vs. moving the tongue (Lal *et al.*, 2005). Despite some other attempts, MEG is sparingly used for BCIs due to the bulkiness and cost associated with the recording equipment.

Invasive Signal Acquisition Modalities

To exclude the disruptive effects of the skull and the overlying tissue, electrodes can be surgically implanted on the brain surface. This can be done in two ways - by placing arrays of electrodes on the surface of the brain, just underneath the scalp to obtain an Electrocorticograph (ECoG), or by placing the electrodes in the cortical gray matter to obtain an intracortical neuron recording. Both of these modalities

require a craniotomy to install the electrode array and are therefore very invasive. Data from these electrodes can be obtained via wireless link to prevent physical wires entering the cranium, reducing the chances of infections (Anderson and Harrison, 2010).

Electrocorticograph (ECoG) The ECoG signal is acquired by placing an array of sub-dural electrodes on the surface of the brain. It has a much higher spatial (<5 mm^2) and temporal resolution than EEG/MEG and is much more immune to external artifacts such as blink and muscle artifacts (Buzsáki *et al.*, 2012). These electrodes are usually made of platinum-iridium or stainless steel The region of neural tissue from which data can be practically acquired is limited due to the limited space available for implanting electrodes.

Intracortical Neuron Recording/Microdepth EEG are recordings obtained by an electrode or an array of electrodes inside the brain, in the intercellular space. A fine array of such electrodes (made of glass or silicon) can record high resolution local field potentials (LFP) from a small volume of neural tissue. The LFP recorded at an electrode is the sum of all transmembrane currents, synaptic currents, ionic processes and action potentials from nearby neurons (Buzsáki *et al.*, 2012). This allows for a very comprehensive dataset which contains activity information from a very specific neuronal population. For much higher resolution, the electrodes can be inside individual neurons, recording single-unit activity (SUA) or multi-unit activity (MUA). These signals record neuronal spiking rather than continuously changing voltages (Nicolas-Alonso and Gomez-Gil, 2012).

Preliminary BCI research in animals (monkeys and rats) showed the potential of

such recordings in predicting the type and direction of intended movement for learned motions (such as tracing a sinusoid in (Schwartz, 1993)). The activity of populations of neurons can be used together to decipher more comprehensive movement profiles such as moving a prosthetic limb and grasping an object (Velliste *et al.*, 2008) (Vargas-Irwin *et al.*, 2010). Advancements in electrode synthesis and implantation techniques has allowed for such control in humans as well. An example of this is David Bundy's study where ECoG data was used to predict kinematic aspects of limb movements in 3D (Bundy *et al.*, 2016).

However, the invasive nature of the recording equipment leads to issues for long term use. The quality of acquired signal deteriorates over time due to gliosis at the electrode tip, leading to fibrotic encapsulation. The platinum and silicon electrodes undergo corrosion and structural damage as well (Barrese *et al.*, 2016). The level of encapsulation varies from one subject to another, and in some cases does not greatly affect BCI performance (Degenhart *et al.*, 2015).

Such modalities can be particularly useful for BCIs geared towards rehabilitation and control of robotic prosthetic limbs once bio-compatibility issues surrounding the implanted electrodes are resolved.

Voltage-sensitive dye imaging (VSDI)

VSDI relies on optical intensity changes of membrane-bound voltage sensitive-dyes or genetically modified voltage-sensitive proteins in response to changing transmembrane voltage. The optical signal is recorded using CCD or CMOS probes. The changes in optical intensity vary linearly with the transmembrane voltage, thereby providing an indirect measure of the transmembrane voltage (Tsytsarev *et al.*, 2014). This is

in contrast to all other modalities which measure the intercellular voltage. Despite this advantage, VSDI suffers from low signal-to-noise ratio, and potential interference with neuronal metabolism (Buzsáki *et al.*, 2012). Being a very novel technique, this has not been applied in BCIs yet. However, preliminary work with classification of VSDI data suggests that it can be used to decipher intentions of various populations of neurons and can therefore serve as a viable source of neural data for BCIs (Vainer *et al.*, 2009).

From the numerous non-invasive modalities available for recording neural signals, electroencephalography (EEG) is the most widely used one for BCIs due to its high temporal resolution, portability and low cost. Other modalities reviewed above have higher spatial resolution, but suffer from poorer temporal resolution, poor portability, and poor user convenience. As a result, these modalities are sparingly used in BCIs. Consequently, most of the methods described henceforth is in the context of EEG signals, although they can be extended to other signal types with little to no modification.

2.1.2 Preprocessor

The pre-processing step aims at improving the signal-to-noise ratio (SNR) of the recorded signal so as to reduce variability in the learned models of the brain state. This is accomplished by eliminating sources of noise, normalizing the signal, identifying and removing artifacts and formatting the signal in preparation for feature extraction.

Artifact Removal

Artifacts are features in the signal from external, unwanted sources that often mask the signal from the desired sources. It is therefore essential to identify such artifacts and remove them before feature extraction. Such artifacts can be physiologic or non-physiologic in nature. This section will delve into the physiologic artifacts encountered in EEG such as muscle artifacts (EMG), ocular artifacts (EOG and blinks), and cardiac (ECG) and breathing rhythms.

Muscle Artifacts (EMG) are segments of electromyographic (EMG) input generated by movement of the neck or facial muscles. Due to the proximity of the EEG electrodes to the muscles of the neck and face, their activation introduces large, high frequency activity (above 30 Hz) in the EEG trace.

Due to selective contamination of high frequencies specifically, such muscle artifacts can be effectively suppressed by applying a low pass filter. This approach is not feasible for BCIs sensitive to higher frequency EEG information. Under such circumstances, blind source separation techniques such as independent component analysis (ICA) are better at isolating the uncorrelated components of the signal (detailed explanation in section 2.1.3). Since muscle artifacts are uncorrelated with EEG data, it is effectively isolated and removed from the signal (Fatourechi *et al.*, 2007).

An alternate novel method of filtering EMG derived artifacts uses spatial filtering methods such as common spatial patterns (CSP) (detailed explanation in section 2.1.3). Traditionally used for classification purposes (Bashashati *et al.*, 2007), CSP features were found to be extremely sensitive to muscle artifacts (due to its spatially localized pattern) (Guger *et al.*, 2001). This property was exploited to

identify the CSP components corresponding to EMG activity and subsequently removing them.

Ocular Artifacts (EOG and blinks) One of the major sources of artifacts are eye blinks and eye motion (EOG), collectively called ocular artifacts (OA). They show up as isolated slow changing peaks in the EEG data (Figure 2.3).

OAs can be removed by using time domain and/or frequency domain methods (Kirkove *et al.*, 2014). Time domain methods, such as adaptive filtering (AF), create a morphological template of the artifact and subtract it from the segment of EEG. Despite having good speed performance, it suffers from alignment issues between the template and artifact. Frequency domain methods, such as discrete wavelet transform (DWT), do not suffer from this issue as it functions in the frequency domain by thresholding the coefficients in the frequency range corresponding to OAs.

There are further methods that use spatial filters such as ICA and CSP to identify components corresponding to OAs and remove them (Fatourechi *et al.*, 2007). These however require a large number of electrodes and longer processing times to be effective (Kirkove *et al.*, 2014).

Cardiac artifacts (ECG) The electrical activity of the heart introduces a periodic artifact at around 1 Hz (roughly the time taken for one cardiac cycle) which can be easily identified and removed using ICA (Iriarte *et al.*, 2003) and other wavelet based de-noising methods (Weidong Zhou and Gotman, 2015). Such methods work under the assumption of stationarity of the cardiac waveform.

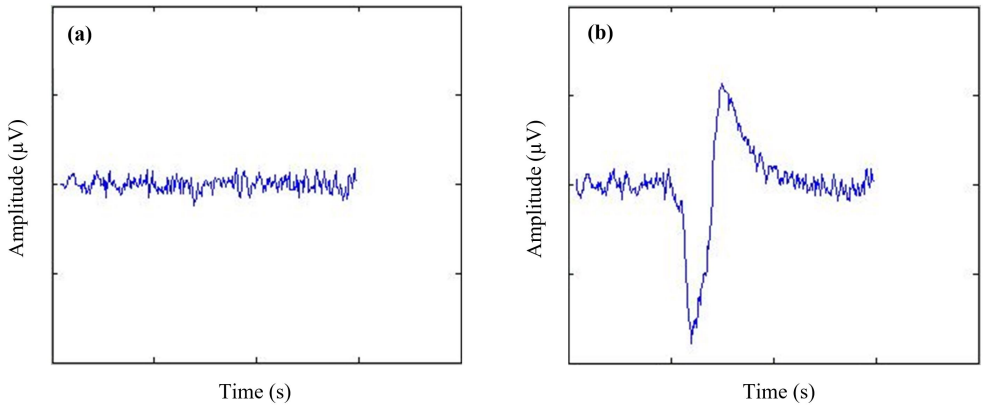

Figure 2.3: Morphology of a blink ocular artifact in EEG. (a) A clean segment of EEG recording, (b) An EEG segment contaminated with an ocular blink artifact

Filtering of Non-Physiologic Noise sources

Non-physiologic sources of noise are easier to remove from the signal due to their deterministic nature. One such common source of noise is power line noise at 50 Hz or 60 Hz. This is easily removed by using a notch filter of sufficient order at the specified frequency. Given the majority of signals of interest in EEG are in the range of 0 Hz - 40 Hz, applying a band pass filter with a pass band of 0 Hz to 40 Hz rids the signal of higher frequency line and instrumentation noise.

2.1.3 Feature Extractor

Once pre-processed clean signals are available, this step performs feature extraction and feature selection. Features are descriptors of the signal relevant to the task of classifying the brain state. Usually a large number of features are extracted from the signal. However, all features may not be relevant to the classification problem.

Hence, feature selection is carried out, resulting in a smaller subset of relevant features which will be passed to the classifier. Selecting the right features is critical to the performance of the BCI. The features should be measures that are different between different brain states that are to be classified. Also, the features need to be robust (i.e. not drift over time), in order to have an accurate model that does not become irrelevant over time.

Some commonly used features, and the feature extractors used to acquire them, are discussed here along with examples of BCIs that use them. All of them aim at computing a set of parameters which could serve as a descriptor of the signal.

Power Spectral Density (PSD) and Spectral Features

The Power Spectral Density (PSD) refers to the distribution of power across the frequency spectra and is defined as follows:

$$P_{xx}(\omega) = \lim_{T\to\infty} \frac{1}{T} E\{\left|\mathcal{F}_x^T(\omega)\right|^2\} \tag{2.2}$$

Where $E\{.\}$ represents the expected value operator and $\mathcal{F}_x^T(\omega)$ is the finite Fourier transform of the signal x given by Equation 2.3

$$\mathcal{F}_x^T(\omega) = \int_0^T x(t)e^{-i\omega t}dt \tag{2.3}$$

Mathematically, the PSD is also given by the Fourier Transform of the auto-correlation. It is exceptionally useful in describing the frequency distribution of the signal and is extensively used to study the amount of signal power present in each frequency band. This gives rise to numerous spectral features such as band power (for

each of the EEG spectral bands described in Table 2.1) describing the corresponding level of activity, and log power ratios which describe the relative power between a pair of bands. Equation 2.4 shows the relative band power $\mathcal{R}_{\alpha\beta}$ between the α and β bands, as computed from the corresponding band powers P_α and P_β.

$$\mathcal{R}_{\alpha\beta} = log\frac{P_\alpha}{P_\beta} \tag{2.4}$$

Such spectral features are useful in BCIs based on rhythms with a clear spectral signature (such as sensorimotor rhythms) where the power in the bands change between the different brain states. One other example of such a BCI is a meditation BCI which monitors alpha band power as its decrease signifies a relaxed or meditative state of mind (Aftanas and Golocheikine, 2001).

Coherence

Coherence features comprise of correlative information between the phase delays of signals in electrodes/voxels pairs (Khodayari-Rostamabad *et al.*, 2010), and are useful in tasks where multiple brain regions work together for a given task (such as motor imagery) (Hamedi *et al.*, 2016). It is therefore a feature representing the connectivity of various regions of the brain. Coherence is computed as follows (Yaesoubi *et al.*, 2015)

$$C_{xy} = \frac{P_{xy}}{\sqrt{P_{xx}P_{yy}}} \tag{2.5}$$

Where P_{xx} and P_{yy} are the power spectral densities (PSD) of two channels x and y, and P_{xy} is the cross spectral densities (Fourier Transform of cross-correlation) of the

signals x and y computed as follows

$$P_{xy}(\omega) = \lim_{T\to\infty} \frac{1}{T} E\{\mathcal{F}_x^*(\omega)\mathcal{F}_y(\omega)\} \tag{2.6}$$

Where $\mathcal{F}_x$ and $\mathcal{F}_y$ are the finite Fourier transforms (given by equation 2.7) of signals x and y respectively, at angular frequency ω and * represents the complex conjugate.

$$\mathcal{F}_x(\omega) = \int_{-\infty}^{\omega} P_{xx}(\nu)d\nu \tag{2.7}$$

Due to the ability of describing synchronized behavior of the brain, coherence measures have been used for BCIs using synchronized rhythms such as the sensorimotor rhythm (Leuthardt *et al.*, 2009).

Principal Component Analysis (PCA)

PCA is a statistical method of deriving a set of uncorrelated "components" from a set of potentially correlated data. These components are called the principal components of the decomposition and are sorted for descending variance, with the first component accounting for majority of the observed variance and the subsequent components accounting for progressively lower amounts of the observed variance.

Intuitively, this can be viewed as fitting an $n-1$ dimensional ellipsoid to the dataset with the long axis of the ellipsoid aligned along the data direction of maximal variance. PCA effectively describes a large dimensional dataset by a lower dimensional subspace. Mathematically, it is obtained by either a singular value decomposition (SVD) of the data matrix (Equation 2.8), or an eigenvalue decomposition of the data covariance matrix (Equation 2.10).

Singular Value Decomposition For a data matrix $\boldsymbol{X}$ of size $n \times p$ where n is the number of time points and p is the number of channels, the principal components (columns of $\boldsymbol{T}$) are given by

$$\boldsymbol{T} = \boldsymbol{U}\boldsymbol{S} \tag{2.8}$$

Where the SVD of the data matrix is

$$\boldsymbol{X} = \boldsymbol{U}\boldsymbol{S}\boldsymbol{W}^T \tag{2.9}$$

such that $\boldsymbol{U}$ is the left singular vector ($n \times n$ matrix), $\boldsymbol{S}$ is the singular matrix (an $n \times p$ rectangular diagonal matrix), and $\boldsymbol{W}$ is the right singular matrix ($p \times p$ matrix). The columns of $\boldsymbol{U}$ and $\boldsymbol{W}$ contain orthogonal unit vectors of lengths n and p respectively. This is the most efficient method to compute the principal components of the data and is therefore the more prominently used algorithm for PCA computation.

Eigenvector Decomposition For a data matrix $\boldsymbol{X}$ of size $n \times p$ where n is the number of time points and p is the number of channels, the principal components (columns of $\boldsymbol{T}$) are given by the projection of the data onto the eigenvectors (or principal axes) as follows:

$$\boldsymbol{T} = \boldsymbol{X} \cdot \boldsymbol{W} \tag{2.10}$$

Where $\boldsymbol{W}$ is the matrix of eigenvectors obtained by decomposing the $p \times p$ data covariance matrix $\boldsymbol{X}^T\boldsymbol{X}$ into its eigenvalues (diagonal of L) and eigenvectors (columns of $\boldsymbol{W}$) as follows:

$$\boldsymbol{X}^T\boldsymbol{X} = \boldsymbol{W}L\boldsymbol{W}^T. \tag{2.11}$$

Due to the efficient algorithms available to compute the principal components of

the signal, PCA can be computed in real-time and is hence an extremely useful feature extraction and reduction (due to its dimensionality reduction property) method for real-time BCIs (Das *et al.*, 2007), (Yu *et al.*, 2014). PCA has also been extensively used for denoising by identifying the principal components as noise components (as they account for the maximum variance) and removing them from the data (Nicolas-Alonso and Gomez-Gil, 2012). However, PCA is extremely sensitive to the scaling protocol used to scale the data and there is no set guidelines on how to pick the optimal scaling method. Also, the identified principal axes may not be the ideal axes for decomposing the data for classifying the different brain states as there is no provision of ensuring maximum class separation in PCA (something that is present in CSP).

Independent Component Analysis (ICA)

ICA is a blind source separation (BSS) method which attempts to decompose the signal into a set of mutually independent components. The assumption for linear ICA is that the recorded m-channel EEG signal $\boldsymbol{x}(t) = \{x_1(t), x_2(t), x_3(t), ..., x_m(t)\}$ is a superposition of a set of independent sources $\boldsymbol{s}(t) = \{s_1(t), s_2(t), s_3(t), ..., s_m(t)\}^T$. The coefficients that describe the contribution of each source is defined by the mixing matrix $\boldsymbol{A} = \{a_1(t), a_2(t), a_3(t), ..., a_m(t)\}$. This is shown in equation 2.12

$$\boldsymbol{x}(t) = \boldsymbol{A} \cdot \boldsymbol{s}(t) + \boldsymbol{n}(t) \tag{2.12}$$

Where $\boldsymbol{n}(t)$ is additive noise. Assumptions of low noise conditions lead to equation 2.12 becoming

$$\boldsymbol{x}(t) = \boldsymbol{A} \cdot \boldsymbol{s}(t) \tag{2.13}$$

Both the sources $\boldsymbol{s}(t)$ and the mixing matrix $\boldsymbol{A}$ are unknowns and need to be computed. The sources are estimated as follows

$$\boldsymbol{s}(t) = \boldsymbol{W} \cdot \boldsymbol{x}(t) = \boldsymbol{A}^{-1} \cdot \boldsymbol{x}(t) \tag{2.14}$$

Where $\boldsymbol{W} = \boldsymbol{A}^{-1}$. The coefficients of $\boldsymbol{W}$ vector are computed iteratively by using a cost function maximizing the non-Gaussianity of the computed product in equation 2.14, or minimizing mutual information (from the independence requirement). Numerous algorithms have been developed and used to obtain these weight matrices, such as the INFOMAX, JADE, FastICA, etc. (Kachenoura *et al.*, 2008) Due to the feature of independence, ICAs are great for identifying artifacts, which originate from a source independent of the EEG signal. In particular, it has been useful in identifying and isolating ocular artifacts from EEG data (Naeem Mannan *et al.*, 2016).

Common Spatial Patterns (CSP)

Common Spatial Pattern (CSP) is a spatial filtering mechanism that has been particularly useful for EEG data which can have distinctive spatial patterns for various brain states. CSP features store information on the variances of the different class models, maximizing the difference between the created models of the signal classes. Hence CSP features are especially useful in situations where robustness is desired (Müller *et al.*, 2008).

For a two class problem (classes A and B), the CSP features are best computed according to Nicolas-Alonso and Gomez-Gil (2012). Normalized spatial covariance ($\boldsymbol{C}$) from the input data $\boldsymbol{X}$ (of size $n \times p$ with n time samples and p channels) is

computed using equation 2.15.

$$\boldsymbol{C} = \frac{\boldsymbol{X}\boldsymbol{X}^T}{Tr(\boldsymbol{X}\boldsymbol{X}^T)} \tag{2.15}$$

Where $Tr(\boldsymbol{X}\boldsymbol{X}^T)$ represents the trace of the matrix $\boldsymbol{X}\boldsymbol{X}^T$, i.e. the sum of the diagonal elements of $\boldsymbol{X}\boldsymbol{X}^T$. Using equation 2.15, the normalized spatial covariance ($\boldsymbol{C}$) is computed for each trial of each class and then averaged, generating average covariance matrices $\bar{\boldsymbol{C}}_A$ and $\bar{\boldsymbol{C}}_B$ for classes A and B respectively. These are used to compute the composite spatial covariance for all trials as shown in equation 2.16

$$\boldsymbol{C}_c = \bar{\boldsymbol{C}}_A + \bar{\boldsymbol{C}}_B \tag{2.16}$$

An eigenvalue decomposition ($\boldsymbol{C}_c = U_c \lambda_c U_c^T$) is performed on $\boldsymbol{C}_c$, to obtain a matrix of eigenvectors U_c and a diagonal matrix of eigenvalues λ_c.

The Mahalanobis whitening transform $P = \sqrt{\lambda_c^{-1}} U_c^T$ is used to map U_c onto a space P where the variances are normalized such that the eigenvalues of $P\boldsymbol{C}_c P^T$ are equal to 1. This is applied to the $\bar{\boldsymbol{C}}_A$ and $\bar{\boldsymbol{C}}_B$ to obtain $\boldsymbol{S}_A$ and $\boldsymbol{S}_B$ such that they share common eigenvectors (shown in equations 2.17 and 2.18)

$$\boldsymbol{S}_A = P\bar{\boldsymbol{C}}_A P^T \tag{2.17}$$

$$\boldsymbol{S}_B = P\bar{\boldsymbol{C}}_B P^T \tag{2.18}$$

Due to the whitening transform, an eigenvector decomposition of $\boldsymbol{S}_A = M\lambda_A\ M^T$ and $\boldsymbol{S}_B = M\lambda_B\ M^T$ yields eigenvalue matrices that sum to the identity matrix $\lambda_A + \lambda_B = \boldsymbol{I}$. This implies that the largest eigenvalue in λ_A corresponds to the

smallest eigenvalue in λ_B, and vice versa. This maximizes the signal variance of class A, while minimizes that of class B (or minimizing common variance) This finally gives the CSP feature vector $\boldsymbol{Z}$ with the spatial filter matrix $\boldsymbol{W}$

$$\boldsymbol{Z} = \boldsymbol{W} \cdot \boldsymbol{X} \tag{2.19}$$

such that $\boldsymbol{W} = \left[M^T \cdot P\right]^T$

The CSP feature extraction procedure is equivalent to maximizing the Rayleigh quotient given in equation 2.20 (Samek *et al.*, 2012).

$$R(\boldsymbol{W}) = \frac{\boldsymbol{W}^T \bar{\boldsymbol{C}}_A \boldsymbol{W}}{\boldsymbol{W}^T (\bar{\boldsymbol{C}}_A + \bar{\boldsymbol{C}}_B) \boldsymbol{W}} \tag{2.20}$$

$$\max_{\boldsymbol{W}} \boldsymbol{W}^T \bar{\boldsymbol{C}}_A \boldsymbol{W} \text{ subject to } \boldsymbol{W}^T (\bar{\boldsymbol{C}}_A + \bar{\boldsymbol{C}}_B) \boldsymbol{W} - C = 0$$

Modifications of this procedure has created numerous variants of CSP for a multiclass problem (Grosse-Wentrup and Buss, 2008), sparse conditions (Goksu *et al.*, 2011) and extremely non-stationary situations (Samek *et al.*, 2012). CSP has been extensively used in BCIs due to its ability to characterize spatial differences and maximize the class models. In particular, it has been used for motor imagery (MI) based BCIs as MI is extremely localized and has a distinctive spatial pattern (Samek *et al.*, 2012).

Wavelet Transform

The wavelet transform (WT) is another method to characterize the time-frequency content of the signal. Traditionally, the short time Fourier transform (STFT) was used for this purpose, however, STFT descriptors suffered from the trade-off of a decreasing spectral resolution, with an increased temporal resolution (by using shorter

bins over which the FT is computed). The WT overcomes this problem by computing coefficients over multiple time and frequency scales. Additionally, WT uses wavelets as the basis set over which to compute the coefficients (compared to sinusoidal basis set in FT). This grants the WT considerable flexibility in characterizing signal patterns with characteristic time and frequency morphologies by using a suitable wavelet for the decomposition. The math underlying this transform is detailed in the Methods chapter.

In the context of BCIs, the WT has been used for denoising purposes, to remove ocular artifacts (Peng *et al.*, 2013) and to create feature vectors for classification of the brain state (Bostanov, 2004).

Numerous other feature extraction methods and features exist which can be used in BCIs. Selecting the right kind of features is crucial as some sets of features are more suited for certain kinds of BCI tasks. Sometimes, multiple sets of such features are combined to improve BCI performance.

2.1.4 Signal Classifier

After features characterizing the acquired signal are computed, they need to be classified into one of the many brain states. To accomplish this, a classifier is first trained on a training data set where the state of the brain during each trial is known *a priori*, and the features computed are used to generate models of the respective states. After training the classifier models, classification can be done on a trial by trial basis. The signal features of each incoming trial are compared to the created models of each state and the most probable state is identified by the classifier using a classification algorithm. This state is the predicted state of the subject's brain which is thereby

used to perform a task or generate an appropriate control signal if it is a mechanical BCI.

Various classification algorithms have been developed over the years which approach the problem of classification using either linear or non-linear methods.

Linear Classifiers

Linear classifiers use linear decision boundaries to separate the different classes of data. Despite being a very simple model, linear methods such as linear discriminant analysis (LDA) and linear support vector machines (SVM) provide good results under conditions where their assumptions are not violated. Their power is in their simplicity which allows for quick computations and updates in real-time.

Linear Discriminant Analysis (LDA) The working principle of this method is finding a hyperplane that separates the different classes present in the training data, and using it to classify new data. The features from the new data ($\hat{\boldsymbol{X}}$) are used to compute the side of the hyperplane the datapoint lands on (given by the sign of G) as shown in equation 2.21.

$$G(\hat{\boldsymbol{X}}) = W^T \cdot \hat{\boldsymbol{X}} + W_0 \tag{2.21}$$

where W and W_0 are the weights (normal vector to the hyperplane) and the threshold respectively, and are the learned parameters of this classifier. The offset of the hyperplane from the origin, along the direction of the normal is given by $\frac{W_0}{||W||}$.

Numerous methods exist to estimate W, most of which utilize the class means and the empirically computed covariance matrices. An example of a binary LDA is

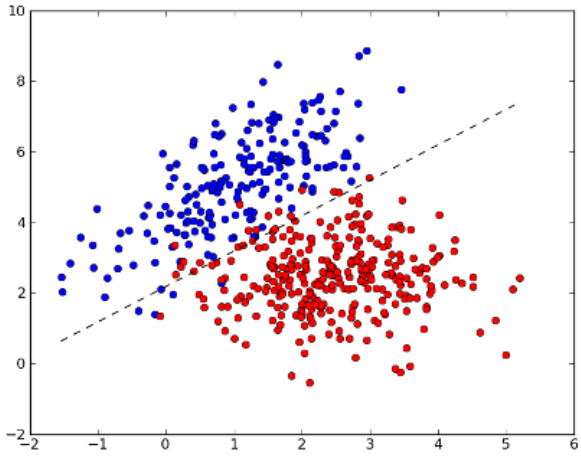

Figure 2.4: A binary LDA classifier. The data points from the two classes (red and blue), are separated by the black line (1 dimensional hyperplane).

shown in Figure 2.4.

Being computationally simple, LDA classifiers are excellent for a large number of BCI applications such as P300 based spellers and motor imagery based BCIs (Pfurtscheller and Guger, 1999), however, their performance deteriorates in conditions where the size of the feature vector is large, compared to the number of available training trials (Blankertz *et al.*, 2011).

Support Vector Machines (SVM) Another class of popular classifiers that have been used extensively in BCIs are Support Vector Machines (SVM). They can be of the linear or the non-linear kind.

Linear-SVM is a classifer with a classification approach similar to that of the LDA, with the additional constraint of optimizing the hyperplane to maximize its

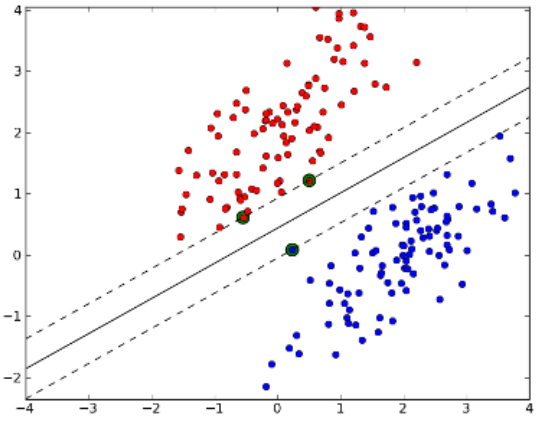

Figure 2.5: A binary linear SVM. The two classes of data (red and blue), are separated by the 1 dimensional hyperplane (black solid line) and the two support vectors (black dotted lines).

distance from the points closest to it, on either side. These margins are called the support vectors and are generally parallel to the decision hyperplane (Figure 2.5) and can be computed by the following optimization problem:

$$\text{"Minimize } ||W|| \text{ subject to } sign(G(\hat{\boldsymbol{X}})) \cdot \left[W^T \cdot \hat{\boldsymbol{X}} + W_0\right] \geq 1 \quad \forall\, \hat{x} \in \hat{\boldsymbol{X}}\text{"}$$

Non Linear-SVM In many problems, a linear decision boundary does not suffice due to the non-linear separation between the classes. Nonlinear-SVMs overcome this problem by projecting the input feature vector into a higher dimensional subspace, in which the decision boundary may be more linear (hyperplane-like) than in the lower dimensional feature space (Cover, 1965).

Instead of transforming the entire feature subspace into the higher dimensional subspace (which is computationally expensive), the kernel trick is used which replaces

the dot product in equation 2.21 with a non-linear kernel function ($k(\hat{x}_i, \hat{x}_j)$) where $\hat{x}_i$ and $\hat{x}_j$ are pairs of feature points in $\hat{\boldsymbol{X}}$. A common kernel used in BCIs (Kaper *et al.*, 2004) is the Gaussian kernel i.e. the Radial Basis Function (RBF) given in equation 2.22.

$$k(\hat{x}_i, \hat{x}_j) = exp\left(\frac{-||x-y||^2}{2\sigma^2}\right) \tag{2.22}$$

Numerous methods are adopted with the kernel to identify the weights (W) (Bashashati *et al.*, 2007). SVMs are particularly good for a classification problem with high dimensionality (large number of features) and small training sets. SVMs also have good generalizability of the created model due to the regularization step, which prevents overfitting of the training feature vectors. However, these additional steps reduce the operational speed of SVMs. Therefore, they are well suited for BCIs where the training trials and the classification trials are in two separate sessions.

Non-Linear Classifiers

As seen in Non-linear SVMs, some datasets need a non-linear decision boundary due to the non-linear separation between the classes in the input data. Non-linear classifiers also outperform their linear counterparts under high noise conditions. Some other non-linear classification algorithms are discussed below.

K-Nearest Neighbors (k-NN) Another non-linear classification method is k-nearest neighbors (k-NN) which classifies data according to the classes of the data point's neighborhood. In simplistic terms, the class of the data point is the class of majority of the k nearest data points. In case of a tie, the assigned class is the class of the nearest neighbor.

Being a simplistic classification algorithm, it has been used in some of the earlier BCIs (Blankertz *et al.*, 2002), however, its recent use has been limited due to the shortcomings associated with a localized classification method i.e. k-NN does not consider global structure of the data and classifies based on local structure which can often produce faulty results. Despite its fallacies, k-NN gives good results (78% to 97%) in conditions with low dimensional features spaces (Lotte *et al.*, 2007).

Artificial Neural Networks (NN) NNs are one of the most widely used classifiers in BCIs, owing to their unique design which allows them to learn features as it is exposed to more trials. They comprise of an input layer, multiple hidden layers and an output layer of artificial neurons that are either fully or partially connected with each other (Figure 2.6). The computed data features ($\hat{\boldsymbol{X}}$) are inputs at the input layer, while the class label is given by the output layer. The strength of connections (also known as weights W) between the layers is the parameter that is learned by the NN according to a learning rule and forms the decision boundary of the classifier.

The perceptron was the precursor to NN and it was proposed in 1958 (Rosenblatt, 1958). It was based on Hebbian learning as the learning rule. The NN generalized the perceptron by adding more layers and adapted a backpropagation based learning rule which facilitates more advanced learning.

Backpropagation based learning The features from a training trial are presented at the input layer ($L1$) of the NN initialized with random weights (W). If the neurons at the lower level are indexed by i and those at the upper level are indexed by j, the weight W_{ij} represents the connection between the i^{th} unit in $L1$ and the j^{th}

unit in $L2$. The input to the j^{th} unit in $L2$ is given by,

$$X_{L2_j} = \sum_{\forall\, i \in L1} Y_{L1_i} \cdot W_{ij} \tag{2.23}$$

The state of the neuron is determined using an activation function which takes into account the input to the neuron (X_{L2_j}). One example of such an activation function is the sigmoid function given by,

$$f(x) = \frac{1}{1 + e^{-x}} \tag{2.24}$$

The activation state (output) of the j^{th} unit in $L2$ is therefore, $Y_{L2_j} = f(X_{L2_j})$ (Gundogdu *et al.*, 2015). Equation 2.24 is applied iteratively, throughout the neural network until the output layer (L_{out}). The error between the output of the output layer and the actual class ($\hat{Y}$) of the training trial is computed as follows,

$$\varepsilon_{L_{out}} = Y_{L_{out}} - \hat{Y} \tag{2.25}$$

This error is back-propagated to the lower layers by using the differentiation chain rule as follows:

$$\varepsilon_{L_{out-1}} = W_{L_{out-1}} \cdot \varepsilon_{L_{out}} \cdot f'(X_{L_{out-1}}) \tag{2.26}$$

Where $W_{L_{out-1}}$ are the weights between the output layer and the penultimate layer. This is back-propagated throughout the network for all training trials to estimate the of the gradient of the error surface with respect to a cost function $K(W)$ as given by equation

$$\frac{\delta K(W)}{\delta W_{L_{k-1},L_k}} = \frac{1}{N_{train}} \cdot \Big[\sum \varepsilon_{L_k} \cdot Y_{L_{k-1}} + W_{L_{K-1}}\Big] \tag{2.27}$$

Where N_{train} is the number of training trials and $k = \{1, 2, 3, ..., m\}$ is the index of the layer. A suitable cost function is chosen for $K(W)$ such that network does not overfit the training data.

Classification Once the weights of the NN are learned, the features from the new trial are applied at the input layer. The activation of the neurons propagate to the output layer according to equations 2.23 and 2.24. The output of the neurons in the output layer is the class of the current trial. The output of the output layer neurons can also be interpreted as posterior probabilities by modifying the activation function at the output layer to the softmax function (equation 2.28)

$$Y_{L_{out},i} = \frac{e^{X_{L_{out-1},i}}}{\sum_{j=1,2,...N} e^{X_{L_{out-1},j}}} \tag{2.28}$$

Where i and j are indexes representing the signal classes and there are N signal classes in total.

Due to the multiple layered structure, various layers can learn subtle nuances in the input features and use those for classification, thereby making NNs a very powerful tool for identifying obscure features that are discriminative between the classes of interest. However, as a result of this, it generally requires a larger training set as compared to other classifiers and is also more unstable when used with non-stationary features (Bashashati *et al.*, 2007).

Affine Space Classifiers Some other classifiers use components of the features that explain the maximal variance in each class as models for classification. Such classifiers often use principal component analysis (PCA) to accomplish this task and

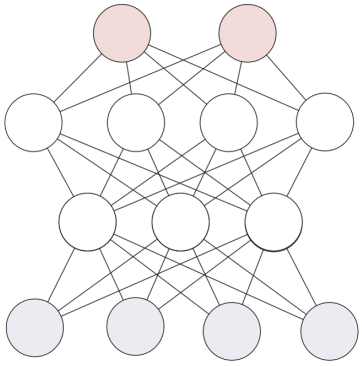

Figure 2.6: A neural network. This neural network has 4 neurons at the input layer (purple) and 2 neurons at the output layer (pink). There are 2 hidden layers that connect the input and the output layers (white).

use it to create an affine space model of each class. Classification is carried out by computing the distance between the computed features and the centroid of each class model. The class with the smallest distance is the assigned class label (Bruna and Mallat, 2011). Affine space classifiers allow for quick computation of the models, allowing for near-real time performance in BCI applications. Additionally, since the dimension of the modeled affine space is the only parameter pliable to change, finding the optimal dimensionality is quick for each BCI run making this an ideal choice for BCIs where the training and classification trials are acquired in a single session. For the purposes of this thesis, such a classifier is referred to as an affine space classifier. This type of classifier is further discussed in the Methods section.

2.1.5 The Actuator and Feedback

Once the data class has been assigned, the actuator performs the task defined for that particular class. For example, if the task was to move a robotic wheelchair either left

or right, and the current trial is classified as a right movement, the motors on the wheelchair are actuated to turn right. As a result of preforming the task, the user is able to sense the class recognized by the computer and this serves as the neurofeedback given to the user. This action completes the BCI loop. This process is repeated in a continuous loop for a real-time BCI. Depending on whether the classified task was the original intention of the user or not, he/she will modify their thought process to generate the correct class in the next run. This results in operant learning of the user (Kober *et al.*, 2013) and an improving BCI performance score. In addition to learning on the user's end, BCIs can also adapt by occasionally updating the class model in the classifier, leading to an even greater increase in BCI performance. This mode of BCI operation is termed optimized co-adaptation (McFarland and Wolpaw, 2011).

2.2 The BCI Neural Response

A wide range of tasks/activities can be selected as the BCI task, however, some are more favorable due to the changes they elicit in the recorded neural signal. Selecting the right task is crucial for a natural BCI that preserves the potential for high performance.

Tasks can be of two kinds - based on explicit physiological phenomena (such as a P300), or based on open-ended subtle features that describe abstract characteristics of the signal (such as entropy). BCIs that use the former category of tasks, purposefully elicit the physiological phenomena and train the subject to associate it with a given control signal. Such BCIs are called exogenous BCIs. This was the basis for the numerous P300 based spellers (Salvaris and Sepulveda, 2009). However, their work required considerable training on the subject's part and it was unnatural for the

subject to associate a stimulus to a control signal. BCIs that use the latter category of tasks, circumvent this problem by allowing the subject to directly think of the control signal and then, using abstract features, classify the brain state. Such endogenous BCIs suffer from poorer BCI performance due to a harder classification task, but are a much more natural BCI paradigm. Current research is focused on creating tools to improve BCI performance for such endogenous BCIs.

2.2.1 Exogenous BCI tasks

Exogenous tasks rely on massive changes in the recorded signal due to a physiological stimulus/event such as evoked responses in EEG to a light flashing. Due to the ease with which such features can be detected, they were used in some of the earliest BCIs, during a time before advanced signal processing techniques (Gao *et al.*, 2003), (Allison and Pineda, 2003).

Visual Evoked Potentials (VEP)

Flashing lights and/or lights moving across the visual field, resulting in changing visual patterns elicit a powerful response in the occipital lobe of the brain, collectively called visual evoked potentials (VEP). If light in the visual field is flashed at a frequency less than 2 Hz, transient VEPs (TVEPs) are produced. Such TVEPs can also be produced by changing visual patterns, however the specific morphologies of the TVEPs depend on the type of stimulus (Odom *et al.*, 2004). Flashing a light in the visual field at a frequency greater than 6 Hz leads to an oscillatory pattern in the occipital lobe called the steady-state visual evoked potential (SSVEP). The frequency components of the SSVEP signal are integer multiples of the frequency at

which the light is being flashed (Gao *et al.*, 2003). This paradigm can also be used to create a BCI speller where the subject looks at an array of letters which are flashing periodically and the desired letter produces an SSVEP of a very particular frequency profile. This is detected by the BCI and deciphered as the letter to be typed (Wang *et al.*, 2006). The drawback of such a BCI is the need for the subject to constantly stare at the desired letter. This is also not feasible for subjects with impaired eye or neck movements.

P300

P300 is a brief positivity in EEG signal over the parietal cortex when the subject is presented with a somatosensory, auditory or visual stimulus that is different from what the subject has been receiving previously. This is an evoked response to an unexpected stimulus that evolves around 300ms post-stimulus (hence the name P300). The large magnitude of the P300 peak makes it a popular choice in BCI control. The P300 has been used to create spellers for paralyzed subjects. Such spellers involve flashing arrays with letters and symbols at random, while the subject looks at the letter he/she wants to type. When the desired letter flashes, a P300 is elicited and is registered as the subjects choice. Practically, multiple trials are required to obtain sufficient confidence for selecting one letter, leading to very low typing rates (Salvaris and Sepulveda, 2009). Another problem with P300 based BCIs is the decline in P300 amplitude as the subject gets accustomed to the aberrant stimulus (Nicolas-Alonso and Gomez-Gil, 2012).

2.2.2 Endogenous BCI tasks

Sensorimotor activity

A voluntary movement, intention of movement and/or an imagined movement causes changes in the motor rhythms (Mu and Beta) of the brain. Such changes are collectively called the sensorimotor activity of the brain. Under resting conditions, mu and beta rhythms are well synchronized (some Beta rhythms are harmonic Mu rhythms (Pfurtscheller and Lopes, 1999)). However, initiating a voluntary movement, causes a desynchronization of these rhythms and deviation from symmetric morphology (as described in Table 2.1) (Pfurtscheller and Aranibar, 1977). The desynchronisation of the bands begin approximately 2s-2.5s before the movement onset and is called the event-related desynchronization (ERD). Once the movement is completed, the rhythms resynchronize in about 600ms post event offset in a process called event-related synchronization (ERS). Such synchronization changes are contralateral in nature, and can predict motor related activity on either side of the subject's body (Pfurtscheller and Aranibar, 1977). One of the earliest BCIs in the 1990s utilized this rhythm to control a cursor on a computer screen, moving it towards a target on the left or the right hand side (McFarland and Wolpaw, 2011). Despite providing good results, SMR based BCIs require extensive training on the subjects' part and constant practice is required to keep up the BCI performance.

Slow Cortical Potentials (SCP)

As the name suggests, SCPs are slowly varying potentials generated by the cortex. This arises from a threshold regulation mechanism for localized excitatory mobilization. As result of this mechanism, negative SCPs (such as Bereitschaftspotential, or

contingent negative variation - CNV) correspond to increased neuronal activity or excitatory mobilization while positive SCP correspond to decreased neuronal activation or disfacilitation (Neumann *et al.*, 2003). Self-regulation of SCP is possible and is the basis of using this potential in a BCI. Examples of such devices include a BCI to control the cursor on a screen based on the amplitude of the SCP potential (Nicolas-Alonso and Gomez-Gil, 2012). Such BCIs require extensive training for the subject to become reasonably good at them. Also the slower variation in this potential leads to a relatively low information transfer rate.

Chapter 3

Resting State

The brain is an extremely complex system, full of electrical and metabolic activity that modulates a person's personality, behavior and their abilities to perform simple or complex tasks. However, the brain is also involved in relaxing and upkeep of the metabolic processes of the body when the person is in a relaxed state i.e. not performing any tasks in particular. This state of the brain under zero cognitive load is termed as resting state (Meehan and Bressler, 2012).

Due to the different kinds of activities performed by the brain during each of these states - the task state and the resting state, the study of the brain needs to be divided into a task-based paradigm and a resting state paradigm. This section will review the current methods used in performing a task-based and a resting state analysis of the brain using two of the more prominent functional imaging modalities - fMRI and EEG.

3.1 Resting State Analysis Techniques

Task-based Analysis All of the early work in understanding the functional state of the human brain was task-based in nature. In this, the subject would be presented with a stimulus or be asked to perform a cognitive or behavioral task, while their brain was being monitored. A popular task-based study design is a block design or a variant of the block design in which the task condition is alternated with a rest condition or multiple task conditions. Another popular design is the oddball paradigm in which a variant target stimulus is presented amongst other baseline stimuli. Both of these designs provide contrast between the active state of the brain and the inactive state. The regions of elevated activity are considered to be the "active" regions of the brain, and therefore the regions associated with the stimulus, task or behavior studied in the experiment. Such methods have been used to study visual responses (Clark *et al.*, 2000), auditory responses (Linden *et al.*, 1999), ERPs (Van Veen and Carter, 2002), and emotional and behavioural responses (Mostofsky *et al.*, 2003).

Despite considerable success, such analyses are difficult due to the very low SNR and correspondingly low contrast-to-noise (CNR) ratio between the active and inactive states. The neurometabolic changes corresponding to task related activation is around 5% of the resting level (Meehan and Bressler, 2012). Majority of the brain's energy consumption is attributed to resting neural activity i.e. the resting state. Thus understanding brain function has changed from the study of task related localized activation to better understanding the distributed brain networks.

Resting State Analysis Due to the absence of a contrasting condition, resting state analysis requires more advanced signal processing techniques to filter out noise

and identify intrinsic nodes of connectivity in the resting state. More advanced techniques can even map out brain functional connectivity in the resting state and monitor changes over time. Some common methods used for such analyses are reviewed below.

3.1.1 Signal Denoising

Since resting state analysis depends on detection of deterministic fluctuations for identification of functional networks, effective denoising is essential. Denoising steps are routine for fMRI analysis.

Motion correction Head motion is a common source of noise due to the long acquisition time associated with an fMRI scan. Moving the head shifts the physical location of each voxel, thereby misaligning the voxels across different time points. If this is not corrected for, the BOLD time series of one voxel will be contaminated by the BOLD time series from the neighbouring voxels. Correcting for this motion first involves computing the amount translation and rotation by comparing each time point to a reference scan (often the first scan of the time series, but not necessarily). This is shown in Figure 3.1. The movement is assumed to be rigid, and hence transformation matrices for each time point can be computed from the movement information, realigning each time point to the reference scan. Once, complete, each voxel is aligned with the corresponding voxel across all time points.

Temporal filtering The resting state networks have been found to generate very low frequency activity (< 0.1Hz) (Whitfield-Gabrieli and Nieto-Castanon, 2012) that is coherent and correlated between different regions of the same network. In order to suppress noise outside this spectral region, a bandpass filter with corner frequencies

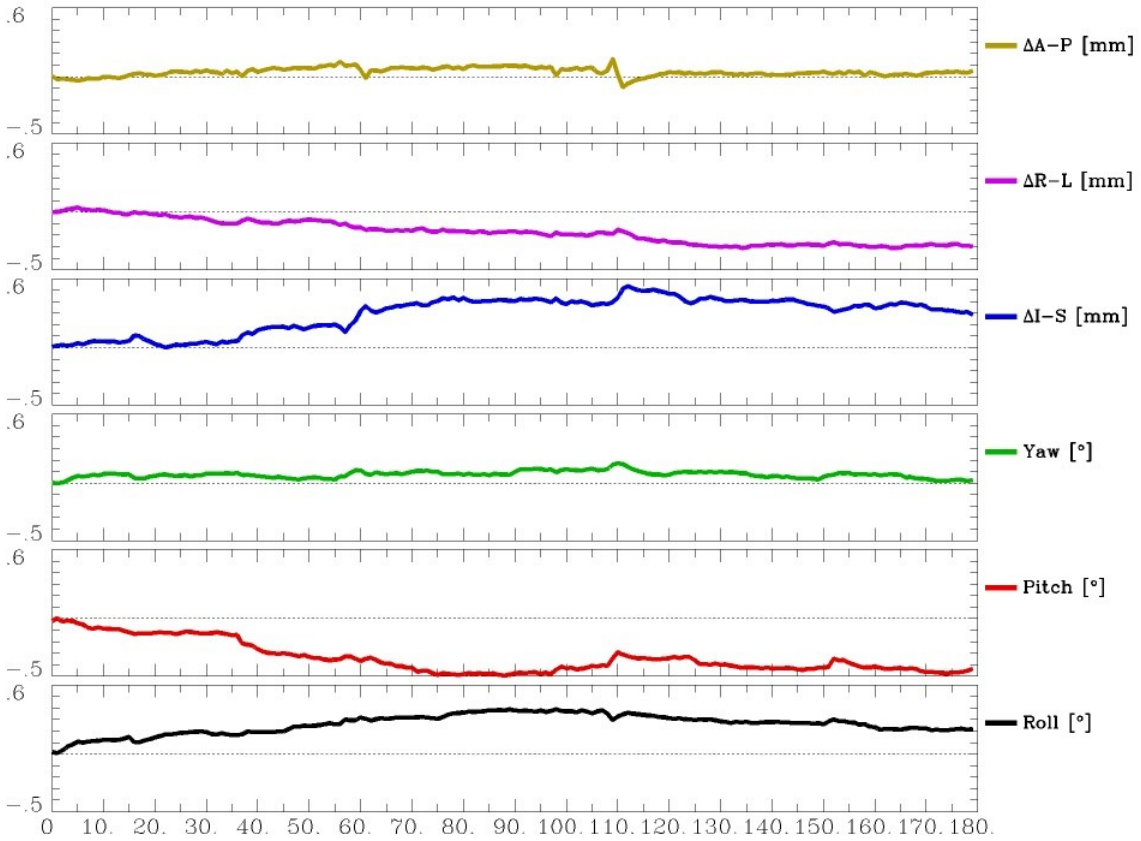

Figure 3.1: The 6 motion parameters (x, y, z, Roll, Pitch and Yaw) estimated from a subject's BOLD scan. The maximum motion is less than 0.6mm which is within the acceptable limit (< 2mm). The motion parameters were computed using the 3dvolreg program from AFNI (Cox, 1996)

of 0.008Hz and 0.09Hz is applied to the BOLD signal. This suppresses high frequency instrumentation noise, static offsets (0Hz). Cardiac activity ($\sim$ 1Hz) is aliased into the low frequency region (0.04Hz) due to the low sampling rate of BOLD scans (2 - 3 seconds). Hence, they need to be removed using other methods (Murphy *et al.*, 2013).

Spatial blurring One trick to increase SNR is by spatially averaging the signal of neighboring voxels using an averaging kernel such as a Gaussian kernel with a designated line width (usually 2mm). In addition to increased SNR, this also results in reduced variability while comparing scans from multiple subjects or computing group level statistics (LaConte *et al.*, 2003).

Coregistration to standard space Once the BOLD scans have been motion corrected, temporally filtered and spatially blurred, they can be co-registered to a standard brain atlas. The process of co-registration warps the acquired scan into the atlas space. This allows for the identification of brain regions, enabling comparisons to current literature and other scans. Some commonly used standard brain atlases are the MNI atlas (http://nist.mni.mcgill.ca/), and the Talairach atlas (Talairach and Tournoux, 1988).

3.1.2 Network Analysis

fMRI

The first resting state network (RSN) was identified by Biswal *et al.* (1995) when the left and right motor cortices showed correlation in their spontaneous BOLD activation. Since then, numerous other resting state networks have been identified, such

as the default mode network (DMN), salience network (SN) and central executive network (CEN) (Meehan and Bressler, 2012).

The goal of resting state fMRI analysis is to identify the networks responsible for the spontaneous activity in the absence of a cognitive task, and characterize their morphology and activity pattern. Two prominent methods exist to identify these networks.

Seed-based method involves the computation of the correlation between a predefined seed voxel or region of interest (ROI) and all other voxels with the hypothesis that regions pertaining to the same network will have a higher correlation of spontaneous BOLD activation (Biswal *et al.*, 1995). This approach is ideal when there is *a priori* information about the seed voxels and/or the researcher is interested in specific networks which have well known seeds (such as the DMN) (Cole *et al.*, 2010).

ICA-based Decomposition method approaches the RSN analysis using a blind source separation technique. An ICA is applied to the BOLD time series, decomposing the signal into its independent components (sources). The generated components usually represent the major RSN identifiable in the BOLD scan (Cole *et al.*, 2010). They also contain some components corresponding to the cardiac rhythm and CSF flow. Isolating these noise sources involves discarding all components that show activation outside gray matter regions (Beckmann and DeLuca, 2005). This method works only when there is more than one subject and group level networks need to be identified. For such an analysis, the BOLD data from all subjects are concatenated into one and fed into the ICA algorithm.

EEG

Studying the connectivity patterns from rsEEG data involves methods of correlative analysis similar to those discussed in Chapter 2 such as coherence between pairs of electrodes and their phase lags. Another popular method of deriving RSN like information from rsEEG data, is microstate analysis. Microstates are quasi-stable patterns in the time course of EEG voltage patterns across the head which last for approximately 100ms before switching to another quasi-stable pattern. Clustering analyses have identified 4 major EEG microstates which are considered as the quantized blocks of thought and emotion (Milz *et al.*, 2015). Having found these in a large group subjects, the microstates identified are universal and are analogous to the RSNs identified using BOLD data. However, the time scale over which microstates evolve is much shorter (milliseconds) than the RSNs (seconds).

Despite this difference in time scales, significant correlations were found when EEG microstate sequence data was time convolved with the haemodynamic response function (a major correlate in BOLD signal) and then compared with BOLD data from the same time period (Van de Ville *et al.*, 2010). This suggests that the RSNs identified using BOLD may actually be composed of multiple EEG microstates. Stemming from this possibility, one of the major goals of this project is to better characterize this relation between an EEG microstate and a BOLD resting state network.

3.2 Advantages and Shortcomings of the Resting State

The resting state provides crucial information regarding the integrity and functionality of the RSNs. Differences in the morphology and structure of these RSNs have been observed in subjects with mTBI (Mayer and Bellgowan, 2014), depression (Greicius *et al.*, 2007) and ADHD (Castellanos *et al.*, 2008).

The resting state EEG (rsEEG) signal also captures spontaneous neural activity that has been found to be indicative of neural development (Boersma *et al.*, 2011), epilepsies (Kerr *et al.*, 2012) and other neurological disorders (Lehembre *et al.*, 2012). However, there is active debate regarding what exactly can be considered the "Resting State" of the brain. Most of the resting state studies request the subject to "not think of anything in particular" while keeping their eyes closed or open. Despite this instruction, thoughts do wander through the mind of the subject, and he/she attempts to remove them which in itself is a task. Hence the concept of a "Resting State" is flawed and could be considered as an open ended state where the brain wanders from one task to another quickly. This is evident in the quickly changing microstate sequences seen in rsEEG, where the brain can be interpreted as switching between attention and visual tasks rapidly. Hence, the term "resting state" is a misnomer.

Chapter 4

Simultaneous EEG-fMRI

Both EEG and fMRI are popular tools to probe the functional activity of the human brain. However, both have certain drawbacks owing to the nature of signals they are sensitive to. EEG has extremely high temporal resolution, however, it suffers from poor spatial resolution due to the factors discussed in Chapter 2. On the other hand, fMRI has comparatively excellent spatial resolution, but poor temporal resolution due to the acquisition time of fMRI scans and the lag introduced by the haemodynamic response. It would therefore be beneficial to combine the two modalities together to obtain EEG and fMRI signals concurrently, providing high temporal and spatial resolutions respectively. This chapter describes the acquisition of simultaneous EEG-fMRI recording and some of the common analysis techniques associated with such recordings.

4.1 Recording Setup

The equipment used in simultaneous EEG-fMRI recordings are specially designed to be compatible with the MRI. The resistors and electrodes used are made from MRI compatible material and the circuitry on board the amplifiers are shielded to minimize any potential effect by the large MRI B_0 magnetic field. Furthermore, the recording computer is placed outside the magnet room, with the amplified EEG data being transmitted via optic fiber cables going through the MRI room wave guide. This setup ensures the integrity of the MRI magnet room RF shielding, while allowing the investigator to record EEG data while the MRI is scanning. A schematic of the setup is shown in Figure 4.1.

4.2 EEG-fMRI Signal Analysis

The acquisition of MRI data during concurrent EEG acquisition introduces a host of artifacts into the EEG signal. The most prominent of these artifacts are the gradient artifacts (GA) and ballistocardiogram (BCG) artifacts, which are discussed below.

4.2.1 Gradient Artifacts (GA)

During BOLD fMRI scanning, the MRI gradients switch back and forth rapidly to acquire multiple full brain images during the course of the scan. These rapidly switching magnetic fields induces a voltage in the electrodes of the EEG cap (according to Faraday's law). These show up as massive spikes in the EEG signal trace and completely mask the underlying EEG data (Salek-Haddadi *et al.*, 2003).

Numerous approaches have been developed to remove such GAs (Ritter *et al.*,

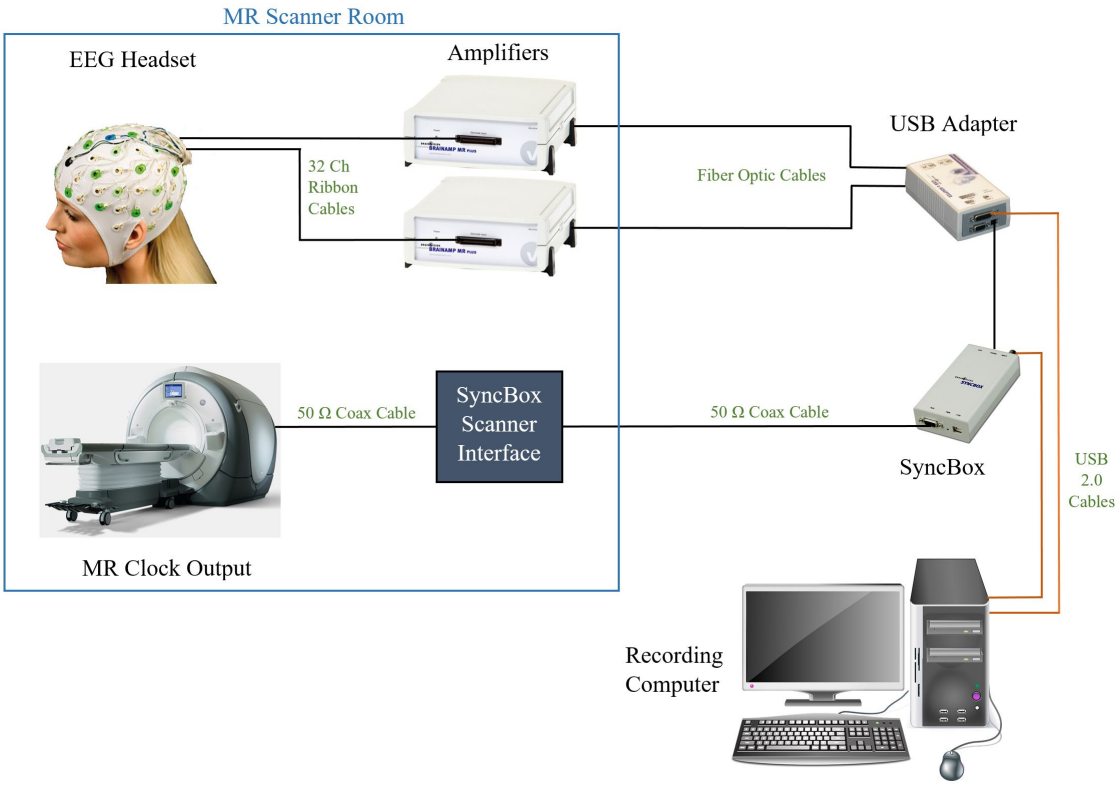

Figure 4.1: The equipment setup for an EEG-fMRI system showing the components in the MRI scanner room (blue box), and the recording equipment outside the scanner room. The SyncBox is required to sync the clocks of the scanner and the acquisition computer. The setup closely followed guidelines listed in the BrainProducts BrainAmp MR setup guide

2007) - Adaptive filtering, optimal basis set removal (OBS), alignment and subtraction (ITAS), and a realtime carbon-wire loop based method (van der Meer *et al.*, 2015). Most of these methods have been combined to provide robust and reliable filtering properties. One of the most popular combinations is the FASTR algorithm (Niazy *et al.*, 2005) implemented in the EEGLAB toolbox (Delorme and Makeig, 2004). It can be downloaded from http://fsl.fmrib.ox.ac.uk/eeglab/fmribplugin/.

Another well packaged set of GA filtering tools is the FACET toolbox (Glaser *et al.*, 2013) for MATLAB, which implements sections of FASTR along with another algorithm FARM, useful for EMG acquisitions in the scanner. The FACET toolbox is available at https://github.com/hansiglaser/facet

All algorithms work on a basic framework set by Allen *et al.* (2000). They create a GA model by averaging segments of gradient artifacts. The deterministic nature of these artifacts allows for the use of such a model to describe the GAs throughout the signal block. The input signal (x) is segmented into the recurring segments of GA using the gradient markers representative of the gradients switching on and off. The segmented data is averaged to obtain the GA model (y).

The FASTR Algorithm

The segmented input signal and the GA model are interpolated to a higher sampling rate, aligned and then subtracted.

$$z_k = x_k - y \tag{4.1}$$

where, x_k and z_k are the raw version and filtered version of the k^{th} epoch. The residual artifact in the filtered signal is further reduced by using an optimal basis set (OBS)

algorithm (Niazy *et al.*, 2005). A temporal PCA is performed on the GA model and the filtered signal. The PCA components of the signal are then fitted to those of the GA model, and are removed if the fit is significant. Any further residuals are removed by using an RLS adaptive filter.

The ITAS Algorithm

This is a variant of the FASTR algorithm, where the template used for subtraction is generated by giving a greater weighting to artifacts in the epochs closer to the current epoch during averaging. Such an algorithm helps in compensating for any drift in the template (Ritter *et al.*, 2007). An example of such a weighting is shown in equation 4.2

$$y_k = \frac{\sum_{i=1}^{n} w^{|k-i|} \cdot x_k}{\sum_{i=1}^{n} w^{|k-i|}} \tag{4.2}$$

where w is the weight factor (0.9) and n is the total number of epochs available. This template is then subtracted from the raw signal for the k^{th} epoch as follows

$$z_k = x_k - y_k \tag{4.3}$$

4.2.2 Ballistocardiogram (BCG) Artifacts

The subtle movements caused by the cardiac rhythm generates a pulse artifact in the EEG trace. Under normal conditions, this artifact is negligible, however, it is amplified to the level of brain signals by the large B_0 magnetic field when recording inside the scanner. Consequently, it needs to be removed as it may confound other EEG analysis downstream.

Multiple approaches exist to remove such BCG artifacts - subtracting the aligned ECG waveform (or its median waveform) from the signal (Allen *et al.*, 1998) (de Munck *et al.*, 2013), subtracting a dynamically computed template (Kruggel *et al.*, 2000), and ICA (Srivastava *et al.*, 2005). OBS can also be used to remove BCG artifacts using the assumption that each artifact instance is a linear combination of a set of orthogonal basis functions. This is used to create an accurate model of each instance of the of the artifact and subtract it from the signal (Niazy *et al.*, 2005). Lastly, data driven methods (Gonçalves *et al.*, 2007) and wavelet transforms (Wan *et al.*, 2006) can also be used to generate the templates for subtraction.

4.3 Applications of EEG-fMRI scanning

Acquiring neural data using two simultaneous modalities at two different time scales provides a lot of flexibility in the types of analyses that can be performed. Traditionally, analyses could be classified into one of two approaches - EEG informed fMRI and fMRI informed EEG analyses.

4.3.1 fMRI-informed EEG

One of the most popular analyses performed on EEG is source localization which tries to find the location of the dipole source causing the EEG spatial pattern observed. This is an inverse problem with no unique solution and usually requires a lot of assumptions to sufficiently constrain the problem. The fMRI data can be used in this regard to constrain the EEG source localization problem to obtain a more accurate solution with fewer assumptions (Meir-Hasson *et al.*, 2014).

4.3.2 EEG-informed fMRI

To study the fMRI correlates of EEG data, the EEG signal is time convolved with an estimate of the haemodynamic response function, bringing the time resolution of the EEG signal at par with the BOLD signal. The EEG signal is then used for correlations with fMRI data or as a regressor in a GLM to identify interactions with the BOLD signal. Such an analysis has led to identification of BOLD correlates of EEG evoked potentials and even shifts in EEG band power (Zotev *et al.*, 2014). Another application was discussed in Chapter 3 when the microstate sequence from EEGs correlated with fractal properties of BOLD signal (Van de Ville *et al.*, 2010). EEG-informed fMRI analyses have also been used to identify the foci of intractable seizures for surgical planning purposes (So, 2000).

Chapter 5

Hypotheses and Objectives

The increasing use of BCIs and advanced techniques like resting state fMRI and EEG analyses has led to a massive boom in neurological information over the past few decades. However, due to aspects discussed earlier, some of these techniques are more accessible and economically feasible than the others, one example of which is EEG, as compared to fMRI. EEG is a modality that is relatively cheap to install and operate, while MRIs entail large installation and operational costs. However, functional studies preferentially use MRI to probe the functional networks in the human brain due to its high spatial resolution and the option of comparing their results with the extensive body of fMRI work in characterizing functional networks.

Although standalone EEG has been used to investigate the brain's functional networks (Bullmore and Sporns, 2009), such data cannot be directly compared to the corresponding networks obtained from fMRI data. Investigating the relationship between multimodal information such as simultaneous EEG-fMRI, could potentially create such a direct link, reducing the need for using the more expensive modality (fMRI). One of the primary goals of this thesis is the characterization of this link in

a healthy population. Due to the varying time scales of EEG and fMRI signals, each fMRI resting state network is hypothesized to be a temporal combination of multiple EEG resting state networks (called microstates). This information is expected to characterize the pattern of healthy functional connectivity.

Functional connectivity can characterize the functional integrity of the brain network connections, however, it cannot describe their cognitive manifestations. Hence, a second protocol which is sensitive to the cognitive integrity of the subject, would be useful in characterizing the cognitive implications of these functional networks. BCIs are one such protocol.

Since BCIs require the subject to actively control their neural activity using neurofeedback (Zotev *et al.*, 2014), the model of neural activity generated is that of the brain under cognitive load. This is reflected in the modulation of BCI performance by a host of cognitive parameters such as working memory, and executive function (Sprague *et al.*, 2015). Hence, BCI performance of a subject can provide important information regarding the cognitive integrity of a subject. Despite the recent boom in BCI research, its application has been limited to providing an alternate method of controlling computers and prosthetics for patients with severe motor disabilities such as locked-in patients and amputees (Lance *et al.*, 2012). This is the first known application of BCI as a metric of cognitive integrity.

Given the dependence of BCI performance on the recognition of a particular pattern of neural activation, any changes to this pattern due to an underlying pathophysiology would negatively affect its performance. Detecting such changes in BCI performance could render it useful as a potential tool for identifying abnormal activation patterns in an active brain (not resting state). This therefore allows a BCI to

diagnose and track the recovery of a neuropathology in a patient. In order to accomplish this, a robust model of the normative brain activity is essential. This thesis, thus aims to characterize the performance profile of such a BCI, on a healthy population, creating a model of the normative activation and BCI performance. In the future, this may potentially be used to detect cognitive deficits due to brain disorders such as a mild traumatic brain injury.

For many brain disorders, in addition to impaired cognitive abilities, there is modified neural activity even under zero cognitive load i.e. in the resting state (Castellanos *et al.*, 2008). Hence, the characterized normative functional connectivity could help in identifying such changes in the resting state activity of the brain. This information, in addition to the cognitive metrics from the BCI, would provide a more comprehensive set of features for use in characterization and identification of the suspected brain disorder.

The proposed framework thus contains a BCI task section and a resting state section which are detailed in the following chapter.

Chapter 6

Methods

6.1 Protocol Desciption

Data was acquired from a population of 10 healthy subjects (22 ± 3.6 years). Each session of scanning took approximately 2 hours with the data acquisition segment taking place within the MRI scanner and lasting for 45 minutes. The first segment of the experiment was the application of an appropriately sized EEG cap and debriefing the subject which took approximately 60 minutes. A BrainProducts (Brain Products GmbH, Gilching, Germany) 64 channel MR compatible EEG cap was used (BC-MR 64). Conductive gel was applied at the site of each electrode on the scalp to improve signal quality. An ECG lead was attached to the subjects back to record ECG signal and correct for ballistocardiographic (BCG) artifacts in the recorded EEG. The subject was then taken into the magnet and set up with headphones and the projector screen. All MRI scanning was performed using a GE MR750 3T MRI and 32 channel head, neck and spine (HNS) RF coil (General Electric Healthcare, Milwaukee, WI).

Once the subject was comfortably in the scanner, a 5 minute 18 seconds long anatomical scan was run in order to obtain a high resolution structural image of their brain. The images were acquired using an IR prepped (TI = 450 ms) axial 3D FSPGR sequence and the head section of a head and neck (HNS) coil. An in-phase echo time (TE) of 2.2 ms, repetition time (TR) of 7.7 ms and a flip angle of 12 degrees was used. The slices were acquired with 2mm slice thickness, 320 frequency encoding points, 192 phase encoding points and a field of view (FOV) of 24. The frequency direction was in the antero-posterior direction (AP). The fMRI scans were acquired using a 2D GRE EPI sequence with a TE of 35 ms and TR of 2000 ms. A flip angle of 90 degrees was used and the number of points in the frequency and phase directions were 64. The frequency direction was right-left direction (R/L) with a FOV of 24. Each volume consisted of 39 slices acquired interleaved, at a slice thickness of 3.8 mm. A total of 150 volumes were acquired.

The acquired anatomical images were used to prescribe all functional scans. Three sets of BCI EEG-fMRI scans were acquired, each lasting 10 minutes. During each scan, the subject was instructed to look at a fixation cross. A musical tone (piano note) was played via a MR Confon headset (MR Confon GmbH, Magdeburg, Germany) for a duration of 2 seconds, following which the subject was instructed to imagine the tone they just heard. The imagery section lasted for 4 seconds. The EEG data collected during this section was then used by the BCI to classify the tone imagined and this was played back to the subject for a duration of 2 seconds. This sequence of events constituted one trial. This was repeated multiple times with low (C2 = 65Hz) and high (C6 = 1046Hz) piano tones played in a random order to collect a total of 50 trials from each subject.

A 5 minute long Resting State EEG-fMRI scan followed the BCI section. For this section, the subject was instructed to close their eyes and not think of anything in particular.

EEG signal was acquired using a BrainAmp MR (Brain Products GmbH, Gilching, Germany) amplifier system recording 64 channel data at a sampling rate of 5000Hz. Upon completion of the scan, the cap was taken off the subject and cleaned. The acquired data was backed up on the lab server.

6.2 Data Analysis

6.2.1 Gradient Artifact (GA) Filtering

Simultaneous recording of EEG-fMRI data, introduces considerable additional artifacts in the EEG signal as discussed in Chapter 4. The FASTR algorithm was used for filtering the resting state EEG data acquired. In the interest of speed, the BCI sections used a custom filtering algorithm that relies on the assumption that the noisy input signal (x) is a convolution of the EEG signal (x_{EEG}) and the gradient noise (n_{GA}).

$$x = x_{EEG} \star n_{GA} \tag{6.1}$$

The clean EEG signal (x) is recovered by de-convolving the EEG signal and the gradient noise, estimated using the GA model. De-convolution is difficult in the time domain, however, can be accomplished by simple division in the frequency domain. Applying a Fourier transform ($\mathcal{F}$) to the above equation,

$$\mathcal{F}[x] = \mathcal{F}[x_{EEG} \star n_{GA}] \tag{6.2}$$

$$X = X_{EEG} \cdot N_{GA} \tag{6.3}$$

The clean estimated EEG signal can then be expressed as

$$x = \mathcal{F}^{-1}\left[\frac{X}{N_{GA}}\right] \tag{6.4}$$

Given that N_GA is non-zero.

For a practical implementation, the FFT was used for quick computation of the Fourier transforms. After applying one of the above mentioned gradient artifact corrections, the filtered data was down sampled to 256 Hz, windowed, and then band-pass filtered (0 to 45 Hz Butterworth).

6.2.2 Brain Computer Interfacing (BCI)

The BCI data was analyzed in real-time using MATLAB on the acquisition computer. The FieldTrip Toolbox (Oostenveld *et al.*, 2011) was used to import the incoming EEG data stream into MATLAB. Additionally, markers for the onset of MR gradients was also recorded. The data was filtered using the Fourier transform algorithm (described in section 6.2.1) to remove the gradient artifacts (GA). The data was then filtered using a 0.4 Hz to 40 Hz Butterworth bandpass filter to remove high frequency noise. Downsampling was carried out to reduce the sampling rate from 5000 Hz to 256 Hz.

The BCI needs to compute features upon which the classifier is trained. The feature set chosen for this BCI was the scattering wavelet coefficients computed by the scattering wavelet transform (ScWT).

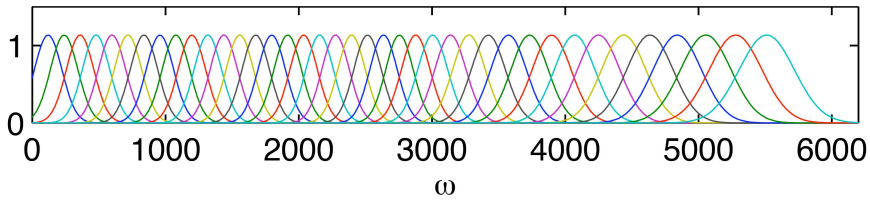

Figure 6.1: A Gabor wavelet filter bank. Andén and Mallat (2011)

Wavelets are families of functions that are created by scaling (dilating) and translating a mother wavelet (ψ). The wavelet filter bank computed from a mother wavelet $\psi(t)$ with an octave bandwidth of $1/Q$ is defined as follows:

$$\psi_j(t) = a^{-j}\psi(a^{-j}t) \tag{6.5}$$

where $a = 2^{1/Q}$, $j \leq J$ and $j \in \mathbb{Z}$

An example of such a wavelet filter bank is shown in Figure 6.1, where the mother wavelet is the Gabor wavelet.

For a one dimensional signal x(t), the wavelet transform is computed by convolving the signal with a wavelet filter bank. The wavelet transform operator is therefore,

$$\mathcal{W}_j x = \{x \star \psi_j\}_{j \in 1,2,\ldots,J} \tag{6.6}$$

This computes a bank of wavelet coefficients

$$\mathcal{W}x = \begin{pmatrix} x \star \phi_j(t) \\ x \star \psi_j(t) \end{pmatrix} \tag{6.7}$$

Where $\phi_J(t)$ is a low pass filter. Despite creating a richer description of the signal

by sampling the higher frequency domain at smaller scales, the wavelet coefficients are not translation invariant. One common trick to obtain translation invariance is to introduce averaging. However, this cannot be done with the wavelet transform as the wavelets have zero mean. This necessitates a modification to the wavelet transform that adds local translation invariance to its coefficients. The scattering wavelet transform (ScWT) attempts to accomplish this by introducing a non-linearity in the transform operator which makes the average value non-zero (Mallat, 2012).

The non-linearity introduced by the ScWT is a complex wavelet modulus operator $U[j]x = |x \star \psi_j|$. The result of averaging the modulus operator will therefore be non-zero and translation invariant.

$$S[j_1]x = \int U[j_1]x \cdot dx = \int |x \star \psi_{j_1}| \cdot dx \tag{6.8}$$

This is one scattering wavelet coefficient. However, the averaging leads to loss of high frequency information which is non-ideal (Andén and Mallat, 2011). This information is recovered by computing the wavelet decomposition of $|x \star \psi_j|$.

$$S[j_{12}]x = |x \star \psi_{j_1}| \star \psi_{j_2} \tag{6.9}$$

This represents the scattering coefficient derived from the path j_{12}. A complex modulus operator further is applied to this decomposition and averaged as well. This procedure continues iteratively to create a cascade of scattering coefficients.

A path is defined as a sequence of scaled wavelets $p = \{j_1, j_2, j_3, , j_m\}$ up to a level m. Each path defines its own unique ordered non-commutative product of modulus

operators:

$$U[p]x = U[j_m]x \cdot ... \cdot U[j_3]x \cdot U[j_2]x \cdot U[j_1]x = ||||x \star \psi_{j_1}| \star \psi_{j_2}| \star \psi_{j_3}| ... \star \psi_{j_m}| \quad (6.10)$$

For computational simplicity, the averaging can be carried out by a low pass filter $\phi_J(t) = 2^{-2J}\phi(2^{-J}t)$. This carries the low frequency information past the scale 2^J. Hence, the scattering wavelet coefficient for a path p is defined as follows

$$S_J[p]x(t) = U[p]x \star \phi_{2^J}(t) = \int U[p]x(v)\phi_{2^J}(t-v) \cdot dv \quad (6.11)$$

Since the scattering coefficient for a particular path can be computed using convolution, the coefficients for all paths can be efficiently computed using a convolutional network (as shown in Figure 6.2). This network computes a vector of scattering coefficients $S_Jx(t)$ of length $m+1$, where m is the number of levels in the network.

$$S_Jx(t) = \begin{pmatrix} x \star \phi_{2^J}(t) \\ |x \star \psi_{j_1}| \star \phi_{2^J}(t) \\ ||x \star \psi_{j_1}| \star \psi_{j_2}| \star \phi_{2^J}(t) \\ ||||x \star \psi_{j_1}| \star \psi_{j_2}| \star \psi_{j_3}| ... \star \psi_{j_m}| \star \phi_{2^J}(t) \end{pmatrix} \quad (6.12)$$

The removal of the complex phase by using a modulus operator reduces the variability of the coefficients in addition to making them locally invariant to translations. The scattering wavelet transform is contractive, being a cascade of wavelet operators and modulus operators, both of which are contractive. This implies that the signal energy dissipates quickly at the deeper levels of the network. Study of this property revealed that in practice, most of the energy (upto 98%) is preserved at levels 0, 1

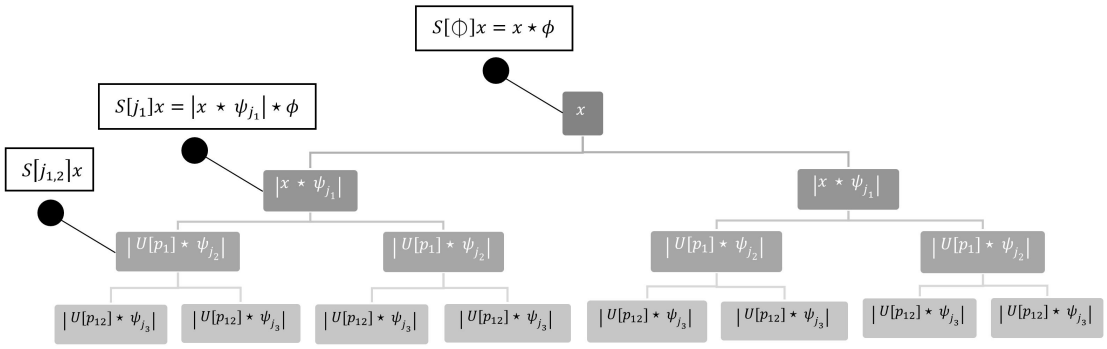

Figure 6.2: The scattering wavelet computation tree where $U[p_{qr}] = \big||x \star \psi_{j_q}| \star \psi_{j_r}\big|$. This tree has a depth (m) of 3. The scattering wavelet output from each level is shown in boxes. The signal decomposition at each node is shown in the node. (Andén and Mallat, 2012)

and 2 (Bruna and Mallat, 2011). Hence, for practical problems, limiting the network depth to 2 levels provides a rich enough description for classification purposes.

The ScWT coefficients are also Lipschitz continuous, implying that small deformations are linearized, adding to the stability of the ScWT (Bruna and Mallat, 2011). This property can also be used to create a generative classifier where the classes are learnt by identifying an approximate affine space $\boldsymbol{A}_{d,i}$ describing the class in the scattering domain (Estrach, 2012). Such a classifier is called an affine space classifier.

For a signal x, let each signal class be represented by vectors X_i. Each class is then modeled by the classifier using its scattering coefficient descriptor $S_J X_i$ to define an affine linear space computed with a PCA. The PCA diagonalizes the class-conditional empirical covariance matrices of $S_J X_i$, and identifies the d covariance eigenvectors of largest variance, denoted by $\boldsymbol{V}_{d,i}$. The dimension of the affine space (d) is adjusted so that the error between $S_J X_i$ and its projection onto $\boldsymbol{A}_{d,i}$ is minimized.

$$\boldsymbol{A}_{d,i} = E\left\{S_J X_i\right\} + \boldsymbol{V}_{d,i} \tag{6.13}$$

$$\hat{i}(x) = \underset{i<K}{argmin} \left|\left|S_J x - P_{\boldsymbol{A}_{d,i}}(S_J x)\right|\right| \tag{6.14}$$

An unclassified signal x is assigned the class with the best approximation space, given by $\hat{i}(x)$ from equation 6.14. An equivalent method of computing $\hat{i}(x)$ is by minimizing the distance between $S_J x$ and each class centroid $E\left\{S_J X_i\right\}$.

Increasing the dimension, decreases the approximation error for each class (term 2 in equation 6.14 i.e. $P_{\boldsymbol{A}_{d,i}}(S_J x)$, however not necessarily the distance between the affine spaces of each class. The classifier learns the dimension d that yields the optimal trade-off by running a cross-validation procedure on a subset of the training dataset that is not used for PCA calculations. Consequently, signal classes are represented by affine spaces of varying dimension in the scattering domain. Since the learning is performed on class specific cross-correlation matrices, such a classifier is efficient for small training sample sizes as is the case in this BCI (Estrach, 2012).

The network used for the ScWT decomposition for the BCI had a maximum depth of 2 layers with a maximum scale of 128. All BCI related processing was carried out in MATLAB, using the ScatNet toolbox (Sifre *et al.*, 2013) for ScWT related computation. Previous work with applying the ScWT on EEG data using the BBCI Competition III dataset (http://www.bbci.de/competition/iii/) found that the Gabor mother wavelet provided the best classification results when compared to other wavelet families such as the Daubechies, Morlet and Spline wavelets. Hence the mother wavelet chosen for the ScWT decomposition in this thesis was the Gabor wavelet as shown in figure 6.1.

During the training phase of the BCI, the computed scattering coefficients of each trial were fed into the affine space classifier to generate a model of the current trial class (low or high note). During the feedback section of the BCI, the generated models were used by the affine space classifier to classify the trial as either a low note trial or a high note trial. This represented the class of the note imagined by the subject and was played back via headphones.

The accuracy of predicting the correct tone was computed for each subject over the course of the experiment using segments of 10 trials each.

6.2.3 Resting State Analysis

The EEG microstate analysis and fMRI RSN analysis was conducted separately and then fused together to probe the simultaneous EEG-fMRI recordings.

EEG Microstates

Brain Vision Recorder (BVR) was used to record the resting state EEG data. This data was read into MATLAB for further processing using the EEGLAB toolbox (Delorme and Makeig, 2004). In particular, the FASTR algorithm was parallelized to speed up (approximately 3x) the process of gradient artifact and pulse artifact corrections. After artifact removal, the data was filtered using a 0.4 Hz to 40 Hz bandpass filter followed by downsampling from 5000 Hz to 256 Hz. All data was processed using a Dell XPS 15 laptop with a 4th generation Intel i7 quad core processor (2.5 GHz), 16 GB RAM, and an Nvidia GeForce 750M graphics card. This concluded the pre-processing steps in the analysis.

EEG microstates were identified as the topology of electrode voltages at peaks

of the global field potential (GFP), computed from the pre-processed data for each subject. The GFP for a n channel EEG system at time t is given by:

$$GFP(t) = \sqrt{\frac{\sum_{i=1}^{n}(v_i(t) - \bar{v}(t))^2}{n}} \tag{6.15}$$

Where $v_i(t)$ is the voltage at channel i and $\bar{v}(t)$ is the mean voltage across all channels. The local maxima in GFP are peaks in EEG field strength (Milz *et al.*, 2016). To identify all local maxima, the highest peak is first chosen (global maxima), after which the threshold for peak detection is incrementally decreased until the peak threshold equals the noise threshold. All such peaks are considered while computing the EEG microstates. The EEG microstate topologies from each peak were aggregated across all subjects and was analysed by a k-means clustering algorithm to identify primary classes of microstate topologies. Once identified, each peak was classified into one of the primary microstate classes. The sequence of these primary classes of microstates was recorded, creating a time series of microstates. This procedure is summarized in Figure 6.3.

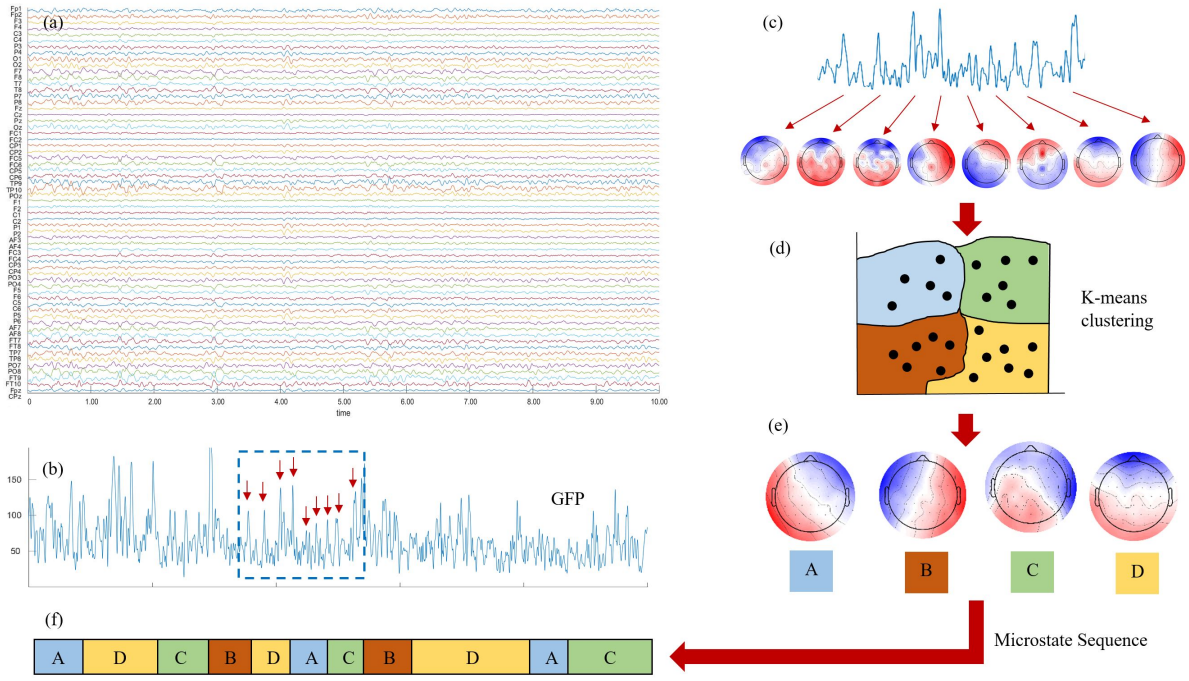

Figure 6.3: The procedure to identify microstate sequences. The EEG channel data (a) is used to compute GFP time series (shown in (b)), using equation 6.15. The peaks in the GFP are identified (red arrows) and the EEG topologies at these peaks are recorded as the microstates. This is shown in (c) where the boxed segment of the GFP trace is magnified. The identified microstates undergo k-means clustering (illustrated in (d) using 2 electrodes which are the two axes shown) to identify dominant microstate topologies (e), which is backprojected onto the microstate time series to generate the microstate sequence shown in (f).

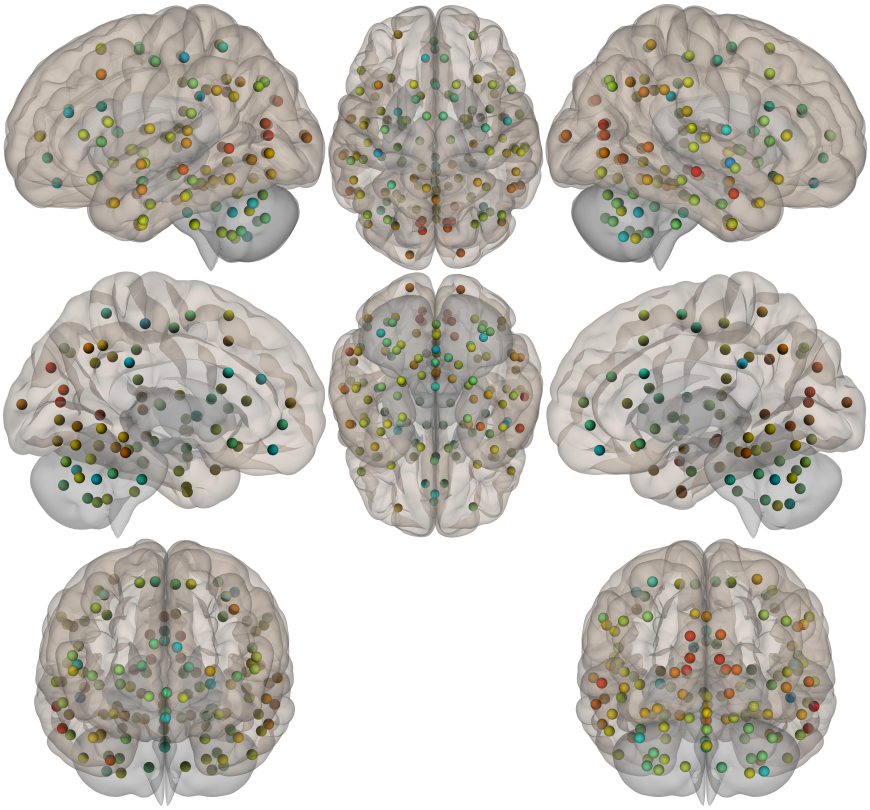

Figure 6.4: The foci of the 136 Regions of Interest (ROIs), shown using multiple views of the brain (Left, Left medial, Ant., Sup., Inf., Right, Right medial, Post.). The different colors indicate distinct functional networks in the brain. Figure generated using the CONN Toolbox (Whitfield-Gabrieli and Nieto-Castanon, 2012).

fMRI Resting State Network Analysis

The acquired BOLD data was de-noised, motion corrected, and aligned with the MNI standard space, after applying a 2mm spatial Gaussian blur. Masks for 136 major brain regions (listed in Appendix A and shown in Figure 6.4) were created and the average BOLD signal within each region was isolated for each subject. The pre-processed data was then used to compute region-to-region correlations, creating a connectivity matrix for each time point. The correlation (r) computed was using a

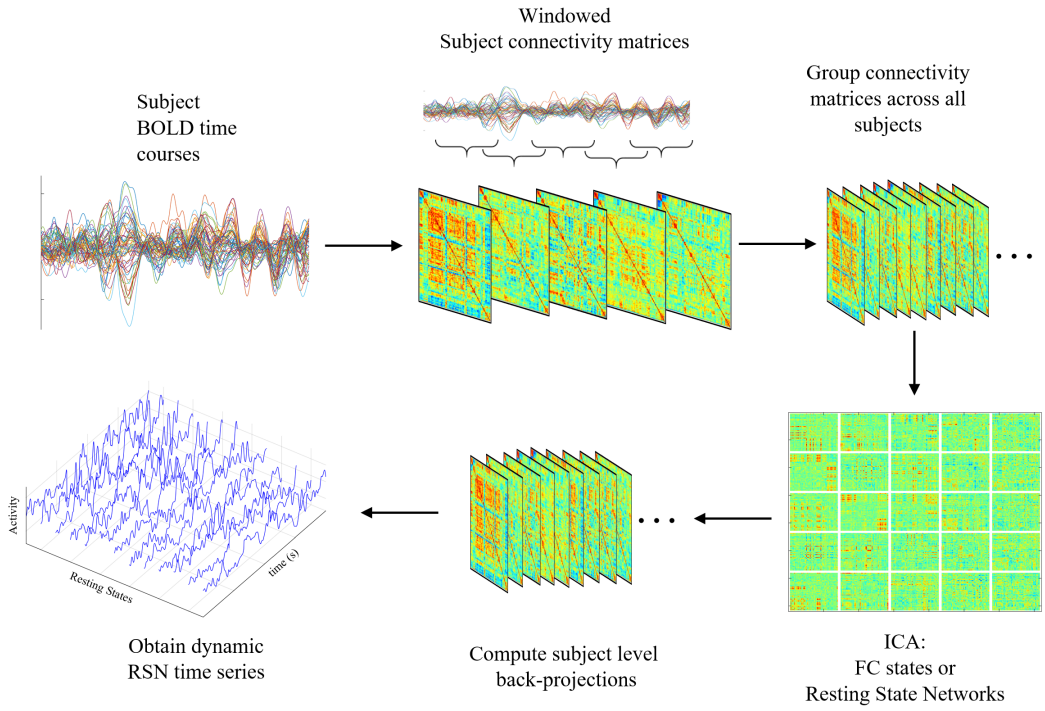

Figure 6.5: Procedure to identify the RSNs and their time courses. The RSNs are identified from an ICA decomposition of group connectivity matrices. This is back-projected onto the subjects to obtain the time courses.

linear bivariate model as follows:

$$r = \left(\sqrt{x^t \cdot x}\right) \cdot b \cdot \frac{1}{\left(\sqrt{y^t \cdot y}\right)} \tag{6.16}$$

where x and y are BOLD time series from two different regions of the brain. The computed correlation gives the level of linear similarity between the pair of BOLD time series. Mathematically, r^2 gives the percentage of BOLD signal variance in y that is explained by the BOLD signal in x. The matrix with the correlations between each ROI is termed the connectivity matrix. Global functional connectivity (FC)

was computed for all subjects and significant group level connections were identified (Bonferroni corrected $p<0.05$). The resultant connections are shown within the brain in Figure 7.4 and as a connectome wheel in Figure 7.5.

Dynamic functional connectivity (dynFC) was computed for each subject by running the correlational analysis on 100 second long windows of the BOLD time series. Independent dynFC factors were identified by using an independent component analysis (ICA) decomposition (described in detail in subsection 2.1.3) on the aggregate dynFC matrices for all subjects. A total of 25 dynFC factors were identified from this decomposition (shown in Figures 7.6 and 7.7). These factors were the empirically identified resting state networks (RSNs). The identified factors were back-projected onto individual subjects to obtain a time series for the activity of each RSN. This procedure is summarized in Figure 6.5.

Combined EEG-fMRI analysis

The time series of microstates sequences and RSNs sequences were time registered using the gradient onset markers recorded in the EEG data. The dominant RSN for each time point was identified by comparing the contribution of all RSNs and picking the one with the largest contribution at the current time point. The microstate sequence corresponding to the time segment taken for acquiring the fMRI volume for the current time point was extracted and the proportion of each microstate was computed. This was repeated for all time points and the microstate composition for each RSN was averaged over all time points corresponding to each RSN. This procedure was repeated across all subjects and a group level average was computed to determine the microstate composition of each RSN for the healthy population.

Chapter 7

Results

7.1 Brain Computer Interfacing (BCI)

The BCI's accuracy of predicting the correct tone imagined by the subject was computed over the course of the experiment using segments of 10 trials each. The resultant Accuracy vs Trial curve (shown in Figure 7.1) has a positive slope. A linear fit was applied to each subject's curve. The mean slope of the subjects' fit was $5.4 \times 10^{-3} \pm 1.3 \times 10^{-3}$ accuracy points per trial ($R^2 = 0.89$), assuming a linear model as appropriate. This average curve is shown in Figure 7.2 along with the associated error regions (in grey). From the group analysis, the standard deviation of the average accuracies was 0.0507.

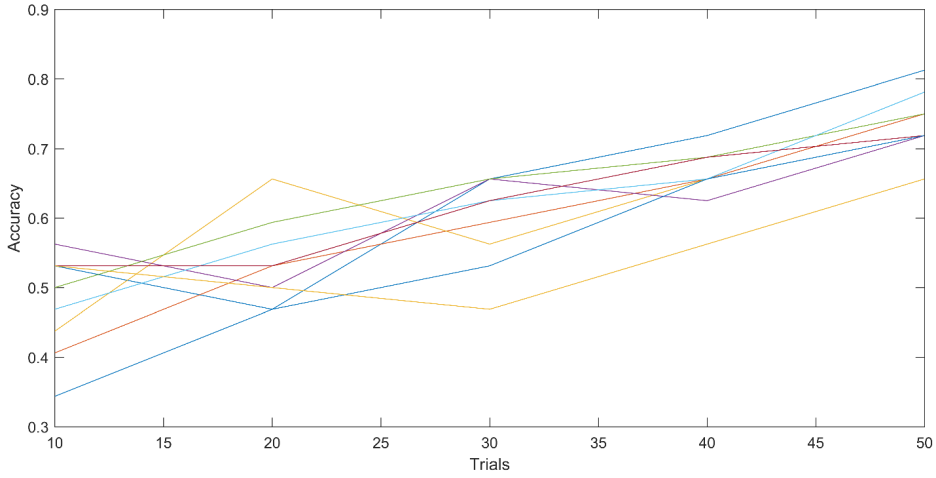

Figure 7.1: The accuracy of the BCI classifier using 10 trials over the duration of the scan. The improvement in performance is attributed to the subject's learning due to no updates to the classifier model.

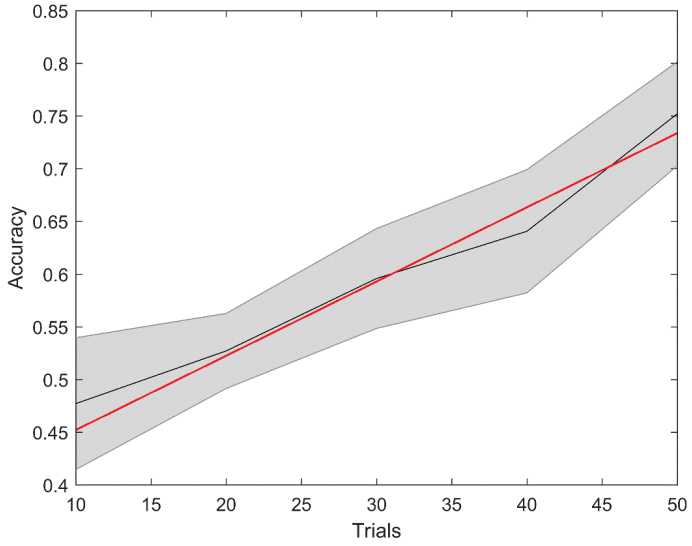

Figure 7.2: The average accuracy (of all subjects) of the BCI classifier. The linear fit with a slope of $5.4 \times 10^{-3} \pm 1.3 \times 10^{-3}$ accuracy points per trial and an $R^2 = 0.89$, is shown in red. The associated error region is shaded gray.

Power analysis was performed for a confidence interval of 95% to 99% (Z-score = 1.960 to 2.576) using equation 7.1 to verify the sufficiency of the sample size. Using this, $N(95\%) = 2.5$ and $N(99\%) = 12.4$, thereby verifying that the current sample size of 10 subjects is sufficient for a 95% confidence interval.

$$N = \frac{Z \cdot \rho \cdot (1 - \rho)}{\varepsilon} \tag{7.1}$$

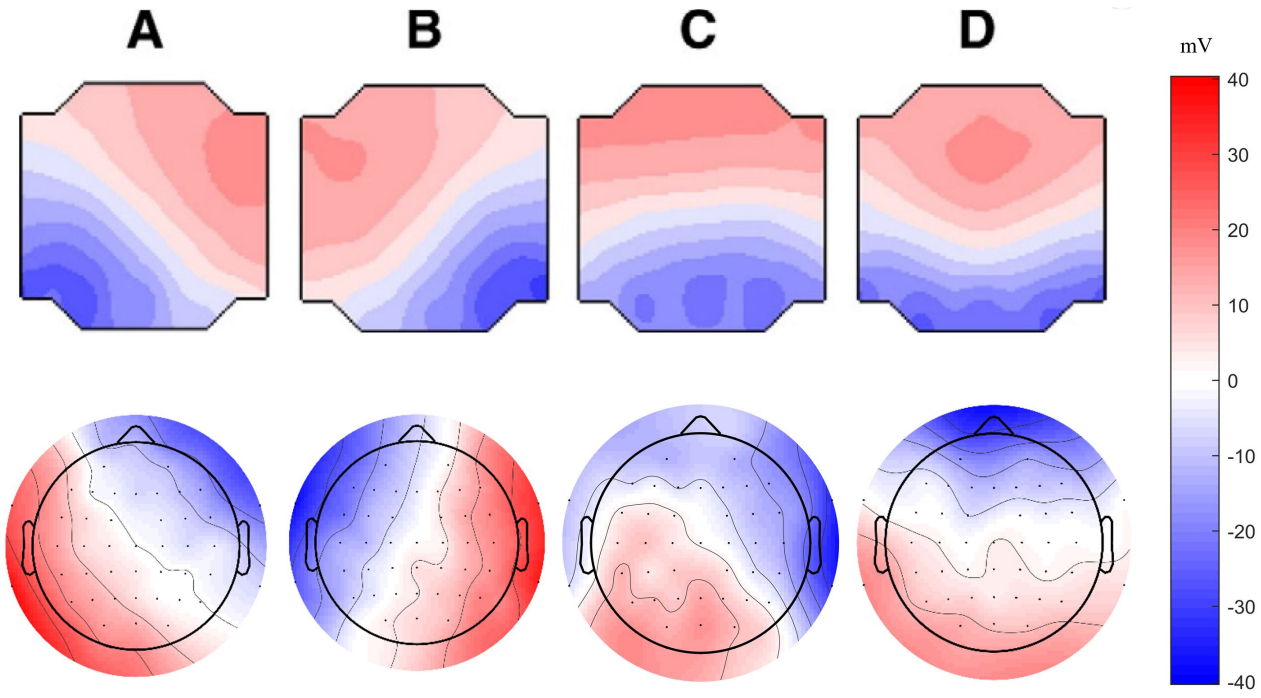

Figure 7.3: The 4 dominant Microstates as defined by (Milz *et al.*, 2015) (Top row). The 4 corresponding Microstates identified from the rsEEG data (Bottom row. In order, Left to Right).

7.2 Resting State EEG-fMRI

Redundant microstates were observed (spatial correlation > 0.75) when the number of microstate classes increased past 4. These redundant states were non-ideal as the classes no longer remained completely independent. Hence, the optimal number of classes that provided the maximal difference between the microstates was found to be 4. These four classes of microstates were responsible for 81% of the variance across all the microstates and 69% of the variance of the entire EEG session. The identified microstate topologies were found to be identical to those reported in the literature. The morphology of the different classes of Microstates is shown in Figure 7.3.

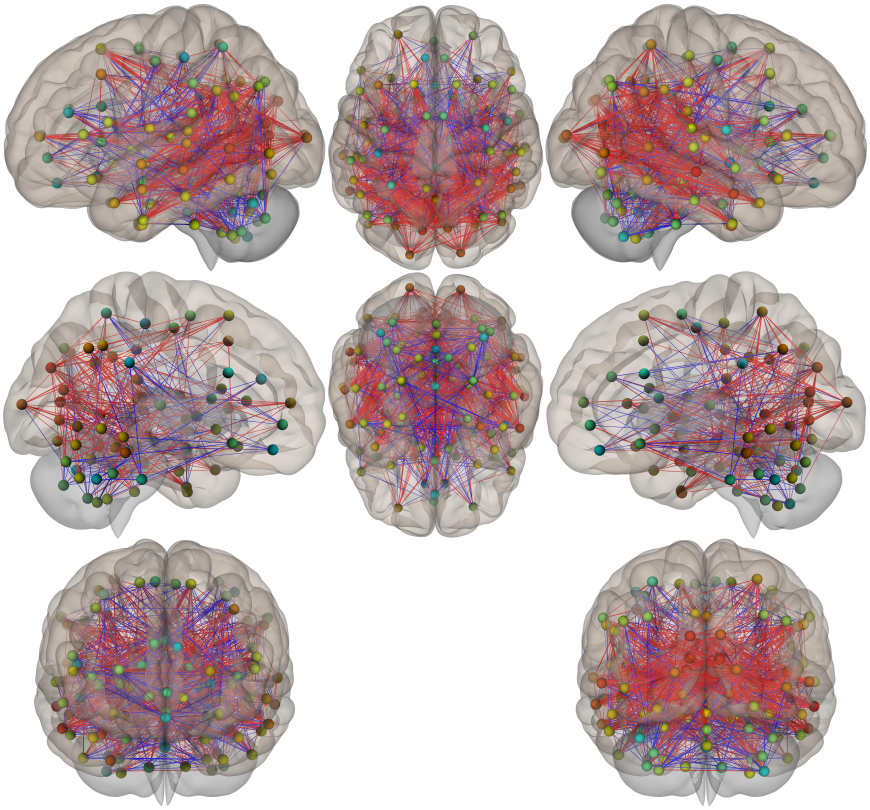

Figure 7.4: The connectivity pattern for the significant ROIs (Bonferroni corrected $p<0.05$) across all subjects. Positive correlations are shown in red and negative correlations in blue. The brain views (in order, Top to Bottom, Right to Left) are Left, Left medial, Ant., Sup., Inf., Right, Right medial and Post.

The connectivity pattern showed positively correlated connections and negatively correlated connections. Figure 7.4 graphically shows the significant connectivities between ROIs across all subjects. This data is displayed as a connectome map in Figure 7.5 for better visualization of the connectivities that exist across all subjects during rest.

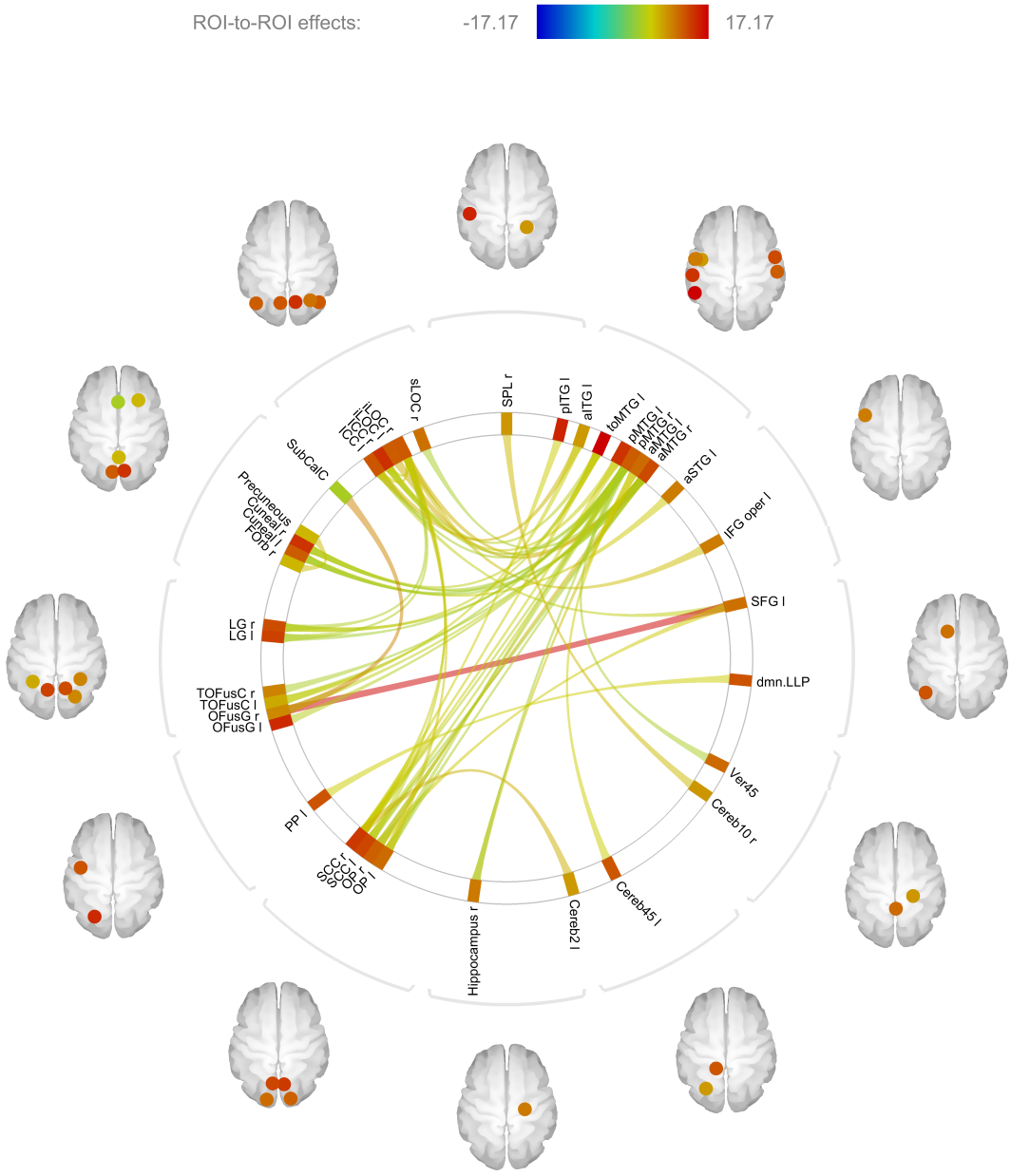

Figure 7.5: The connectome map showing the connectivity from figure 7.4 across significant ROIs (Bonferroni corrected $p<0.05$) for all subjects. Positive values represent positive correlation and negative values represent negative correlation. Figure generated using the CONN Toolbox (Whitfield-Gabrieli and Nieto-Castanon, 2012).

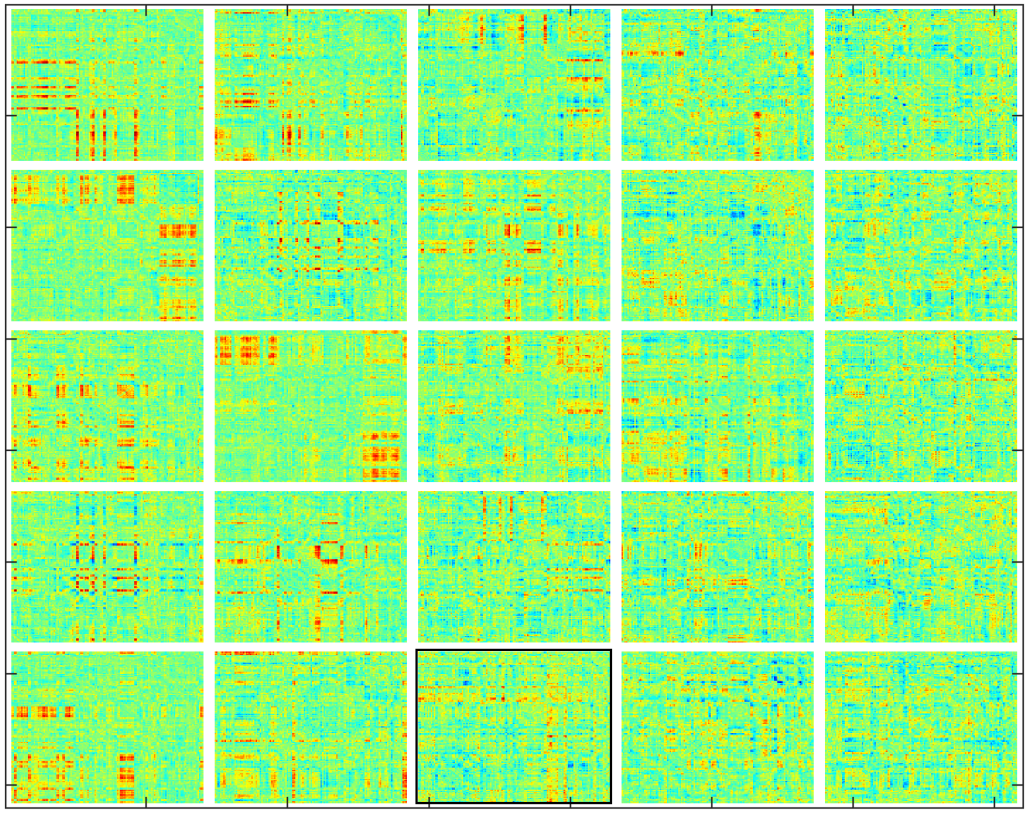

Figure 7.6: The 25 Functional Connectivity components identified across all subjects, as identified in Table 7.1 (In order, Top to Bottom, Left to Right). Component 15 (black box) is shown in detail and further discussed in Figure 7.7. Figure generated using the CONN Toolbox (Whitfield-Gabrieli and Nieto-Castanon, 2012).

The 25 independent dynamic Functional Connectivity (dynFC) maps identified from the aggregate subject data is shown in Figure 7.6. The various regions of the dynFC maps represent different regions in the brain as given in Figure 7.7, where one of the dynFC maps is segmented into the corresponding segments of the brain. Most dynFC components showed activation of a major network in the brain, as labeled in Table 7.1.

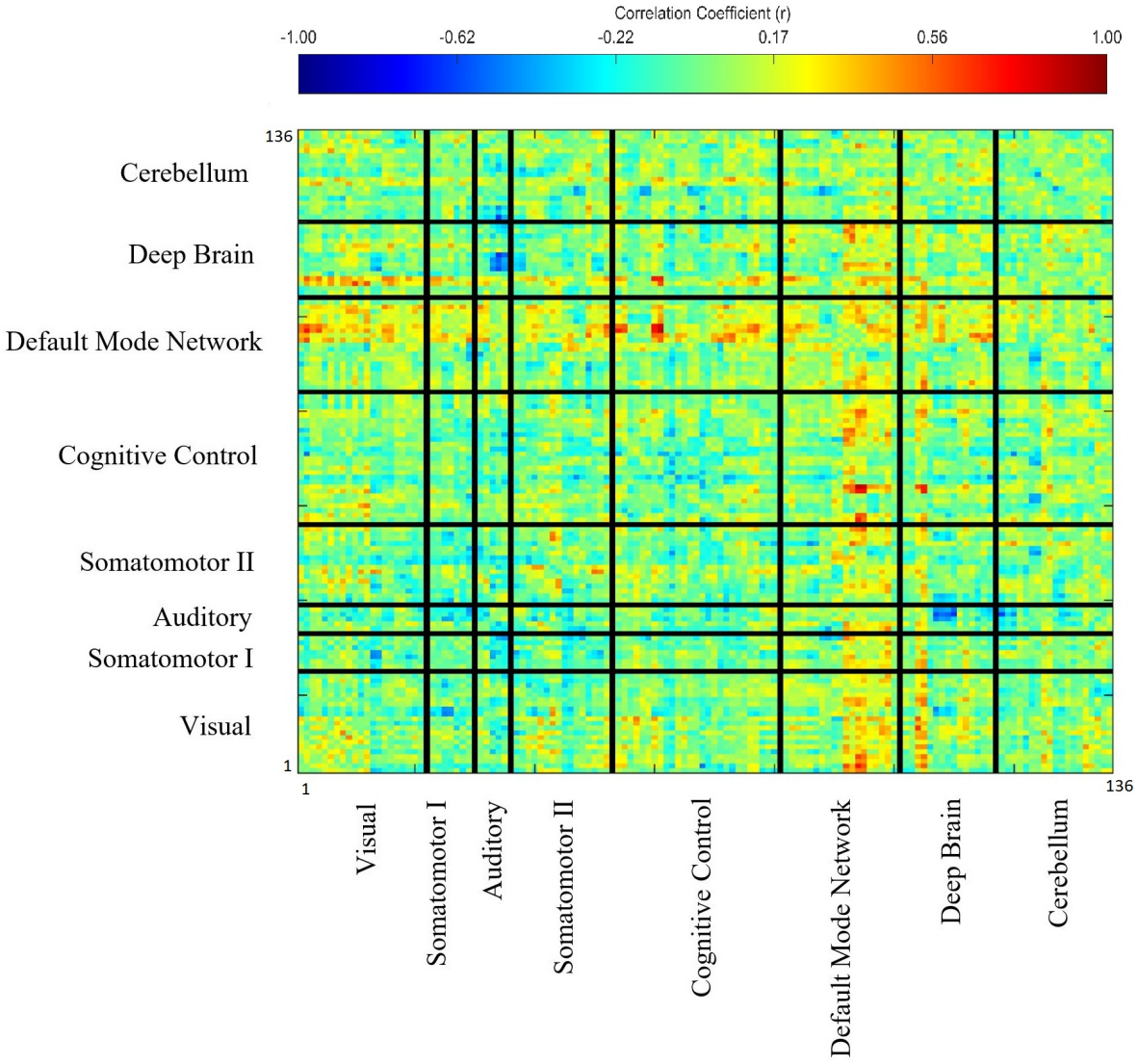

Figure 7.7: The various sections of FC map 15 along with the corresponding functional regions of the brain. The axes correspond to the 136 ROIs used for FC analysis (detailed in the appendix). Each pixel corresponds to the computed correlation coefficient (from equation 6.16) between the corresponding pairs of ROIs. Activation along the column corresponding to the region labeled indicates involvement of this network in the labeled function. For example, the given FC map is that of ICN 15, corresponding to the Default Mode Network (DMN), shown by the activation along the regions constituting the DMN

dynFC Component	Network Type/Activity	Reference
1	Visual Processing	(Seghier, 2012)
2	Dorsal Attention	(Meehan and Bressler, 2012)
3	Auditory	(Meehan and Bressler, 2012)
4	Anterior DMN	(Uddin *et al.*, 2009)
5	Visuo-spatial Attention	(Gitelman *et al.*, 1999)
6	Somatomotor	-
7	Cognitive Control	-
8	Deep Brain	-
9	Temporo-Parietal	-
10	Speech/ Language Processing	(Friederici *et al.*, 2003)
11	Fronto-Temporal	-
12	Executive Control	(Alvarez and Emory, 2006)
13	Cognitive Control	-
14	Salience	(Meehan and Bressler, 2012)
15	DMN	(Uddin *et al.*, 2009)
16	Spatial Attention	(Gitelman *et al.*, 1999)
17	Somatomotor	-
18	Dorsal Attention	(Meehan and Bressler, 2012)
19	Attention	(Zhang *et al.*, 2016)
20	Miscellaneous	-
21	Miscellaneous	-
22	Miscellaneous	-
23	Miscellaneous	-
24	Miscellaneous	-
25	Miscellaneous	-

Table 7.1: The various types of RSNs identified by dynFC analysis (- are miscellaneous networks)

7.3 Comparison of the EEG Microstates and the Resting State Networks

Each BOLD timepoint showed a dominant resting state network active during the time duration of the volume acquisition. Each dominant RSN remained dominant for approximately 3-4 consecutive TRs. During this time, multiple microstate transitions were observed and their composition was characterized. Table 7.2 shows the microstate composition corresponding to the 25 resting state networks, during the BOLD timepoints in which they were dominant.

RSN Number	Microstate A	Microstate B	Microstate C	Microstate D
1	0.447 ± 0.12	0.188 ± 0.02	0.094 ± 0.01	0.272 ± 0.08
2	0.431 ± 0.43	0.145 ± 0.07	0.157 ± 0.11	0.267 ± 0.13
3	0.475 ± 0.12	0.142 ± 0.04	0.107 ± 0.05	0.276 ± 0.13
4	0.431 ± 0.19	0.230 ± 0.06	0.080 ± 0.05	0.259 ± 0.12
5	0.495 ± 0.17	0.150 ± 0.05	0.051 ± 0.03	0.304 ± 0.12
6	0.327 ± 0.10	0.549 ± 0.17	0.000 ± 0.00	0.124 ± 0.02
7	0.043 ± 0.03	0.428 ± 0.15	0.138 ± 0.05	0.390 ± 0.13
8	0.181 ± 0.12	0.447 ± 0.28	0.070 ± 0.11	0.301 ± 0.27
9	0.467 ± 0.14	0.183 ± 0.05	0.071 ± 0.03	0.279 ± 0.09
10	0.039 ± 0.02	0.371 ± 0.09	0.148 ± 0.13	0.443 ± 0.07
11	0.433 ± 0.23	0.173 ± 0.06	0.135 ± 0.19	0.259 ± 0.13
12	0.462 ± 0.13	0.177 ± 0.09	0.089 ± 0.05	0.270 ± 0.08
13	0.044 ± 0.03	0.442 ± 0.16	0.137 ± 0.08	0.377 ± 0.09
14	0.458 ± 0.33	0.192 ± 0.06	0.069 ± 0.06	0.280 ± 0.14
15	0.474 ± 0.22	0.446 ± 0.02	0.007 ± 0.02	0.038 ± 0.10
16	0.048 ± 0.03	0.436 ± 0.12	0.188 ± 0.08	0.329 ± 0.08
17	0.062 ± 0.01	0.278 ± 0.11	0.213 ± 0.10	0.448 ± 0.15
18	0.031 ± 0.02	0.479 ± 0.25	0.120 ± 0.06	0.370 ± 0.12
19	0.044 ± 0.04	0.436 ± 0.18	0.107 ± 0.06	0.413 ± 0.12
20	0.454 ± 0.15	0.189 ± 0.05	0.084 ± 0.05	0.273 ± 0.11
21	0.482 ± 0.18	0.150 ± 0.05	0.085 ± 0.03	0.284 ± 0.12
22	0.222 ± 0.67	0.333 ± 1.00	0.222 ± 0.67	0.222 ± 0.67
23	0.430 ± 0.27	0.384 ± 0.12	0.030 ± 0.05	0.033 ± 0.06
24	0.313 ± 0.07	0.526 ± 0.16	0.000 ± 0.00	0.161 ± 0.06
25	0.112 ± 0.06	0.008 ± 0.02	0.198 ± 0.07	0.682 ± 0.27

Table 7.2: The mean microstate percentage composition for of the 25 resting state networks (RSN). The values shown are means and standard deviations computed across all healthy subjects.

Chapter 8

Discussion

BCIs have been previously used for the control of neuroprosthesis (Bhagat *et al.*, 2016), and for directed rehabilitation of neuropathologies such as ALS (McCane *et al.*, 2014), Locked-in Syndrome (Oken *et al.*, 2013), and other motor impairments (Halder *et al.*, 2016), (Daly and Wolpaw, 2008). However, this framework is the first known attempt at developing a BCI based system as a metric for characterizing the cognitive integrity of a subject, rather than an assistive device or a tool for rehabilitation (Shih *et al.*, 2012). This could potentially allow for diagnosis of neuropathologies that affect cognitive functionality. As with any diagnostic tool, its operation needs to be characterized on a healthy population, so that it may then be tested on a diseased population.

8.1 Brain Computer Interfacing

For the healthy population studied, the BCI performance was found to linearly increase with time (Figure 7.1). Since there was no update to the models of the two

classes once the BCI began, this improvement in BCI performance can be directly attributed to learning on the subject's part. Such a BCI design allows for the deconvolution of the human learning process from the machine learning process by temporally splitting the two into separate blocks. This is in contrast to traditional BCI designs which allow the machine and human to continually co-adapt throughout the experiment, making it hard to isolate the human contribution in BCI performance improvement (McFarland and Wolpaw, 2011).

Identifying the factors that influence a subject's BCI performance is essential to understand the implications of such observed BCI performance profiles. Despite considerable research in other aspects of BCI development, very few studies have probed subject level factors that modulate BCI performance (Nijboer *et al.*, 2010). Halder *et al.* (2011) suggested the involvement of attentional and self-regulatory brain regions such as the dorsolateral prefrontal cortex in execution of the BCI task. This is supported by Hammer *et al.* (2012) and Hammer *et al.* (2014), who showed that a subject's "ability to concentrate" accounted for a considerable amount of BCI performance variance (19%). In addition to attentional control, other factors, such as the level of working memory and executive function, have also been implicated in the modulation of BCI performance (Sprague *et al.*, 2015). Tasks external to the BCI that are known to improve working memory (such as n-back tasks (Morrison and Chein, 2011)), when performed in conjunction with the BCI, improved BCI performance (Sprague *et al.*, 2015). The switching of thought processes between the different classes of brain states during BCI is thought to recruit the attentional control and executive functionality networks in the brain (Sprague *et al.*, 2015), thereby suggesting their effect on the BCI performance, irrespective of the BCI task specifics.

This effect persists even in subjects with disabilites such as amyotrophic lateral sclerosis (Riccio *et al.*, 2013). In light of the link between a subject's functional level of such cognitive factors and their BCI performance profile, the latter may be used as a metric of the functional level of the factors discussed. Given that numerous brain disorders such as depression, anxiety (Akerlund *et al.*, 2013) and concussion (Keightley *et al.*, 2014) negatively affect such factors, BCIs could potentially be used as a tool to detect them. Although BCI performance metrics may not be able encapsulate all the intricacies of attention, working memory and executive function, it could serve as a first level quantitative estimate of their functionality. Hence, an appropriate metric needs to be derived from the BCI performance data to accomplish this goal. The slope of the Accuracy vs Trial curve (Figures 7.1, 7.2) is one such metric. Absolute accuracy values have a higher variance (compared to the slope), potentially due to a host of other factors such as fatigue, and individual variances in familiarity with the BCI task (Nijboer *et al.*, 2010). However the improvement in accuracy over time is highly dependent on the learning process in the subject, which are known to be modulated by the factors discussed above (Hammer *et al.*, 2012).

Three major learning theories have been used to explain the pattern of learning observed in BCIs (Hammer *et al.*, 2012). The first is based on operant learning (Skinner, 1945), second on motor learning (Lang and Twentyman, 1976) and the third is based on the dual process theory (Lacroix and Gowen, 1981). Being a combination of the other two, the dual process theory is the most general and hence pliable to most BCIs. This theory suggests that learning takes place using a combination of feed-forward and feed-backward information flow, starting with an estimated strategy and changing it if and when it becomes and ineffective strategy. This ensures that

eventually, the optimal strategy persists and performance is improved. Hence the slope, which represents the learning undergone by the subject, is a more appropriate metric for characterizing the subjects level of cognitive functionality, as the associated learning procedures are modulated by the cognitive factors discussed above (Engle *et al.*, 2004).

One of the major concerns with BCIs built for traditional assistive tasks is the non-generalizability of the learned model. This often results in the BCI performance varying vastly between subjects (Zhang *et al.*, 2016). Such differences in performance is termed the "BCI inefficiency" and is thought to stem from either psychological factors such as mood, mastery confidence, and motivation, or cognitive factors such as attention, working memory and executive control (Hammer *et al.*, 2012), (Nijboer *et al.*, 2010). Some subjects may function at a higher cognitive level than others, allowing them to excel at the BCI task. Exploiting this source of variance in BCI accuracy results, to identify deviations from normal cognitive function, could be a future application of this protocol, as discussed earlier. The results from a large group of healthy controls can be used as the healthy standard when analyzing a potentially ill subjects data.

Evaluation of a subjects' cognitive capacity for detection of disorders is currently done using neuropsychological testing. They can be used to evaluate a subject's attentional capacity (TOVA (Greenberg and Waldmant, 1993)), working memory (WCST (Miyake *et al.*, 2000)), and executive function (Alvarez and Emory, 2006). However, these have been shown to have low positive predictive value (PPV) for subtle brain disorders such as mTBIs (Binder *et al.*, 1997). Furthermore, other tasks that may involve learning and could potentially predict these factors, require

multiple training sessions to see a performance improvement (Bugos *et al.*, 2007). It would therefore be extremely time consuming to use such a task to estimate a subject's learning characteristics. BCI based neurofeedback training however, shows performance improvements within a single session (Blankertz *et al.*, 2008), allowing it to characterize the subject's functional capacity in a short period of time (One BCI session - 30 to 45 mins).

Given that the BCI learns a model of the user's brain activity, it could also be used to track the progress of the subject over time by comparing the brain model at subsequent sessions of the BCI with that of the first session, making BCIs an ideal tool for diagnosing potential neuropathologies and tracking their resolution, through the course of recovery.

8.2 The Scattering Wavelet Transform

One of the major sources of variance in the EEG signal (and consequently in BCI performance), is its non-stationarity. The non-stationarity of EEG makes it hard for regular features to adapt to an ever changing input signal. Hence adding invariance to non-stationarities in the signal improves the BCI performance (Samek *et al.*, 2012). This was attempted in the current study by using a novel variant of the wavelet transform - the Scattering Wavelet Transform (ScWT) as the input feature to the classifier.

The ScWT has been previously used for successfully classifying textures (Estrach, 2012), audio signals (Andén and Mallat, 2011), lingual accents (Lerch, 2015), faces for face verification (Jain and Swaminathan, 2014) and in characterizing intrapartum fetal heart rate variability (Chudacek *et al.*, 2014). However, it has not been applied to

any other biological signal, including EEG. Given the similarity between audio signal processing and EEG signal processing, such an extension is not a difficult task. This thesis marks the first such application, demonstrating that ScWT can be successfully used for obtaining above chance classification accuracy on EEG signals.

The ScWT improves upon the non-stationary properties of regular WTs by adding translation invariance to the computed coefficients. Such an invariance allows for a more robust BCI performance due to decreased variability in the model of the BCI classes.

Another feature of the ScWT is the ease with which additional invariance can be added to the features. The ScWT coeffients can be made invariant to any set of functions that can be modeled as a compact Lie group (G). This is accomplished by replacing the cascaded wavelet transforms on $\mathbf{L}^2(\mathbf{R}^2)$ by wavelet transforms on $\mathbf{L}^2(G)$ (Bruna and Mallat, 2011). One example of such a group is $G = SO(2)$, which is the group of rotations in $\mathbb{R}^2$. Adding invariance to this group changes equation 6.11 to the following

$$\tilde{S}_J[\tilde{p}]x(t) = \int_G U[\tilde{p}]\ x(g)\ \tilde{\phi}_{2^J}(g^{-1}t) \cdot dg \tag{8.1}$$

Where $\tilde{\phi}_{2^J}(x(t))$ are the wavelets on the group G. In the case of the rotation group, these are the rotated versions of the mother wavelet (Mallat, 2012). This allows for the flexibility of making applications that use ScWT more robust to certain types of signal deformations. More research into such deformations is needed to be able to model them as Lie groups and apply the above mentioned modification to make ScWTs invariant to them.

An added benefit of the ScWT structure is its the convolutional network architecture which allows for quick computation of the coefficients. These coefficients are

representative of the time and frequency characteristics of the EEG signal across multiple scales. Thus, the ScWt are robust and information rich features, making them ideal for use in a BCI.

8.3 Microstates

Microstates are quasi-stable classes of EEG topology that switch between each other over time. There is no pre-determined number of classes into which the microstates can be divided. Previous research suggests that 4 classes of microstates provide the optimal number of classes to explain approximately 70% of the variance (Khanna *et al.*, 2014). These microstates were found to be responsible for verbal, visual, subjective interoceptive- autonomic processing, and attention reorientation tasks (Milz *et al.*, 2015), and are shown in Figure 7.3. However, other studies have found additional microstates responsible for finer tasks such as sensorimotor activity by decomposing the microstates into a larger number of classes (Yuan *et al.*, 2012). Consequently, the number of microstate classes used for decomposition was varied from 2 to 10 microstates in order to study all possible microstate classes identifiable from the data. Also, staying consistent with current literature, switching of polarities in the microstate topology was considered the same microstate (Milz *et al.*, 2016).

Despite having decomposed the resting state EEG into higher number of microstates, 4 microstates emerge as dominant contributors to the functional networks, consistent with previous literature (Milz *et al.*, 2016).

The detection of microstates was found to be extremely sensitive to faulty electrodes. A single faulty electrode suppressed the detection of all other microstates and produced a topology similar to that shown in Figure 8.1. This is due to protocol

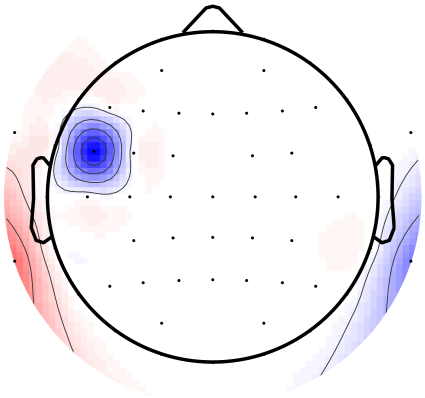

Figure 8.1: The identified microstate 4 for a scanning session with a faulty electrode (FC5). Regular electrode topologies are replaced by a halo around the faulty electrode.

followed for identifying the microstates, which only depends on the topologies at the GFP peaks for identification of the microstates. For the purposes of this study, such scans (2 for this study) were omitted from the analysis. However, for future implementations, adding more features to identify the microstates will make this process robust and insensitive to such system wide faults. One such feature that has been explored is the localization of the sources in each EEG epoch using source localization packages like LORETA (Musso *et al.*, 2010).

8.4 EEG-fMRI Results

The processing of information by the brain is thought to take place by the preliminary processing of data within the relevant primary cortices, followed by transfer of processed information to secondary cortices that consolidate information from multiple sources (visual, tactile, olfactory, etc.) (Meehan and Bressler, 2012). Consequently, these secondary regions are expected to be heavily connected with other networks in the brain.

One such secondary region is the occipito-parietal region which is implicated in consolidation of visual and language information (Tzvi *et al.*, 2016), (Bettencourt and Xu, 2016). From figure 7.4, it can be seen that this region is heavily connected with other regions of the brain, implying there is a large amount of information being processed by this region, even under zero cognitive load.

Another such pathway of information assimilation is the fronto-occipital connections which are responsible for processing of objects (Sehatpour *et al.*, 2010). A high connectivity value observed between the superior frontal gyrus (SFG) and the occipital fusiform gyrus (OFusG) in figure 7.5 is representative of this pathway. The effect sizes (connectivity value) portrayed in figure 7.5 represents the percentage of the BOLD signal affected at the target(SFG) for a 1 percent signal change at the source(OFusG).

Such patterns of resting state activity was also observed in the dynamic functional connectivity and EEG microstate analysis. Each RSN identified from the BOLD signal involved the activation of multiple microstates within itself. However, The RSN networks that show a robust proportion of a particular microstate/s, were generally

found to be responsible for functions that have been associated with that particular microstate/s. For example, in Table 7.2, RSN 2 consisted of 27% microstate D (The variance of microstate A is too high to be considered robust), which is associated with attention reorientation (Milz *et al.*, 2015). Consistent with this finding, RSN 2 was identified as a dorsal attention network in Table 7.1. This demonstrated functional consistency in the identified RSN and the underlying microstate composition. This finding is in line with the concept that EEG microstates are "atoms of thought" (Lehmann, 1990) and are present in each thought process, including the thought process that produced the dominant RSN at each time point. Microstates can thus be used to gauge the dynamic activity of certain resting state networks.

Microstates have been reported to have a high test-retest reliability (Cronbach's $\alpha > 0.9$) and have hence been recommended as a potential biomarker for the health of the brain's cognitive networks (Khanna *et al.*, 2014). Therefore, a microstate based protocol, in conjunction with a BCI, to characterize the state of the cognitive networks and cognition respectively, forms a comprehensive testing tool that could potentially be used to diagnose and track neuropathologies.

Chapter 9

Conclusions and Future Directions

The current study showed the possibility of using a BCI based framework for evaluating the integrity of cognitive functionality. EEG Microstates were also shown to be potentially useful in characterizing the normative resting state networks traditionally probed using fMRI. This demonstrates the potential use of using EEG to probe such questions regarding functional networks, thereby increasing the accessibility of such analyses for research and clinical applications. Future work can try to characterize this predictive potential, by training a neural network to predict the resting state activity using EEG microstates acquired in an EEG alone configuration (as opposed to simultaneous EEG-fMRI).

This opens up the possibility of using this framework as a clinical diagnostic tool to diagnose neuropathologies, given the ease with which EEG testing can be performed in a clinical setting. One such neuropathology is concussion or mild traumatic brain injury (mTBI). mTBI is a diffuse brain injury caused by an abrupt acceleration and deceleration of the head that lead to shear stresses on the brain tissue, causing damage on a microscopic level (Macfarlane and Glenn, 2015). Such an injury causes a cascade

of neurochemical and electrical changes in the brain tissue (Macfarlane and Glenn, 2015), causing cognitive deficits and leaving the brain vulnerable to a second impact which can be fatal (Byard and Vink, 2009). Return-to-Play policies are drawn for sport mTBIs in order to prevent such second injuries.

Current guidelines to detect and classify mTBIs rely heavily on GCS score and self-reported measures such as the PCSS scores. GCS score is a poor metric for diagnosis due to it's poor Inter-rater reliability. Significant metabolic changes can occur despite a normal GCS score, and metabolic changes might prevail even with improving clinical symptoms (Macfarlane and Glenn, 2015).

The diffuse and microscopic nature of mTBIs render them invisible to conventional imaging modalities such as CT and anatomical MRI (Bigler and Maxwell, 2012). As a result of this, most tests used to diagnose and track mTBIs rely on neuropsychological testing, which has a poor Positive Predictive Value (PPV) of <50% (Binder *et al.*, 1997). Other methods have found mTBI linked differences as well, however, they are far from clinical use. EEG studies have found a decrease in mean alpha frequency, increase in theta activity, decrease in alpha and beta power between anterior and posterior regions, and increased coherence between frontal and temporal regions in subjects with mTBIs (Mayer and Bellgowan, 2014). EEG microstates show modified topology and longer dwell times in mTBI subjects (Corradini and Persinger, 2014). FMRI revealed significant differences of the BOLD signal in concussed individuals while performing working memory, attention, sensory-motor, auditory orientation and attention inhibition tasks (McAllister *et al.*, 2006). mTBI subjects have decreased connectivity in the Default Mode Network (DMN), and hyper-activity in the frontoparietal task related network (TRN) (Mayer and Bellgowan, 2014).

Despite seeing such changes in EEG and fMRI, their application in the clinical management of mTBIs has been limited partly due to the amount of variance observed (Gaetz and Bernstein, 2001) and the cost associated with acquiring such data (fMRI). The protocol developed in this study could be a more practical diagnostic tool that can assess the patients' cognitive integrity and the state of their functional networks, and compare them to the normative group characterized in this study.

The current protocol can also be generalized to other neuropathologies such as post-traumatic stress disorder (PTSD) which is known to affect the cognitive factors discussed in section 8.1 (Astafiev *et al.*, 2016).

Appendix A

rsfMRI Regions of Interest (ROIs)

The 136 ROIs used for the resting state fMRI analysis are given in the table below, along with the MNI coordinates of their foci.

ROI Number	ROI Abbreviation	ROI Name	MNI Coordinates (x,y,z) in mm
1	Cuneal r	Cuneal Cortex Right	(9,-79,28)
2	Cuneal l	Cuneal Cortex Left	(-8,-80,27)
3	SCC r	Supracalcarine Cortex Right	(8,-74,14)
4	SCC l	Supracalcarine Cortex Left	(-8,-73,15)
5	ICC r	Intracalcarine Cortex Right	(12,-74,8)
6	ICC l	Intracalcarine Cortex Left	(-10,-75,8)

ROI Number	ROI Abbreviation	ROI Name	MNI Coordinates (x,y,z) in mm
7	LG r	Lingual Gyrus Right	(14,-63,-5)
8	LG l	Lingual Gyrus Left	(-12,-66,-5)
9	iLOC r	Lateral Occipital Cortex (inferior division) Right	(46,-74,-2)
10	OFusG r	Occipital Fusiform Gyrus Right	(27,-75,-12)
11	OFusG l	Occipital Fusiform Gyrus Left	(-27,-77,-14)
12	iLOC l	Lateral Occipital Cortex (inferior division) Left	(-45,-76,-2)
13	TOFusC r	Temporal Occipital Fusiform Cortex Right	(35,-50,-17)
14	TOFusC l	Temporal Occipital Fusiform Cortex Left	(-33,-54,-16)
15	OP r	Occipital Pole Right	(18,-95,8)
16	OP l	Occipital Pole Left	(-17,-97,7)
17	toMTG r	Middle Temporal Gyrus (temporo-occipital) Right	(58,-49,2)

ROI Number	ROI Abbreviation	ROI Name	MNI Coordinates (x,y,z) in mm
18	toITG r	Inferior Temporal Gyrus (temporo-occipital) Right	(54,-50,-17)
19	pTFusC r	Temporal Fusiform Cortex (posterior division) Right	(36,-24,-28)
20	pTFusC l	Temporal Fusiform Cortex (posterior division) Left	(-36,-30,-25)
21	sLOC r	Lateral Occipital Cortex (superior division) Right	(33,-71,39)
22	sLOC l	Lateral Occipital Cortex (superior division) Left	(-32,-73,38)
23	IC r	Insular Cortex Right	(37,3,-0)
24	IC l	Insular Cortex Left	(-36,1,0)
25	SMA r	Juxtapositional Lobule Cortex (Supp. Motor Cortex) Right	(6,-3,58)

ROI Number	ROI Abbreviation	ROI Name	MNI Coordinates (x,y,z) in mm
26	SMA l	Juxtapositional Lobule Cortex (Supp. Motor Cortex) Left	(-5,-3,56)
27	CO l	Central Opercular Cortex Left	(-48,-9,12)
28	PO l	Parietal Operculum Cortex Left	(-48,-32,20)
29	CO r	Central Opercular Cortex Right	(49,-6,11)
30	PO r	Parietal Operculum Cortex Right	(49,-28,22)
31	PP r	Planum Polare Right	(55,-25,12)
32	HG r	Heschls Gyrus Right	(46,-17,7)
33	PT r	Planum Temporale Right	(55,-25,12)
34	PP l	Planum Polare Left	(-47,-6,-7)
35	HG l	Heschls Gyrus Left	(-45,-20,7)
36	PT l	Planum Temporale Left	(-53,-30,11)
37	AC	Cingulate Gyrus (anterior division)	(1,18,24)

ROI Number	ROI Abbreviation	ROI Name	MNI Coordinates (x,y,z) in mm
38	PreCG r	Precentral Gyrus Right	(35,-11,50)
39	PostCG r	Post Central Gyrus Right	(38,-26,53)
40	PreCG l	Precentral Gyrus Left	(-34,-12,49)
41	PostCG l	Post Central Gyrus Left	(-38,-28,52)
42	IFG oper r	Inferior Frontal Gyrus (pars opercularis) Right	(52,15,16)
43	pSMG r	Supramarginal Gyrus (posterior division) Right	(55,-40,34)
44	FO r	Frontal Operculum Cortex Right	(41,19,5)
45	FO l	Frontal Operculum Cortex Left	(-40,18,5)
46	SPL r	Superior Parietal Lobule Right	(29,-48,59)
47	SPL l	Superior Parietal Lobule Left	(-29,-49,57)

ROI Number	ROI Abbreviation	ROI Name	MNI Coordinates (x,y,z) in mm
48	aSMG r	Supramarginal Gyrus (anterior division) Right	(58,-27,38)
49	aSMG l	Supramarginal Gyrus (anterior division) Left	(-57,-33,37)
50	Cereb6 l	Cerebellum 6 Left	(-23,-58,-24)
51	Cereb6 r	Cerebellum 6 Right	(24,-58,-25)
52	Cereb8 l	Cerebellum 8 Left	(-26,-55,-48)
53	Cereb8 r	Cerebellum 8 Right	(25,-56,-49)
54	FP r	Frontal Pole Right	(26,52,8)
55	SFG r	Superior Frontal Gyrus Right	(15,18,57)
56	MidFG r	Middle Frontal Gyrus Right	(39,19,43)
57	AG r	Angular Gyrus Right	(52,-52,32)
58	IFG tri r	Inferior Frontal Gyrus (pars triangularis) Right	(52,28,8)
59	FOrb r	Frontal Orbital Cortex Right	(29,23,-16)

ROI Number	ROI Abbreviation	ROI Name	MNI Coordinates (x,y,z) in mm
60	aITG r	Inferior Temporal Gyrus (anterior division) Right	(46,-2,-41)
61	pITG r	Inferior Temporal Gyrus (posterior division) Right	(53,-23,-28)
62	FP l	Frontal Pole Left	(-25,53,8)
63	SFG l	Superior Frontal Gyrus Left	(-14,19,56)
64	AG l	Angular Gyrus Left	(-50,-56,30)
65	MidFG l	Middle Frontal Gyrus Left	(-38,18,42)
66	IFG tri l	Inferior Frontal Gyrus (pars triangularis) Left	(-50,28,9)
67	aITG l	Inferior Temporal Gyrus (anterior division) Left	(-48,-5,-39)
68	FOrb l	Frontal Orbital Cortex Left	(-30,24,-17)
69	IFG oper l	Inferior Frontal Gyrus (pars opercularis) Left	(-51,15,15)

ROI Number	ROI Abbreviation	ROI Name	MNI Coordinates (x,y,z) in mm
70	pSMG l	Supramarginal Gyrus (posterior division) Left	(-55,-46,33)
71	toMTG l	Middle Temporal Gyrus (temporo-occipital) Left	(-58,-53,1)
72	pITG l	Inferior Temporal Gyrus (posterior division) Left	(-53,-28,-26)
73	toITG l	Inferior Temporal Gyrus (temporo-occipital) Left	(-52,-53,-17)
74	TP r	Temporal Pole Right	(41,13,-30)
75	TP l	Temporal Pole Left	(-40,11,-30)
76	aSTG r	Superior Temporal Gyrus (anterior division) Right	(58,-1,-10)
77	pSTG r	Superior Temporal Gyrus (posterior division) Right	(61,-24,2)

ROI Number	ROI Abbreviation	ROI Name	MNI Coordinates (x,y,z) in mm
78	aSTG l	Superior Temporal Gyrus (anterior division) Left	(-56,-4,-8)
79	pSTG l	Superior Temporal Gyrus (posterior division) Left	(-62,-29,4)
80	aTFusC r	Temporal Fusiform Cortex (anterior division) Right	(31,-3,-42)
81	aTFusC l	Temporal Fusiform Cortex (anterior division) Left	(-32,-4,-42)
82	Amygdala r	Amygdala Right	(23,-4,-18)
83	Amygdala l	Amygdala Left	(-23,-5,-18)
84	PaCiG r	Paracingulate Gyrus Right	(7,37,23)
85	PaCiG l	Paracingulate Gyrus Left	(-6,37,21)
86	PC	Cingulate Gyrus (posterior division)	(1,-37,30)
87	Precuneous	Precuneous Cortex	(1,-59,38)
88	Brain-Stem	Brain-Stem	(0,-30,-35)

ROI Number	ROI Abbreviation	ROI Name	MNI Coordinates (x,y,z) in mm
89	Cereb45 l	Cerebellum 4-5 Left	(-14,-44,-17)
90	Cereb9 l	Cerebellum 9 Left	(-11,-49,-46)
91	Cereb9 r	Cerebellum 9 Right	(9,-49,-46)
92	aMTG r	Middle Temporal Gyrus (anterior division) Right	(58,-2,-25)
93	pMTG r	Middle Temporal Gyrus (posterior division) Right	(61,-23,-12)
94	Dmn.RLP	Default Mode Network (Right Lateral Parietal Cortex)	(46,-70,36)
95	aMTG l	Middle Temporal Gyrus (anterior division) Left	(-57,-4,-22)
96	pMTG l	Middle Temporal Gyrus (posterior division) Left	(-61,-27,-11)
97	Dmn.PCC	Default Mode Network (Posterior Cingulate Cortex)	(-6,-52,40)

ROI Number	ROI Abbreviation	ROI Name	MNI Coordinates (x,y,z) in mm
98	Dmn.LLP	Default Mode Network (Left Lateral Parietal Cortex)	(-46,-70,36)
99	MedFC	Frontal Medial Cortex	(0,43,-19)
100	SubCalC	Subcallosal Cortex	(-0,21,-15)
101	Dmn.MPFC	Default Mode Network (Medial Prefrontal Cortex)	(-1,49,-5)
102	aPaHC r	Parahippocampal Gyrus (anterior division) Right	(22,-8,-30)
103	aPaHC l	Parahippocampal Gyrus (anterior division) Left	(-22,-9,-30)
104	Hippocampus r	Hippocampus Right	(26,-21,-14)
105	Hippocampus l	Hippocampus Left	(-25,-23,-14)
106	pPaHC r	Parahippocampal Gyrus (posterior division) Right	(23,-31,-17)
107	pPaHC l	Parahippocampal Gyrus (posterior division) Left	(-22,-32,-17)

ROI Number	ROI Abbreviation	ROI Name	MNI Coordinates (x,y,z) in mm
108	Thalamus r	Thalamus Right	(11,-18,7)
109	Thalamus l	Thalamus Left	(-10,-19,6)
110	Pallidum r	Pallidum Right	(20,-4,-1)
111	Pallidum l	Pallidum Left	(-19,-5,-1)
112	Putamen r	Putamen Right	(25,2,0)
113	Putamen l	Putamen Left	(-25,0,0)
114	Caudate r	Caudate Right	(13,10,10)
115	Caudate l	Caudate Left	(-13,9,10)
116	Accumbens r	Accumbens Right	(9,12,-7)
117	Accumbens l	Accumbens Left	(-9,11,-7)
118	Ver12	Vermis 1-2	(1,-39,-20)
119	Cereb10 l	Cerebellum 10 Left	(-23,-34,-42)
120	Cereb10 r	Cerebellum 10 Right	(26,-34,-41)
121	Ver9	Vermis 9	(1,-55,-35)
122	Cereb3 l	Cerebellum 3 Left	(-9,-37,-19)
123	Cereb3 r	Cerebellum 3 Right	(12,-35,-19)
124	Ver3	Vermis 3	(1,-40,-11)
125	Cereb45 r	Cerebellum 4-5 Right	(16,-44,-19)
126	Ver45	Vermis 4-5	(1,-52,-7)
127	Ver6	Vermis 6	(1,-66,-16)
128	Ver7	Vermis 7	(1,-72,-25)
129	Ver8	Vermis 8	(1,-64,-34)

ROI Number	**ROI Abbreviation**	**ROI Name**	**MNI Coordinates (x,y,z) in mm**
130	Cereb1 l	Cerebellum Crus 1 Left	(-36,-66,-30)
131	Cereb7 l	Cerebellum 7b Left	(-32,-60,-45)
132	Cereb7 r	Cerebellum 7b Right	(33,-63,-48)
133	Cereb1 r	Cerebellum Crus 1 Right	(38,-67,-30)
134	Cereb2 r	Cerebellum Crus 2 Right	(32,-69,-40)
135	Cereb2 l	Cerebellum Crus 2 Left	(-29,-73,-38)
136	Ver10	Vermis 10	(0,-46,-32)

Bibliography

Aftanas, L. and Golocheikine, S. (2001). Human anterior and frontal midline theta and lower alpha reflect emotionally positive state and internalized attention: high-resolution EEG investigation of meditation. *Neuroscience Letters*, **310**(1), 57–60.

Akerlund, E., Esbjörnsson, E., Sunnerhagen, K. S., and Björkdahl, A. (2013). Can computerized working memory training improve impaired working memory, cognition and psychological health? *PloS one*, **44**(3), 606–621.

Allen, P. J., Polizzi, G., Krakow, K., Fish, D. R., and Lemieux, L. (1998). Identification of EEG events in the MR scanner: the problem of pulse artifact and a method for its subtraction. *NeuroImage*, **8**(3), 229–239.

Allen, P. J., Josephs, O., and Turner, R. (2000). A method for removing imaging artifact from continuous EEG recorded during functional MRI. *NeuroImage*, **12**(2), 230–9.

Allison, B. Z. and Pineda, J. A. (2003). ERPs evoked by different matrix sizes: Implications for a brain computer interface (BCI) system. *IEEE Transactions on Neural Systems and Rehabilitation Engineering*, **11**(2), 110–113.

Alvarez, J. A. and Emory, E. (2006). Executive function and the frontal lobes: A meta-analytic review. *Neuropsychology Review*, **16**(1), 17–42.

Andén, J. and Mallat, S. (2011). Multiscale scattering for audio classification. *Proceedings of the 12th International Society for Music Information Retrieval Conference (ISMIR 2011), Miami (Florida), 24-28 October 2011*, (2), 657–662.

Andén, J. and Mallat, S. (2012). Scattering representation of modulated sounds. *Proc. of the 15th Int. Conference on Digital Audio ...*, (3), 15–18.

Anderson, G. S. and Harrison, R. R. (2010). Wireless integrated circuit for the acquisition of electrocorticogram signals. In *Proceedings of 2010 IEEE International Symposium on Circuits and Systems*, pages 2952–2955. IEEE.

Astafiev, S. V., Zinn, K. L., Shulman, G. L., and Corbetta, M. (2016). Exploring the physiological correlates of chronic mild traumatic brain injury symptoms. *NeuroImage: Clinical*, **11**, 10–19.

Barrese, J. C., Aceros, J., and Donoghue, J. P. (2016). Scanning electron microscopy of chronically implanted intracortical microelectrode arrays in non-human primates. *Journal of Neural Engineering*, **13**(2), 026003.

Bashashati, A., Fatourechi, M., Ward, R. K., and Birch, G. E. (2007). A Survey of Signal Processing Algorithms in Brain-Computer Interfaces Based on Electrical Brain Signals. *Journal of Neural Engineering*, **4**(2), 32–57.

Beckmann, C. and DeLuca, M. (2005). Investigations into resting-state connectivity using independent component analysis. *of the Royal ....*

Berger, H. (1929). Über das Elektrenkephalogramm des Menschen. *Archiv für Psychiatrie und Nervenkrankheiten*, **87**(1), 527–570.

Bettencourt, K. and Xu, Y. (2016). Decoding the content of visual short-term memory under distraction in occipital and parietal areas. *Nature neuroscience*.

Bhagat, N. A., Venkatakrishnan, A., Abibullaev, B., Artz, E. J., Yozbatiran, N., Blank, A. A., French, J., Karmonik, C., Grossman, R. G., O'Malley, M. K., Francisco, G. E., and Contreras-Vidal, J. L. (2016). Design and optimization of an EEG-based brain machine interface (BMI) to an upper-limb exoskeleton for stroke survivors. *Frontiers in Neuroscience*, **10**(MAR).

Bigler, E. D. and Maxwell, W. L. (2012). Neuropathology of mild traumatic brain injury: Relationship to neuroimaging findings. *Brain Imaging and Behavior*, **6**(2), 108–136.

Binder, L. M., Rohling, M. L., and Larrabee, G. J. (1997). A review of mild head trauma. Part I: Meta-analytic review of neuropsychological studies. *Journal of clinical and experimental neuropsychology*, **19**(3), 421–431.

Biswal, B., FZ, Y., VM, H., and JS, H. (1995). - Functional connectivity in the motor cortex of resting human brain using. *Magn Reson Med*, **34**(9), 537–541.

Blankertz, B., Curio, G., and Muller, K. (2002). Classifying single trial EEG: Towards brain computer interfacing. *Advances in neural information*.

Blankertz, B., Losch, F., Krauledat, M., Dornhege, G., Curio, G., and MÜller, K.-R.

(2008). The Berlin Brain-Computer Interface: Accurate performance from first-session in BCI-naive subjects. *IEEE Transactions on Biomedical Engineering*, **55**(10), 2452–2462.

Blankertz, B., Lemm, S., Treder, M., Haufe, S., and M??ller, K. R. (2011). Single-trial analysis and classification of ERP components - A tutorial. *NeuroImage*, **56**(2), 814–825.

Boersma, M., Smit, D. J. A., De Bie, H. M. A., Van Baal, G. C. M., Boomsma, D. I., De Geus, E. J. C., Delemarre-Van De Waal, H. A., and Stam, C. J. (2011). Network analysis of resting state EEG in the developing young brain: Structure comes with maturation. *Human Brain Mapping*, **32**(3), 413–425.

Bostanov, V. (2004). BCI competition 2003 - Data sets Ib and IIb: Feature extraction from event-related brain potentials with the continuous wavelet transform and the t-value scalogram. *IEEE Transactions on Biomedical Engineering*, **51**(6), 1057–1061.

Bruna, J. and Mallat, S. (2011). Classification with scattering operators. *Proceedings of the IEEE Computer Society Conference on Computer Vision and Pattern Recognition*, (2), 1561–1566.

Bugos, J. a., Perlstein, W. M., McCrae, C. S., Brophy, T. S., and Bedenbaugh, P. H. (2007). Individualized Piano Instruction enhances executive functioning and working memory in older adults. *Aging & Mental Health*, **11**(4), 464–471.

Bullmore, E. and Sporns, O. (2009). Complex brain networks: graph theoretical

analysis of structural and functional systems. *Nature reviews. Neuroscience*, **10**(3), 186–198.

Bundy, D. T., Pahwa, M., Szrama, N., and Leuthardt, E. C. (2016). Decoding three-dimensional reaching movements using electrocorticographic signals in humans. *Journal of neural engineering*, **13**(2), 026021.

Buzsáki, G., Anastassiou, C. a., and Koch, C. (2012). The origin of extracellular fields and currents–EEG, ECoG, LFP and spikes. *Nature reviews. Neuroscience*, **13**(6), 407–20.

Byard, R. W. and Vink, R. (2009). The second impact syndrome. *Forensic Science, Medicine, and Pathology*, **5**(1), 36–38.

Castellanos, F. X., Margulies, D. S., Kelly, C., Uddin, L. Q., Ghaffari, M., Kirsch, A., Shaw, D., Shehzad, Z., Di Martino, A., Biswal, B., Sonuga-Barke, E. J. S., Rotrosen, J., Adler, L. A., and Milham, M. P. (2008). Cingulate-Precuneus Interactions: A New Locus of Dysfunction in Adult Attention-Deficit/Hyperactivity Disorder. *Biological Psychiatry*, **63**(3), 332–337.

Chudacek, V., Talmon, R., Anden, J., Mallat, S., Coifman, R. R., Abry, P., and Doret, M. (2014). Low dimensional manifold embedding for scattering coefficients of intrapartum fetale heart rate variability. *Conference proceedings : ... Annual International Conference of the IEEE Engineering in Medicine and Biology Society. IEEE Engineering in Medicine and Biology Society. Annual Conference*, **2014**, 6373–6376.

Clark, V., Fannon, S., Lai, S., and Benson, R. (2000). Responses to rare visual target and distractor stimuli using event-related fMRI. *Journal of*.

Cohen, D. (1972). Magnetoencephalography : Detection of the Brain's Electrical Activity with a Superconducting Magnetometer. *Science*, **175**(4022), 664–666.

Cole, D. M., Smith, S. M., and Beckmann, C. F. (2010). Advances and pitfalls in the analysis and interpretation of resting-state FMRI data. *Frontiers in systems neuroscience*, **4**(April), 8.

Corradini, P. L. and Persinger, M. a. (2014). Spectral power, source localization and microstates to quantify chronic deficits from 'mild' closed head injury: Correlation with classic neuropsychological tests. *Brain Injury*, **28**(10), 1317–1327.

Cover, T. (1965). Geometrical and statistical properties of systems of linear inequalities with applications in pattern recognition. *IEEE transactions on electronic computers*.

Cox, R. W. (1996). AFNI: Software for Analysis and Visualization of Functional Magnetic Resonance Neuroimages. *Computers and Biomedical Research*, **29**(3), 162–173.

Coyle, S. M., Ward, T. E., Markham, C. M., Ward, E., and Markham, C. M. (2007). Brain-computer interface using a simplified functional near-infrared spectroscopy system. *Journal of neural engineering*, **4**(3), 219–26.

Daly, J. J. and Wolpaw, J. R. (2008). Brain-computer interfaces in neurological rehabilitation. *The Lancet Neurology*, **7**(11), 1032–1043.

Das, K., Osechinskiy, S., and Nenadic, Z. (2007). A classwise PCA-based recognition of neural data for brain-computer interfaces. *Annual International Conference of the IEEE Engineering in Medicine and Biology - Proceedings*, pages 6519–6522.

de Munck, J. C., van Houdt, P. J., Gon??alves, S. I., van Wegen, E., and Ossenblok, P. P. W. (2013). Novel artefact removal algorithms for co-registered EEG/fMRI based on selective averaging and subtraction. *NeuroImage*, **64**(1), 407–415.

Degenhart, A. D., Mischel, J., Endler, B., Smalianchuk, I., Ashmore, R. C., Cui, T., Dum, R., Elizabeth, C., Wang, W., and Batista, A. P. (2015). Evaluation of a chronically-implanted electrocorticographic electrode grid in a nonhuman primate. *To be submitted*, **13**(4), 1–24.

Delorme, A. and Makeig, S. (2004). EEGLAB: An open source toolbox for analysis of single-trial EEG dynamics including independent component analysis. *Journal of Neuroscience Methods*, **134**(1), 9–21.

Engle, R. W., Tugade, M. M., and Barrett, L. F. (2004). Individual Differences in Working Memory Capacity and Dual-Process Theories of the Mind. *Psychological Bulletin*, **130**(4), 553–573.

Estrach, J. B. (2012). Scattering Representations for Recognition. (November).

Fatourechi, M., Bashashati, A., Ward, R. K., and Birch, G. E. (2007). EMG and EOG artifacts in brain computer interface systems: A survey. *Clinical Neurophysiology*, **118**(3), 480–494.

Fayyad, U., Piatetsky-Shapiro, G., and Smyth, P. (1996). From Data Mining to Knowledge Discovery in Databases. *AI Magazine*, **17**(3), 37–54.

Friedberg, R. M. (1958). A Learning Machine: Part I. *IBM Journal of Research and Development*, **2**(1), 2–13.

Friederici, A. D., Rüschemeyer, S.-A., Hahne, A., and Fiebach, C. J. (2003). The role of left inferior frontal and superior temporal cortex in sentence comprehension: localizing syntactic and semantic processes. *Cerebral cortex (New York, N.Y. : 1991)*, **13**(2), 170–177.

Gaetz, M. and Bernstein, D. M. (2001). The current status of electrophysiologic procedures for the assessment of mild traumatic brain injury. *The Journal of head trauma rehabilitation*, **16**(4), 386–405.

Gao, X., Xu, D., Cheng, M., and Gao, S. (2003). A BCI-based environmental controller for the motion-disabled. *IEEE Transactions on Neural Systems and Rehabilitation Engineering*, **11**(2), 137–140.

Gitelman, D. R., Nobre, a. C., Parrish, T. B., LaBar, K. S., Kim, Y. H., Meyer, J. R., and Mesulam, M. M. (1999). A large-scale distributed network for covert spatial attention. *Brain*, **122**(6), 1093–1106.

Glaser, J., Beisteiner, R., Bauer, H., and Fischmeister, F. P. S. (2013). FACET - a "Flexible Artifact Correction and Evaluation Toolbox" for concurrently recorded EEG/fMRI data. *BMC neuroscience*, **14**(1), 138.

Gloor, P. (1969). Hans Berger on Electroencephalography. *American Journal of EEG Technology*.

Goksu, F., Ince, N., and Tewfik, A. (2011). Sparse common spatial patterns in brain computer interface applications. *2011 IEEE International*.

Gonçalves, S., Pouwels, P., and Kuijer, J. (2007). Artifact removal in co-registered EEG/fMRI by selective average subtraction. *Clinical*.

Greenberg, L. and Waldmant, I. (1993). Developmental normative data on The test of variables of attention (TOVA). *Journal of Child Psychology and*.

Greicius, M. D., Flores, B. H., Menon, V., Glover, G. H., Solvason, H. B., Kenna, H., Reiss, A. L., and Schatzberg, A. F. (2007). Resting-State Functional Connectivity in Major Depression: Abnormally Increased Contributions from Subgenual Cingulate Cortex and Thalamus. *Biological Psychiatry*, **62**(5), 429–437.

Grosse-Wentrup, M. and Buss, M. (2008). Multiclass common spatial patterns and information theoretic feature extraction. *IEEE transactions on Biomedical*.

Guger, C., Guger, C., Ramoser, H., and Pfurtscheller, G. (2001). Real-Time EEG Analysis with Subject-Specific Real-Time EEG Analysis with Subject-Specific Spatial Patterns for a Brain Computer Interface (BCI). **8**(October 2015), 447–456.

Gundogdu, O., Egrioglu, E., Aladag, C. H., and Yolcu, U. (2015). Multiplicative neuron model artificial neural network based on Gaussian activation function. *Neural Computing and Applications*, pages 927–935.

Halder, S., Agorastos, D., Veit, R., Hammer, E. M., Lee, S., Varkuti, B., Bogdan, M., Rosenstiel, W., Birbaumer, N., and Kübler, A. (2011). Neural mechanisms of brain-computer interface control. *NeuroImage*, **55**(4), 1779–1790.

Halder, S., Käthner, I., and Kübler, A. (2016). Training leads to increased auditory brain-computer interface performance of end-users with motor impairments. *Clinical Neurophysiology*, **127**(2), 1288–1296.

Hamadicharef, B. (2010). Brain-Computer Interface (BCI) literature-a bibliometric study. *... and their Applications (ISSPA), 2010 10th ...*, **1**(Isspa), 626–629.

Hamedi, M., Salleh, H., and Noor, A. M. (2016). Electroencephalic Motor Imagery Brain Connectivity Analysis for BCI: A Review. *Neural computation*, **1872**(28), 999–1041.

Hammer, E. M., Halder, S., Blankertz, B., Sannelli, C., Dickhaus, T., Kleih, S., Müller, K. R., and Kübler, A. (2012). Psychological predictors of SMR-BCI performance. *Biological Psychology*, **89**(1), 80–86.

Hammer, E. M., Kaufmann, T., Kleih, S. C., Blankertz, B., and KÃbler, A. (2014). Visuo-motor coordination ability predicts performance with brain-computer interfaces controlled by modulation of sensorimotor rhythms (SMR). *Frontiers in Human Neuroscience*, **8**(August), Article 574.

Huettel, S., Song, A., and McCarthy, G. (2004). *Functional magnetic resonance imaging*.

Hutchison, R. M., Womelsdorf, T., Allen, E. A., Bandettini, P. A., Calhoun, V. D., Corbetta, M., Della Penna, S., Duyn, J. H., Glover, G. H., Gonzalez-Castillo, J., Handwerker, D. A., Keilholz, S., Kiviniemi, V., Leopold, D. A., de Pasquale, F., Sporns, O., Walter, M., and Chang, C. (2013). Dynamic functional connectivity: Promise, issues, and interpretations. *NeuroImage*, **80**, 360–378.

Iriarte, J., Urrestarazu, E., Valencia, M., Alegre, M., Malanda, A., Viteri, C. C., and Artieda, J. (2003). Independent component analysis as a tool to eliminate

artifacts in EEG: a quantitative study. *Journal of clinical neurophysiology : official publication of the American Electroencephalographic Society*, **20**(4), 249–257.

Jain, A. and Swaminathan, S. (2014). Incorporating Scattering Transform in Similarity Metric Learning with Application to Face Verification. pages 1–8.

Kachenoura, A., Albera, L., Senhadji, L., and Comon, P. (2008). ICA: A potential tool for BCI systems. *IEEE Signal Processing Magazine*, **25**(1), 57–68.

Kaper, M., Meinicke, P., Grossekathoefer, U., Lingner, T., and Ritter, H. (2004). BCI competition 2003 - Data set IIb: Support vector machines for the P300 speller paradigm. *IEEE Transactions on Biomedical Engineering*, **51**(6), 1073–1076.

Keightley, M. L., Saluja, R. S., Chen, J.-K., Gagnon, I., Leonard, G., Petrides, M., and Ptito, A. (2014). A functional magnetic resonance imaging study of working memory in youth after sports-related concussion: is it still working? *Journal of neurotrauma*, **31**(5), 437–51.

Kerr, W. T., Anderson, A., Xia, H., Braun, E. S., Lau, E. P., Cho, A. Y., and Cohen, M. S. (2012). Parameter Selection in Mutual Information-Based Feature Selection in Automated Diagnosis of Multiple Epilepsies Using Scalp EEG. In *2012 Second International Workshop on Pattern Recognition in NeuroImaging*, pages 45–48. IEEE.

Khanna, A., Pascual-Leone, A., and Farzan, F. (2014). Reliability of resting-state microstate features in electroencephalography. *PLoS ONE*, **9**(12), 1–21.

Khodayari-Rostamabad, A., Hasey, G. M., MacCrimmon, D. J., Reilly, J. P., and

Bruin, H. d. (2010). A pilot study to determine whether machine learning methodologies using pre-treatment electroencephalography can predict the symptomatic response to clozapine therapy. *Clinical Neurophysiology*, **121**(12), 1998–2006.

Kirkove, M., Francois, C., and Verly, J. (2014). Comparative evaluation of existing and new methods for correcting ocular artifacts in electroencephalographic recordings. *Signal Processing*, **98**, 102–120.

Kober, S., Witte, M., and Ninaus, M. (2013). Learning to modulate one's own brain activity: the effect of spontaneous mental strategies. *Frontiers in human ...*, **7**(October), 695.

Kruggel, F., Wiggins, C. J., Herrmann, C. S., and Von Cramon, D. Y. (2000). Recording of the event-related potentials during functional MRI at 3. 0 tesla field strength. *Magnetic Resonance in Medicine*, **44**(2), 277–282.

LaConte, S., Anderson, J., Muley, S., Ashe, J., Frutiger, S., Rehm, K., Hansen, L. K., Yacoub, E., Hu, X., Rottenberg, D., and Strother, S. (2003). The Evaluation of Preprocessing Choices in Single-Subject BOLD fMRI Using NPAIRS Performance Metrics. *NeuroImage*, **18**(1), 10–27.

Lacroix, J. M. and Gowen, A. H. (1981). The Acquisition of Autonomic Control Through Biofeedback: Some Tests of Discrimination Theory. *Psychophysiology*, **18**(5), 559–572.

Lal, T. N., Schr, M., Hill, N. J., Preissl, H., Bogdan, M., Rosenstiel, W., Hofmann, T., Birbaumer, N., and Sch, B. (2005). A Brain Computer Interface with Online

Feedback based on Magnetoencephalography. *22Nd International Conference on Machine Learning*, pages 465–472.

Lance, B. B. J., Ieee, M., Kerick, S. E., Ries, A. J., Oie, K. S., Mcdowell, K., and Ieee, S. M. (2012). Brain Computer Interface Technologies in the Coming Decades.

Lang, P. J. and Twentyman, C. T. (1976). Learning to Control Heart Rate: Effects of Varying Incentive and Criterion of Success on Task Performance. *Psychophysiology*, **13**(5), 378–385.

Larkum, M. E., Zhu, J. J., and Sakmann, B. (2001). Dendritic mechanisms underlying the coupling of the dendritic with the axonal action potential initiation zone of adult rat layer 5 pyramidal neurons. *The Journal of Physiology*, **533**(2), 447–466.

Lehembre, R., Bruno, M. A., Vanhaudenhuyse, A., Chatelle, C., Cologan, V., Leclercq, Y., Soddu, A., Macq, B., Laureys, S., and Noirhomme, Q. (2012). Resting-state EEG study of comatose patients: A connectivity and frequency analysis to find differences between vegetative and minimally conscious states. *Functional Neurology*, **27**(1), 41–47.

Lehmann, D. (1990). Brain Electric Microstates and Cognition: The Atoms of Thought. In *Machinery of the Mind*, pages 209–224. Birkhäuser Boston, Boston, MA.

Lehmann, D., Faber, P., Achermann, P., Jeanmonod, D., Gianotti, L. R., and Pizzagalli, D. (2001). Brain sources of EEG gamma frequency during volitionally meditation-induced, altered states of consciousness, and experience of the self. *Psychiatry Research: Neuroimaging*, **108**(2), 111–121.

Lerch, M. (2015). Accent Classification using Scattering Coefficients. *OpenStax-CNX*.

Leuthardt, E. C., Freudenberg, Z., Bundy, D., and Roland, J. (2009). Microscale recording from human motor cortex: implications for minimally invasive electrocorticographic brain-computer interfaces. *Neurosurgical focus*, **27**(1), E10.

Linden, D., Prvulovic, D., and Formisano, E. (1999). The functional neuroanatomy of target detection: an fMRI study of visual and auditory oddball tasks. *Cerebral*.

Lotte, F., Congedo, M., Lecuyer, A., Lamarche, F., and Arnaldi, B. (2007). A review of classification algorithms for EEG-based brain-computer interfaces. *J Neural Eng*, **4**(2), R1–R13.

Macfarlane, M. P. and Glenn, T. C. (2015). Neurochemical cascade of concussion. *Brain Injury*, **9052**(2), 139–153.

Mallat, S. (2012). Group Invariant Scattering. *Communications on Pure and Applied Mathematics*, **65**(10), 1331–1398.

Mayer, A. R. and Bellgowan, P. S. F. (2014). *Concussions in Athletics*.

McAllister, T. W., Flashman, L. a., McDonald, B. C., and Saykin, A. J. (2006). Mechanisms of working memory dysfunction after mild and moderate TBI: evidence from functional MRI and neurogenetics. *Journal of neurotrauma*, **23**(10), 1450–1467.

McCane, L. M., Sellers, E. W., McFarland, D. J., Mak, J. N., Carmack, C. S., Zeitlin, D., Wolpaw, J. R., and Vaughan, T. M. (2014). Brain-computer interface (BCI) evaluation in people with amyotrophic lateral sclerosis. *Amyotrophic lateral sclerosis & frontotemporal degeneration*, (November 2013), 1–9.

McFarland, D. J. and Wolpaw, J. R. (2011). Brain-computer interfaces for communication and control. *Communications of the ACM*, **54**(5), 60–66.

Medathati, N., Neumann, H., Masson, G. S., and Kornprobst, P. (2016). Bio-Inspired Computer Vision: Towards a Synergistic Approach of Artificial and Biological Vision. *Computer Vision and Image Understanding*, **0**, 1–30.

Meehan, T. P. and Bressler, S. L. (2012). Neurocognitive networks: Findings, models, and theory. *Neuroscience and Biobehavioral Reviews*, **36**(10), 2232–2247.

Meir-Hasson, Y., Kinreich, S., Podlipsky, I., Hendler, T., and Intrator, N. (2014). An EEG Finger-Print of fMRI deep regional activation. *NeuroImage*, **102**, 128–141.

Michel, C., Lehmann, D., and Henggeler, B. (1992). Localization of the sources of EEG delta, theta, alpha and beta frequency bands using the FFT dipole approximation. *Electroencephalography*.

Milz, P., Faber, P., Lehmann, D., Koenig, T., Kochi, K., and Pascual-Marqui, R. (2015). The functional significance of EEG microstatesAssociations with modalities of thinking. *NeuroImage*, **125**, 643–656.

Milz, P., Faber, P. L., Lehmann, D., Koenig, T., Kochi, K., and Pascual-Marqui, R. D. (2016). The functional significance of EEG microstates-Associations with modalities of thinking. *NeuroImage*, **125**, 643–656.

Miyake, A., Friedman, N. P., Emerson, M. J., Witzki, a. H., Howerter, A., and Wager, T. D. (2000). The unity and diversity of executive functions and their contributions to complex "Frontal Lobe" tasks: a latent variable analysis. *Cognitive psychology*, **41**(1), 49–100.

Morrison, A. B. and Chein, J. M. (2011). Does working memory training work? The promise and challenges of enhancing cognition by training working memory. *Psychonomic bulletin & review*, **18**(1), 46–60.

Mostofsky, S., Schafer, J., and Abrams, M. (2003). fMRI evidence that the neural basis of response inhibition is task-dependent. *Cognitive brain*.

Müller, K. R., Tangermann, M., Dornhege, G., Krauledat, M., Curio, G., and Blankertz, B. (2008). Machine learning for real-time single-trial EEG-analysis: From brain-computer interfacing to mental state monitoring. *Journal of Neuroscience Methods*, **167**(1), 82–90.

Murphy, K., Birn, R. M., and Bandettini, P. A. (2013). Resting-state fMRI confounds and cleanup. *NeuroImage*, **80**, 349–359.

Musso, F., Brinkmeyer, J., Mobascher, A., Warbrick, T., and Winterer, G. (2010). Spontaneous brain activity and EEG microstates. A novel EEG/fMRI analysis approach to explore resting-state networks. *NeuroImage*, **52**(4), 1149–1161.

Naeem Mannan, M. M., Jeong, M. Y., and Kamran, M. A. (2016). Hybrid ICA regression: automatic identification and removal of ocular artifacts from electroencephalographic signals. *Frontiers in Human Neuroscience*, **10**(193), 1–17.

Neumann, N., Kuebler, A., Kaiser, J., Hinterberger, T., and Birbaumer, N. (2003). Conscious perception of brain states: mental strategies for brain-computer communication Bewusste Wahrnehmung von Hirnzustaenden: Mentale Strategien fuer die Gehirn-Computer-Kommunikation. *Neuropsychologia*, **41**, 1028–1036.

Niazy, R., Beckmann, C., Iannetti, G., Brady, J., and Smith, S. (2005). Removal of FMRI environment artifacts from EEG data using optimal basis sets. *NeuroImage*, **28**(3), 720–737.

Nicolas-Alonso, L. F. and Gomez-Gil, J. (2012). Brain computer interfaces, a review. *Sensors*, **12**(2), 1211–1279.

Nijboer, F., Birbaumer, N., and Kübler, A. (2010). The influence of psychological state and motivation on brain-computer interface performance in patients with amyotrophic lateral sclerosis - a longitudinal study. *Frontiers in Neuroscience*, **4**(JUL), 1–13.

Odom, J., Bach, M., Barber, C., Brigell, M., Marmor, M., a P, T., G E, H., and Vaegan (2004). Visual evoked potentials standard. *Documenta Ophthalmologica*, **108(2)**, 115–123.

Oken, B. S., Orhan, U., Roark, B., Erdogmus, D., Fowler, A., Mooney, A., Peters, B., Miller, M., and Fried-Oken, M. B. (2013). Brain–Computer Interface With Language Model–Electroencephalography Fusion for Locked-In Syndrome. *Neurorehabilitation and neural repair*, page 1545968313516867.

Oostenveld, R., Fries, P., Maris, E., and Schoffelen, J. M. (2011). FieldTrip: Open source software for advanced analysis of MEG, EEG, and invasive electrophysiological data. *Computational Intelligence and Neuroscience*, **2011**.

Peng, A. W., Effertz, T., and Ricci, A. J. (2013). Adaptation of Mammalian Auditory Hair Cell Mechanotransduction Is Independent of Calcium Entry. *Neuron*, **80**(4), 960–972.

Pfurtscheller, G. and Aranibar, A. (1977). Event-related cortical desynchronization detected by power measurements of scalp EEG. *Electroencephalography and Clinical Neurophysiology*, **42**(6), 817–826.

Pfurtscheller, G. and Guger, C. (1999). Braincomputer communication system: EEG-based control of hand orthesis in a tetraplegic patient. *Acta Chir. Austriaca*, **31**(Suppl 159), 23–25.

Pfurtscheller, G. and Lopes, F. H. (1999). Event-related EEG / MEG synchronization and desynchronization : basic principles. *Clinical Neurophysiology*, **110**, 1842–1857.

Riccio, A., Simione, L., Schettini, F., Pizzimenti, A., Inghilleri, M., Belardinelli, M. O., Mattia, D., and Cincotti, F. (2013). Attention and P300-based BCI performance in people with amyotrophic lateral sclerosis. *Frontiers in Human Neuroscience*, **7**(November), 732.

Rice, J. K., Rorden, C., Little, J. S., and Parra, L. C. (2013). Subject position affects EEG magnitudes. *NeuroImage*, **64**(1), 476–484.

Ritter, P., Becker, R., Graefe, C., and Villringer, A. (2007). Evaluating gradient artifact correction of EEG data acquired simultaneously with fMRI. *Magnetic Resonance Imaging*, **25**(6), 923–932.

Rosenblatt, F. (1958). The perceptron: A probabilistic model for information storage and organization in the brain. *Psychological Review*, **65**(6), 386–408.

Rothenberg, M. (1982). The Endless Space Frontier: A History of the House Committee on Science and Astronautics, 1959-1978 Ken Hechler. *The Public Historian*, **4**(4), 127–129.

Salek-Haddadi, A., Friston, K. J., Lemieux, L., and Fish, D. R. (2003). Studying spontaneous EEG activity with fMRI. *Brain Research Reviews*, **43**(1), 110–133.

Salvaris, M. and Sepulveda, F. (2009). Visual modifications on the P300 speller BCI paradigm. *Journal of neural engineering*, **6**(4), 046011.

Samek, W., Vidaurre, C., Müller, K.-R., and Kawanabe, M. (2012). Stationary Common Spatial Patterns for Brain-Computer Interfacing. **9**.

Schwartz, a. B. (1993). Motor cortical activity during drawing movements: population representation during sinusoid tracing. *Journal of neurophysiology*, **70**(1), 28–36.

Seghier, M. (2012). The Angular Gyrus: Multiple Functions and Multiple Subdivisions. *The Neuroscientist*, **19**(1), 43–61.

Sehatpour, P., Dias, E. C., Butler, P. D., Revheim, N., Guilfoyle, D. N., Foxe, J. J., and Javitt, D. C. (2010). Impaired visual object processing across an occipital-frontal-hippocampal brain network in schizophrenia: an integrated neuroimaging study. *Archives of general psychiatry*, **67**(8), 772–82.

Shih, J. J., Krusienski, D. J., and Wolpaw, J. R. (2012). Brain-computer interfaces in medicine. *Mayo Clinic Proceedings*, **87**(3), 268–279.

Sifre, L., Kapoko, M., Oyallon, E., and Lostanlen, V. (2013). ScatNet : a MATLAB Toolbox for Scattering Networks. pages 1–26.

Skinner, B. F. (1945). The operational analysis of psychological terms. *Psychological Review*, **52**(5), 270–277.

So, E. L. (2000). Integration of EEG, MRI, and SPECT in Localizing the Seizure Focus for Epilepsy Surgery. *Epilepsia*, **41**(s3), S48–S54.

Sprague, S. A., McBee, M. T., and Sellers, E. W. (2015). The effects of working memory on braincomputer interface performance. *Clinical Neurophysiology*, **127**(2), 1331–1341.

Srivastava, G., Crottaz-Herbette, S., Lau, K. M., Glover, G. H., and Menon, V. (2005). ICA-based procedures for removing ballistocardiogram artifacts from EEG data acquired in the MRI scanner. *NeuroImage*, **24**(1), 50–60.

Talairach, J. and Tournoux, P. (1988). Co-planar stereotaxic atlas of the human brain. 3-Dimensional proportional system: an approach to cerebral imaging.

Tsytsarev, V., Liao, L.-D., Kong, K. V., Liu, Y.-H., Erzurumlu, R. S., Olivo, M., and Thakor, N. V. (2014). Recent progress in voltage-sensitive dye imaging for neuroscience. *Journal of nanoscience and nanotechnology*, **14**(7), 4733–44.

Tzvi, E., Verleger, R., Münte, T., and Krämer, U. (2016). Reduced alpha-gamma phase amplitude coupling over right parietal cortex is associated with implicit visuomotor sequence learning. *NeuroImage*.

Uddin, L. Q., Kelly, A. M. C., Biswal, B. B., Castellanos, F. X., and Milham, M. P. (2009). Functional Connectivity of Default Mode Network Components: Correlation, Anticorrelation, and Causality. *Human Brain Mapping*, **30**(2), 625–637.

Uludag, K., Dubowitz, D. J., and Buxton, R. B. (2005). Basic Principles of Functional Mri. *Clinical MRI*, pages 249–287.

Vainer, I., Kraus, S., Kaminka, G. A., and Slovin, H. (2009). Scalable classification in large scale spatiotemporal domains applied to voltage-sensitive dye imaging. *Proceedings - IEEE International Conference on Data Mining, ICDM*, pages 543–551.

Van de Ville, D., Britz, J., and Michel, C. M. (2010). EEG microstate sequences in healthy humans at rest reveal scale-free dynamics. *Proceedings of the National Academy of Sciences of the United States of America*, **107**(42), 18179–18184.

van der Meer, J. N., Pampel, A., Van Someren, E. J. W., Ramautar, J. R., van der Werf, Y. D., Gomez-Herrero, G., Lepsien, J., Hellrung, L., Hinrichs, H., Möller, H. E., and Walter, M. (2015). Carbon-wire loop based artefact correction outperforms post-processing EEG/fMRI corrections-A validation of a real-time simultaneous EEG/fMRI correction method. *NeuroImage*, **125**, 880–894.

Van Veen, V. and Carter, C. S. (2002). The anterior cingulate as a conflict monitor: FMRI and ERP studies. *Physiology and Behavior*, **77**(4-5), 477–482.

Vargas-Irwin, C. E., Shakhnarovich, G., Yadollahpour, P., Mislow, J. M. K., Black, M. J., and Donoghue, J. P. (2010). Decoding Complete Reach and Grasp Actions from Local Primary Motor Cortex Populations. *J Neurosci*, **30**(29), 9659–9669.

Velliste, M., Perel, S., Spalding, M. C., Whitford, a. S., and Schwartz, a. B. (2008). Cortical control of a robotic arm for self-feeding. *Nature*, **453**(June), 1098–1101.

Vidal, J. J. (1973). Tow ard direct brain-computer 9027 communication. *Annual review of biophysics and bioengineering*, **2**, 157–80.

Wan, X., Iwata, K., Riera, J., Ozaki, T., Kitamura, M., and Kawashima, R. (2006). Artifact reduction for EEG/fMRI recording: Nonlinear reduction of ballistocardiogram artifacts. *Clinical Neurophysiology*, **117**(3), 668–680.

Wang, Y., Wang, R., Gao, X., Hong, B., and Gao, S. (2006). A practical VEP-based brain-computer interface. *IEEE Transactions on Neural Systems and Rehabilitation Engineering*, **14**(2), 234–239.

Weidong Zhou and Gotman, J. (2015). Removal of EMG and ECG artifacts from EEG based on wavelet transform and ICA. In *The 26th Annual International Conference of the IEEE Engineering in Medicine and Biology Society*, volume 3, pages 392–395. IEEE.

Weiskopf, N., Mathiak, K., Bock, S. W., Scharnowski, F., Veit, R., Grodd, W., Goebel, R., and Birbaumer, N. (2004). Principles of a brain-computer interface (BCI) based on real-time functional magnetic resonance imaging (fMRI). *IEEE Transactions on Biomedical Engineering*, **51**(6), 966–970.

Whitfield-Gabrieli, S. and Nieto-Castanon, A. (2012). Conn: a functional connectivity toolbox for correlated and anticorrelated brain networks. *Brain connectivity*, **2**(3), 125–41.

Whittingstall, K. and Logothetis, N. K. (2009). Frequency-Band Coupling in Surface EEG Reflects Spiking Activity in Monkey Visual Cortex. *Neuron*, **64**(2), 281–289.

Wolpaw, J., McFarland, D., and Neat, G. (1991). An EEG-based brain-computer interface for cursor control. *Electroencephalography*.

Yaesoubi, M., Allen, E. A., Miller, R. L., and Calhoun, V. D. (2015). Dynamic coherence analysis of resting fMRI data to jointly capture state-based phase, frequency, and time-domain information. *NeuroImage*, **120**, 133–142.

Yu, X., Chum, P., and Sim, K. B. (2014). Analysis the effect of PCA for feature reduction in non-stationary EEG based motor imagery of BCI system. *Optik*, **125**(3), 1498–1502.

Yuan, H., Zotev, V., Phillips, R., Drevets, W. C., and Bodurka, J. (2012). Spatiotemporal dynamics of the brain at rest - Exploring EEG microstates as electrophysiological signatures of BOLD resting state networks. *NeuroImage*, **60**(4), 2062–2072.

Zhang, B., Li, M., Qin, W., Demenescu, L. R., Metzger, C. D., Bogerts, B., Yu, C., and Walter, M. (2016). Altered functional connectivity density in major depressive disorder at rest. *European Archives of Psychiatry and Clinical Neuroscience*, **266**(3), 239–248.

Zotev, V., Phillips, R., Yuan, H., Misaki, M., and Bodurka, J. (2014). Self-regulation of human brain activity using simultaneous real-time fMRI and EEG neurofeedback. *NeuroImage*, **85 Pt 3**, 985–95.